Toward Confined Spaces in Polymers and Microemulsions for Catalytic Applications

von der Fakultät Chemie der Universität Stuttgart zur Erlangung der Würde eines Doktors der Naturwissenschaften (Dr. rer. nat.) genehmigte Abhandlung

vorgelegt von

Yaseen Nazmi Qawasmi

aus Hebron, Palästina

Hauptberichter: Apl. Prof. Dr. Thomas Sottmann

Mitberichterin: Prof. Dr. Bettina V. Lotsch

Prüfungsvorsitzende: Prof. Cosima Stubenrauch

Tag der mündlichen Prüfung:

19.12.2019

Institut für Physikalische Chemie der Universität Stuttgart

2019

Erklärung über die Eigenständigkeit der Dissertation

Ich versichere, dass ich die vorliegende Arbeit selbständig verfasst und keine anderen als die angegebenen Quellen und Hilfsmittel benutzt habe; aus fremden Quellen entnommene Passagen und Gedanken sind als solche kenntlich gemacht.

Declaration of Authorship

I hereby certify that this dissertation is entirely my own work except where otherwise indicated. Passages and ideas from other sources have been clearly indicated.

Stuttgart, den 13.11.2019 Yaseen Nazmi Qawasmi

Abstract

In biocatalysis impressive regio- and stereoselectivities are achieved via the directing influence of the three-dimensional structure of enzymes. As enzymes often suffer from limited pH stability, intolerance of organic solvents and perform only within a limited temperature range, the development of mesoporous support materials in which organometallic catalyst are introduced is targeted in the CRC 1333 "Molecular Heterogeneous Catalysis in Confined Geometries". Thus, the first part of this study dealt with the synthesis of porous polystyrene (PS) and mesoporous PS/ZnO hybrid materials. Following the Nanofoams by Continuity-Inversion of Dispersion (NF-CID) method, in which colloidal crystals of polymer nanoparticles are foamed with supercritical CO_2, porous PS polymers were synthesized in a first step. The results of this thesis show, that pore size, homogeneity, porosity, and morphology of the synthesized porous polymers can be adjusted by the size, polydispersity, and glass transition temperature of the PS nanoparticles as well as the foaming parameters. Open-cellular porous PS with pore size of the order of 50 nm was obtained by modifying the expansion step of the NF-CID method. To enhance the stability of the porous PS and finetune the pore size, the chemical bath deposition method was used to synthesize a mesoporous PS/ZnO hybrid material. Thereby, SEM images and EDX analysis confirm the formation of a thin layer of ZnO particles on the pore walls, while the general porous structure is retained. After the functionalization and anchoring of organometallic catalysts, these mesoporous PS/ZnO hybrid materials will be ready for the use in heterogeneous catalysis.

In the second part of this study, the influence of liquid confinement on asymmetric Rh-catalysis was explored. As a benchmark reaction, the 1,2-addition of boroxine **2** to *N*-tosylimine **1** in the presence of a [Rh/chiral diene ligands] complex was chosen. To create liquid-confinement, a reaction-specific microemulsion containing equal amounts of H_2O/KOH and toluene/reactants was formulated using *n*-octyl β-D-glucopyranoside (C_8G_1). A special feature of this nanostructured reaction medium is the presence of water- and toluene-rich compartments with a domain size of 5.5 nm. Performing the catalysis, a strong dependence on ligand type and reaction media was found. Especially for slightly polar diene ligands the liquid confinement provided by the microemulsion improved reaction rate, yield and enantioselectivity.

Kurzzusammenfassung

In der Biokatalyse werden beeindruckende Regio- und Stereoselektivitäten durch den dirigiererden Einfluss der dreidimensionalen Struktur von Enzymen erreicht. Da Enzyme allerdings häufig eine eingeschränkte pH-Stabilität und Unverträglichkeit gegenüber organischen Lösungsmitteln aufweisen und nur in einem eingeschränkten Temperaturbereich funktionieren, wird die Entwicklung mesoporöser Trägermaterialien, in die metallorganische Katalysatoren eingeführt werden, im der SFB 1333 „Molekulare heterogene Katalyse in definierten, dirigierenden Geometrien" untersucht. Der erste Teil dieser Studie befasste sich daher mit der Synthese von porösem Polystyrol (PS) und mesoporösen PS/ZnO Hybridmaterialien. Im ersten Schritt wurden poröse PS Polymere gemäß des Nanoschaümverfahrens „Nanofoams by Continuity Inversion of Dispersions" (NF-CID) synthetisiert, bei dem kolloidale Kristalle von Polymernanopartikeln mit überkritischen CO_2 aufgeschäumt werden. Die Ergebnisse dieser Arbeit zeigen, dass die Porengröße, Homogenität, Porosität und Morphologie der synthetisierten porösen Polymere durch die Größe, Polydispersität und Glasübergangstemperatur der PS-Nanopartikel sowie die Schäumparameter eingestellt werden können. Durch Modifizieren des Expansionsschritts des NF-CID-Verfahrens konnte offenzelliges poröses Polystyrol mit einer Porengröße in der Größenordnung von 50 nm erhalten werden. Zur Verbesserung der Stabilität des porösen PS und zur weiteren Reduzierung der Porengröße wurde das chemische Badabscheidungsverfahren (CBD) verwendet, um ein mesoporöses PS/ZnO-Hybridmaterial zu synthetisieren. REM-Bilder und EDX-Analysen bestätigen dabei die Bildung einer dünnen Schicht von ZnO-Partikeln auf den Porenwänden, während die allgemeine poröse Struktur erhalten bleibt. Durch anschließende der Funktionalisierung und Verankerung von metallorganischen Katalysatoren sind diese mesoporösen PS/ZnO-Hybridmaterialien bereit um in der heterogenen Katalyse eingesetzt zu werden.

Im zweiten Teil dieser Arbeit wurde der Einfluss flüssiger Nanostrukturen auf die asymmetrische Rh-Katalyse untersucht. Als Benchmark-Reaktion wurde die 1,2-Addition von Boroxin **2** an *N*-Tosylimin **1** in Gegenwart eines [Rh/chiralen Dien-Liganden]-Komplexes gewählt. Zur Herstellung von flüssigen Nanostrukturen wurde eine reaktionsspezifische Mikroemulsion mit gleichen Mengen an H_2O/KOH und Toluol/Reaktanten unter Verwendung von *n*-Octyl-β-D-glucopyranosid (C_8G_1) formuliert. Eine Besonderheit dieses nanostrukturierten Reaktionsmediums ist das Vorhandensein

wasser- und toluolreicher Domänen mit einer Domänengröße von 5,5 nm. Bei der Durchführung der Katalyse wurde eine starke Abhängigkeit des Ligandentyps und Reaktionsmedium festgestellt. Insbesondere für leicht polare Dienliganden verbesserte die durch die Mikroemulsion bedingte dirigierende Nanostrukturierung die Reaktionsgeschwindigkeit, Ausbeute und Enantioselektivität.

Acknowledgement

I would never touch the end of such a journey without the great people who assisted me. I owe my full gratefulness to all of them for making this journey full of experience.

I express my deepest gratitude and my sincere thanks foremost to Prof. Dr. Thomas Sottmann for allowing me to conduct my research with him, who supervised me through those years and all the stages of my research. His guidance and trust were the keys to accomplish this work. I could not have finished it without his guidance and patience toward this successful research.

I would also like to thank Prof. Dr. Bettina Lotsch for giving the time and effort to examine and review my work and to provide deep perception regarding this tremendous work. I acknowledge Prof. Dr. Cosima Stubenrauch for her help and monitoring from the beginning of my thesis and for accepting to be the chairwoman during my defense.

This Ph.D. study would not have been possible without the generous financial support of the Konrad Adenauer Stiftung scholarship. A very special thanks and deep appreciation to the KAS foreign-students office and the committee for giving me this huge opportunity. Special thank goes to Dr. h. c Berthold Gees for his personal mentoring.

A special and warm thanks to Dr. Petia Atanasova and to Prof. Dr. Joachim Bill for the successful collaborations. The fruitful discussions and the intensive work with Dr. Atanasova were precious and very valuable. I also want to thank Prof. Dr. Sabine Laschat, Max Deimling and Manuel Kirchoff for the constructive collaboration. Your efforts made me come to this phase.

A million thanks to my students, Karina Abitaev, Barbara Schwager and Andreas Greulich, who were a part of this research and put a thumbprint in accomplishing this study.

I am grateful to Dr. Gunther Richter and Hilda David for their assist and support with the SEM and EDX measurements. To Dr. Carsten Müller and Gabriele Bräuning I am grateful for their help in the SAXS measurements and DSC measurements, respectively. I would also like to mention and acknowledge Dr. Angelika Manner at the University of Vienna for the aid regarding the density measurements.

A warm appreciation goes to the CRC 1333 team for generous supporting me during my studies in all the aspects and allowing me to attend several conferences to increase my knowledge.

For the people who reviewed my thesis. I want to express my gratitude and thankfulness to Prof. Thomas Sottmann, Karina Abitaev, Katja Steck, Dr. Petia Atanasova, Shih-Yu Tseng, Sebastian Andrieux, Manuel Kirchoff for taking the time to review this work.

A special thanks to Abdalrahman Alshorafa for his effort in the 3D-drawings. He is a friend who I could and I can count on when things were hard for me.

I am very grateful to Diana Zauser and Birgit Feucht for their support in laboratories. I am also thankful to Boris Tschertsche, Daniel Relovsky and Thomas Weigand from the electronic and mechanical workshops for their help by maintaining the high-pressure cells and solving technical problems.

Many thanks to my past and present colleagues of the Sottmann group Dr. Stefan Lülsdorf, Harun Bilgili, Kristina Schneider, Shih-Yu Tseng, Julian Fischer and Karina Abitaev, as well as to my colleagues of the Stubenrauch group for the years I have spent with them. It was full of experience, laughter, and joy. I would never forget those years.

Furthermore, I would also thank my officemates for having me for those years and creating a lovely atmosphere.

I would like to thank my friends who supported me during these years and being there whenever I needed them.

Most significantly, I sincerely and profoundly thank my support system, my parents, my brothers and my sister for being always there since I was a kid until this moment. Without them, it was never possible to reach this phase.

Content

1 Introduction

1.1. Motivation

Nowadays, catalysis plays a fundamental role in chemical synthesis and makes up about 80 % of all the chemical processes in pharmaceutical, agrochemical, and chemical industry [1]. Catalysis can be classified as heterogeneous, if the catalyst acts from a different phase than the substrates, or as homogeneous, when both the catalyst and the substrates are in the same phase. One remarkable advantage of homogeneous catalysts over heterogeneous is their high selectivity with respect of the synthesis of the desired product. Homogeneous catalysis is subdivided in various classes. An important class is the transition-metal/organometallic catalysis, in which a metal atom surrounded by ligands acts as a catalytic active center. The fact that three Nobel prizes in chemistry (2001, 2005, 2010) have been awarded to scientists for their contributions to organometallic catalysis in the last two decades, manifest the importance of organometallic catalysis in chemistry. The development of organometallic catalysis led to the discovery of new reactions that were considered impossible before [2]. That one can easily obtain molecular-scale information (via spectroscopy techniques) about the active catalyst (metal/ligands complex), helps in understanding the catalytic mechanism [3,4]. This in turn enables the further enhancement of the catalytic selectivity and/or activity of a certain active center by tuning the electronic and/or the steric properties of the ligand [5].

However, a rational catalyst-by-design strategy for specific chemical transformations has still not been well-established so far and catalyst screening is still the core principle to discover new catalysis pathways. Additionally, even though some of the homogeneous organometallic complexes exhibit high catalytic performances, they are difficult to separate intact from the reaction medium. This problem becomes even more crucial in case of asymmetric catalysts, which are based on expensive chiral ligands. Thus, although the activity of homogeneous organometallic catalysts is exceptionally high compared to the heterogeneous one, their economical, toxicological, and environmental impacts are challenging.

Further improvements in the field of organometallic catalysis were inspired from biocatalytic systems, i.e. enzymes [6]. These biocatalysts possess a catalytic cavity, in which

the catalytic center is located as shown in Figure 1.1. The confinement of the catalytic center in the cavity, firstly ensure the proximity between the substrate and the catalysts, thereby enhancing the overall reaction. Secondly, the environment around the active site influences the substrate binding, which in turn leads to high selectivity. Thirdly, enzymes can pre-orient the substrate in a high energy conformation, which results in an increased reactivity [7].

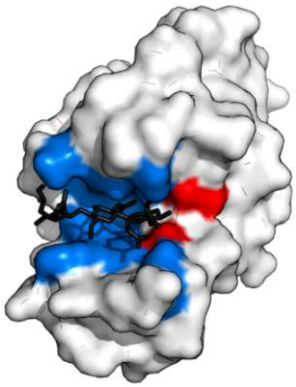

Figure 1.1: Schematic representation of an exemplary enzyme structure showing the confined cavity around the active center. The substrate (black) is bounded at the binding sites (blue) to pre-orient it next to the catalytic center (red). Taken from [8].

Inspired by this beneficial impact of confinements in biocatalytic systems, there is a rising interest in concepts, that enable both homogeneous and heterogeneous catalysis in confined spaces [9,10]. On the one hand, in heterogeneous catalysis the confinement effects have been reported in several studies based on materials containing confined-cavities, which are intrinsically catalytic active, such as zeolites [11], metal-organic frameworks (MOFs) [12], and covalent-organic frameworks (COFs) [13]. On the other hand, in homogeneous catalysis the influence of confinement on reactivity and selectivity has been investigated utilizing cyclodextrins [14], self-assembled container molecules [9,15], micellar-based systems [16], water-in-oil, oil-in-water microemulsions [17] and much more [18].

In the meantime, a strategy which combines heterogeneous catalysis and homogeneous organometallic catalysis is attracting more and more attention. Here, molecular catalysts, known from homogeneous settings, are immobilized in a porous support material via linker groups. This strategy, which is also called "molecular heterogeneous catalysis", aims to combine the high activity and selectivity of molecular homogeneous catalysis with the advantages of heterogeneous catalysis, i.e. simplicity in removing and reusing a catalyst [19]. Furthermore, the porous structure of the support materials enables a beneficial impact on

reactivity and selectivity through confinement effects. Suitable pore-containing support materials are porous polymers, porous carbon materials and porous inorganic carriers (silicates, alumosilicates, etc.) as well as porous organic/inorganic hybrid materials. In this context, an influence of the confinement on the catalysis is only expected when the size of the pores d_{pore} is only slightly larger than the dimensions of organometallic catalysts (~1 nm). This means that mesoporous materials ($2 < d_{pore}/nm < 50$) are the most suitable supports. The cavities in macroporous materials ($d_{pore} > 50$ nm) are too large to induce confinement effects, while micropores ($d_{pore} < 2$ nm) are too small to accommodate the catalyst and to enable efficient mass transport.

Motivated by the aspects discussed above, the collaborative research center (CRC 1333) "Molecular Heterogeneous Catalysis in Confined Geometries" has been established at the University of Stuttgart in 2018 to explore the influence of the confinement on selected organometallic-catalyzed transformations in organic chemistry, i.e. transfer hydrogenation, olefin metathesis, and asymmetric addition. The respective organometallic catalyst will be immobilized through a linker group in the mesopores of different support materials possessing pores with various size and geometry as well as polarity. Within the CRC, several materials like COFs, mesoporous silica, carbons, polymers, and organic/inorganic hybrid materials are planned to be used. Among them, porous polymers and mesoporous organic/inorganic hybrid materials seem to be advantageous with respect to upscaling. Furthermore, conventional and thus cheap polymers, surfactants, and CO_2 are used to produce the mesoporous polymers.

Only a limited number of methods have been suggested for the synthesis of porous polymers/polymer foams exhibiting a pore size $d_{pore} < 100$ nm [20,21]. Among these the "Nanofoam by Continuity Inversion of Dispersion (NF-CID) method" seems to be particularly promising as it should allow for the large scale production of thermoplastic nanoporous polymers for thermal insulation application [22].

However, a potential weakness of porous polymers in catalysis is their instability against harsh organic solvents and high temperatures. A feasible way to overcome this weakness, is the mineralization of porous polymers with metal oxides via the chemical bath deposition (CBD) method. In this way porous organic/inorganic hybrid materials can be synthesized via the formation of a metal oxides layer on the pore walls of the porous polymers.

Attaching organometallic catalysts to the inorganic layer in the pores of these hybrid materials (see Figure 1.2) would then allow to study the role of confinement in molecular heterogeneous catalysis (CRC 1333 project, 2019).

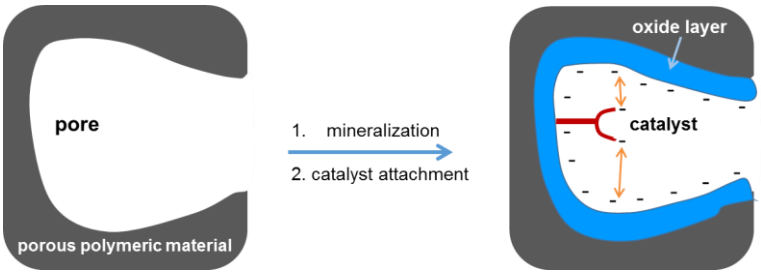

Figure 1.2: Schematic representation of the synthesis of organic/inorganic mesoporous hybrids as a support material for investigating the molecular heterogenous catalysis in confined spaces. (CRC 1333 project, 2019).

However, before carrying out catalytic reactions in these functionalized mesoporous hybrid materials, the diffusion of the reactants and products into and out of the pores has to be considered. According to Sastre and Corma, the diffusion will depend on the size and the shape of the pore, the size of the diffusing molecule as well as the attractive and repulsive interactions between the pore walls and the diffusing molecules [11]. Thus, limited diffusion will critically affect the goal to perform heterogeneous catalysis in confinement. In case both polar and nonpolar reactants or products are involved, bicontinuously structured microemulsion consisting of polar and nonpolar nanodomains interwined in a sponge-like fashion might facilitate the transport of molecules with different their polarities.

1.2. Task Description

From the preceding introduction the following two scientific question/issues emerge as main objectives of this thesis. The main objective of the first part is the synthesis of open-cellular porous polymers organic/inorganic hybrid materials with a pore size $50 < d_{pore}/nm < 250$, while the second part deals with the formation and use of bicontinuously structured microemulsion as reaction media for homogeneous organometallic catalysis. Both type of systems, the porous materials (polymers and hybrids) and microemulsion provide confined spaces which might be of beneficial impact for the reactivity and selectivity of catalytic reactions. While, the confinement is of solid nature in the former type systems, it is liquid in the latter.

For the synthesis of the porous polymer the NF-CID method was chosen, which bases on the foaming of colloidal crystals of polymer nanoparticles with supercritical CO_2. To optimize the structure of the porous polymer with respect to pore size and morphology, the influence of the size, polydispersity and glass transition temperature of the polymer nanoparticles on the obtained porous material had to be investigated. For further optimization, the influence of the NF-CID parameters, i.e. temperature, exposure time and course of expansion on the obtained porous polymers had to be studied in a second set of experiments. To enhance the stability of the porous polymers against the harsh reaction conditions, i.e. organic solvents and high temperature, the obtained porous polymer planned to be used as template to synthesize mesoporous organic/inorganic hybrids via the CBD method.

To explore the effect of liquid confinement of bicontinuous microemulsions on homogeneous organometallic catalysis, the Rh-catalyzed asymmetric arylation of *N*-tosylimine **1** with boroxine **2** had to be studied. Therefore, a reaction-specific nanostructured microemulsion with equal amounts of water and toluene had to be formulated and characterized. The Rh-catalyzed arylation and kinetic studies of the reaction applying (Rh/ligands) complexes with different polarities had to be conducted and compared to conventional homogeneous conditions to determine the influence of the liquid confinement. These results may become of great value when bicontinuous microemulsions applied as a reaction media in catalyst-carrying mesoporous materials.

2 Synthesis of Porous Polymers and Porous Hybrid Materials

Porous materials, regardless whether they are intrinsically catalytic active or not, offer a huge surface area on which the catalyst can be attached. In case the pore size approach the size of the catalyst the increasing confinement is expected to induce impressive effects on enantioselectivity. With the general objective to develop mesoporous support materials for heterogeneous catalysis the first task of this thesis was the synthesis of porous polymers and porous organic/inorganic hybrid materials.

This chapter starts with an introduction on porous materials in general. Then the methods used for the synthesis of porous polymers with pore size smaller than 1 micron are presented. Thereby, a special focus is dedicated to the foaming of polymers with supercritical CO_2. Thereafter, the NF-CID method, used in this thesis to produce the porous polymers, will be introduced. The second section deals with the synthesis of porous polystyrene and influence of polystyrene nanoparticles, their polydispersity, and glass transition temperature as well as the NF-CID parameters; temperature, exposure time, and expansion step on the pore size and morphology of the obtained porous polystyrene. The chapter ends with the mineralization of the synthesis of porous PS/ZnO hybrid materials, which not only exhibit an improved stability but also allow to finetune the pore size.

This chapter is based on the following publications:

Y. Qawasmi, P. Atanasova, L. Grassberger, T. Jahnke, Z. Burghard, R. Strey, J. Bill, T. Sottmann, Synthesis of nanoporous organic/inorganic hybrid materials with adjustable pore size, *Colloid Polym. Sci.* 2018, *296*, 1805.

K. Abitaev, Y. Qawasmi, T. Sottmann, Synthesis of polystyrene nanoparticles with adjustable size and polydispersity for the production of mesoporous foams and ZnO inverse opals, in preparation.

Author Contributions:

The author was assisted by Mrs. Karina Abitaev and Dr. Petia Atanasova. K. Abitaev partially synthesized the polymer nanoparticles and partially studied the effect of the template on the porous polymers. Dr. P. Atanasova performed the mineralization reactions.

2.1. Porous Polymers

Inspired by the architecture and the sophisticated properties of natural porous materials such as bones, honeycombs with hexagonal cells, sponges, coals and hollow bamboos, uncountable porous materials have been synthesized in the last decades. Nowadays synthetic porous materials are used in numerous fields of application such as in gas storage [23], as separation materials [24], heat insulation [25,26], encapsulation agents for drug delivery systems [27], in catalysis [28], supports for catalysts [29] and sensors [30], templates for structure replication [31], packing materials [32] and many others [33].

2.1.1. Terminology

Porous materials are, simply put, materials containing pores, which can be cavities, channels or interstices. The porous structure of these materials leads to special physical and mechanical properties such as lightweight, shock absorption, high internal surface area, and many more. Depending on the nature of the matrix, porous materials can be categorized into porous metals, porous ceramics, porous glasses, and polymer foams/porous polymers [34]. The synthesis and characterization of the latter type of porous materials is the scope of the thesis at hand. Pore-containing polymers are widely discussed in literature and described using different terms such as porous polymers [20], polymer foams, cellular foams, cellular polymers [35] and cellular sponges [36]. For the sake of clarity, the term "porous polymers" will be used in this thesis.

According to the pore diameter, IUPAC classifies porous polymers into three categories: microporous polymers (pore size smaller than 2 nm), mesoporous polymers (pore size in the range of 2-50 nm), and macroporous polymers (pore size larger than 50 nm) [37]. However, the terms nanoporous polymers and nanofoams are frequently used in the literature as well to describe porous polymers with a pore size below one micron [38,39].

Beside their size, the pores can further be classified according to their accessibility with respect to an external fluid. Closed pores are totally isolated from their surroundings, as sketched in Figure 2.1 (a). Open pores, in contrast, have a continuous channel of communication with the surrounding as sketched in Figure 2.1 (b-f). Pores which are only open at one end, as for example the pores shown in Figure 2.1. (b) and (f), are known as blind or dead-end pores. In case pores are open at two ends (see Figure 2.1. (e)), they are named as through or passing pores [40].

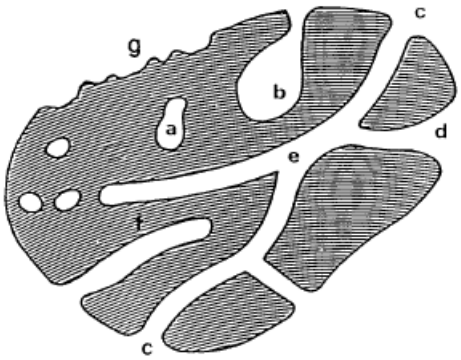

Figure 2.1: Schematic cross-section of a porous material allowing a classification of the pores according to their accessibility to the surroundings: (a) closed pores, (b, f) open pores at one end – blind pores, (c, d, g) open pores and (e) open pores at two ends – passing pores. Taken from [40].

2.1.2. Synthesis of Nanoporous Polymers

Because of their properties, i.e. thermal, mechanical, large surface areas, and well-defined porosity, as well as their multifaceted applications, the synthesis of porous polymers became an attractive research area for scientists in academia and industry. The overall goal was and still is the development of cheap, efficient, and environmentally friendly methods to synthesize well-defined porous materials along with the control over their pore size, pore size distribution and functionality. One of the main motivations for the synthesis of new porous polymer materials with small pore size is their usage in thermal insulation applications. According to Knudsen [41], the gaseous heat conductivity almost vanishes when the pore size approaches the mean free path Λ of gas molecules, which is defined as the average traveled distance of two molecules between two collisions. For air at ambient temperature and pressure the mean free path approximates to 70 nm [42]. Thus, porous polymer materials with a pore size smaller than 100 nm would provide a comparable thermal insulation efficiency to vacuum insulation panels (VIPs) and aerogels, which are difficult to fabricate and therefore expensive.

A number of different approaches have been proposed and applied to produce nanoporous materials with pore size smaller than one micron like templating [43], self-assembly [44], phase separation [45], and foaming [46]. In the following some of the approaches will be briefly described.

Porous polymers via block copolymer self-assembly

One approached towards nanoporous polymers and porous carbon utilizes the self-assembly of amphiphilic block copolymers. Amphiphilic block copolymers (BCs) are macromolecules consisting of two or more homopolymer chains covalently linked together. Depending on the chemical miscibility and the volume fraction (f_A) of the constituting blocks, the copolymers can self-assemble into a variety of thermodynamically stable and ordered nanostructures. For instance, diblock copolymers can form various microphase morphologies to minimize the contact energy between the incompatible segments. These morphologies vary from spheres (S), cylinders (C), double gyroid (G), lamellae (L), and their inverse structures, as shown in Figure 2.2. [44,47]

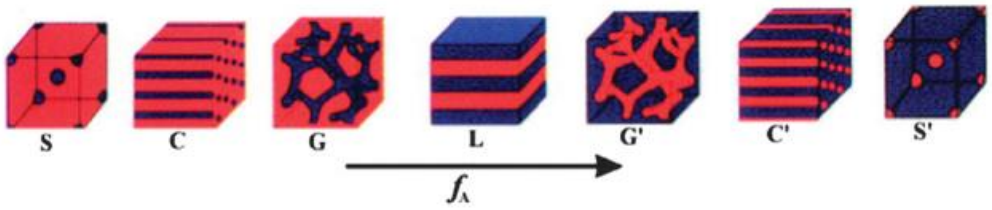

Figure 2.2: Various microphase morphologies formed by diblock copolymers depending on the volume fraction (f_A) of one block (blue block). The morphologies varies from spheres (S), cylinders (C), double gyroid (G), lamellae (L) and their inverse structures (G', C', S'). Taken from [47].

In order to obtain a porous material, the microdomains of the minor (sacrificial) component are selectively removed by etching techniques. Following this method, the pore size of the obtained material depends directly on the molecular weight of the sacrificial block. It was showed that porous material with a pore size ranging from 5 nm to 50 nm are accessible [48]. Pore morphologies, which are easy to realize are cylindrical and gyroid structures. However, the synthesis of materials exhibiting closed-cell pores turned out to be not easy due to the difficult full removal of the sacrificial component.

Porous polymers via swelling

In a different approach to produce porous polymers, a polymer network swollen by a solvent mixture is solidified via specific evaporation of one solvent. Following this approach, sketched in Figure 2.3, Grassberger et al. recently produced porous poly(methyl methacrylate) (PMMA) with pore size down to 80 nm for insulation application [45]. To obtain these porous polymers, a crosslinked polymer network (I) is swollen by a mixture of two miscible solvents (II). One of these solvents is a swelling agent (e.g. acetone) that adsorbs into the polymer network and decreases its glass transition temperature T_g. The other solvent is a non-swelling agent (e.g. cyclohexane) that exhibit a lower vapor pressure than the swelling agent. Evaporating the swelling agent, the non-swelling agent remains in the network (III). As a consequence of the evaporation of the swelling agent, T_g of the polymer increases and the polymer chains solidify (IV). The pores of the swollen crosslinked polymer undergo a slight volume reduction but are still expanded due to the presence of the non-swelling solvent. After evaporating the non-swelling agent, one obtains a solvent-free nanostructured porous polymer. Although this method yields highly porous polymer materials with adjustable pore size, the large amount of organic solvents needed for the production might be a cost and environmental issue.

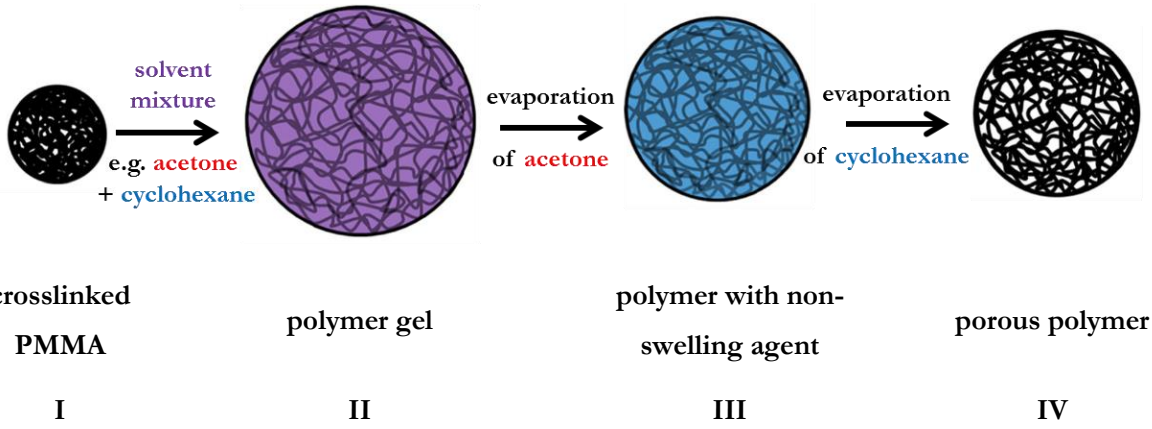

Figure 2.3: Schematic representation of the blowing agent free foam formation process proposed by Grassberger et al. A crosslinked polymer network (I) is swollen in a mixture of two solvents (II); one swelling agent (e.g. acetone) and one non-swelling agent (e.g. cyclohexane). After evaporating acetone (III), cyclohexane remains in the network so that the polymer undergoes a slight volume decrease and T_g of the polymer increases by which the polymer chains solidify. Evaporating the cyclohexane the porous polymer is generated (IV). [45]

Porous Polymers via Foaming using Physical Blowing Agents

The third method utilizes a blowing agent to nucleate in a polymer melt, which after an expansion step form pores in the polymer matrix. This method known as foaming using a blowing agent is widely used and investigated method, therefore, it will be described in detail in the next paragraphs.

Chemical or a physical blowing agent are commonly used to produce porous polymers. Chemical blowing agents are chemicals that produce gases during the foaming process via a chemical reaction, e.g. isocyanate and water for polyurethanes, or sodium bicarbonate and azo-, hydrazine-based compounds for thermoplastic polymers. In contrast, physical blowing agents are gases that are added to a polymer/polymer melt, in which they exhibit a reasonable solubility. Common physical blowing agents are nitrogen, carbon dioxide and volatile hydrocarbons such as propane, butane, as well as low boiling chlorofluorocarbons (CFCs), and hydrochlorofluorocarbons (HCFCs). However, the use of CFCs and HCFCs as blowing agents has been prohibited because they cause ozone layer depletion [49]. Whereas, the use of use CO_2 in foaming technique has several advantages since it is an environmentally friendly gas, its supercritical state is accessible and has a reasonable solubility in organic polymers. Many porous polymers have been obtained using CO_2 as a blowing agent such as PMMA [50,51], polystyrene [52], polycarbonate [53], poly(ethylene terephthalate) [54], polylactic acid [55] and poly(ε-caprolactone) [56] and many others.

Foaming using CO_2 as a blowing agent

Basically, this foaming process can be divided into three stages as shown in Figure 2.4. Firstly, CO_2 is added to a thermoplastic polymer under high pressure. Then a polymer-melt saturated with CO_2 (polymer/fluid mixture) is obtained upon heating the mixture above its glass transition temperature ($T > T_g$) at high pressure. In the next step, the polymer/fluid mixture is quenched into a super-saturated state by either reducing the pressure or increasing the temperature. Thereby, CO_2 cells/clusters are nucleated (homogeneously or heterogeneously) in the polymer matrix and grow until the systems transfers from the rubbery to the glassy state [57].

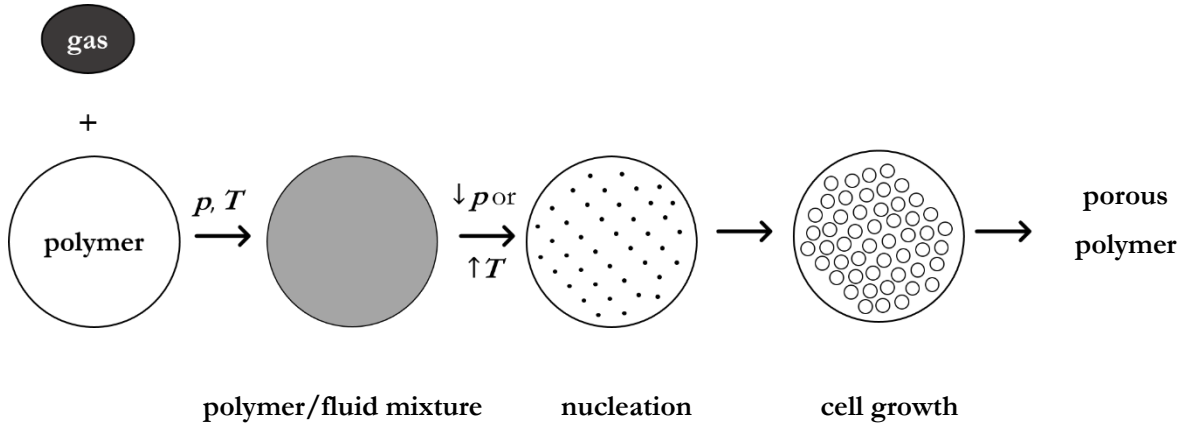

Figure 2.4: Foaming of thermoplastic polymers using physical blowing agents. The process involves three steps: (1) Dissolution of the gas in the polymer at a certain temperature and pressure. (2) Nucleation of gas cells/clusters driven by the supersaturation as a result of an increase of temperature or a decrease in pressure. (3) Cell growth until the system exceeds the T_g of the polymer. Redrawn from [57].

The nucleation of the gas cell/clusters takes place either homogeneously or heterogeneously. Due to its importance in the foaming process, it will be discussed in the following paragraphs.

- **Homogeneous Nucleation:**

In case of single-phase polymers and a pure gas, the mechanism of nucleation and cell growth is described by the classical homogeneous nucleation theory. Regard the nucleation stage, the classical homogeneous nucleation theory states that in a closed isothermal system the difference of the free energy of a system due to the formation of a gas nucleus in the polymer matrix is the sum of the free energy (ΔG) gained from the formation of the new phase and the required free energy for the creation of the interface between gas cells and polymer matrix, which is given by [58]:

$$\Delta G_{\text{hom}} = -\frac{4\pi r^3}{3}\Delta p + 4\pi r^2 \sigma \tag{1}$$

where r is the radius of the spherical gas cell, σ is the interfacial tension between the gas and the polymer and Δp is the pressure difference between the two sides of the interface. By plotting ΔG against the cell radius, a curve that has a maximum at the critical radius r^* is obtained (see Figure 2.5):

$$\frac{d\Delta G}{dr} = 0 \;\Rightarrow\; r^* = \frac{2\sigma}{\Delta p} \tag{2}$$

Then the maximum value of ΔG for homogeneous nucleation is:

$$\Delta G^*_{\text{hom}} = \frac{16\pi\sigma^3}{3\Delta p^2} \tag{3}$$

The rate of nucleation N_0 can be described by the following equation:

$$N_0 = C_0 f_0 e^{\left(\frac{-\Delta G^*_{hom}}{kT}\right)}, \tag{4}$$

where k is the Boltzmann constant, C_0 the fluid concentration dissolved in the polymer matrix and f_0 the frequency factor of fluid molecules, which describes the rate at which nuclei with a critical radius are transformed into stable pores.

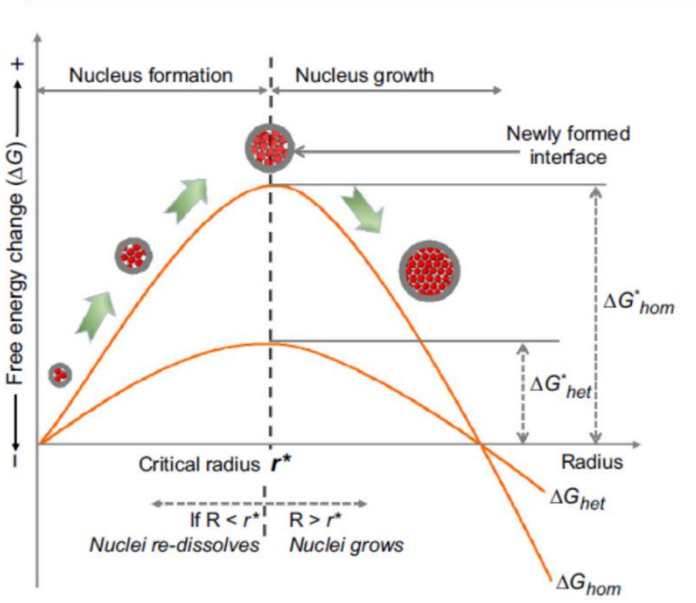

Figure 2.5: Schematic representation of free energy change ΔG as a function of the nucleus radius of both homogeneous (ΔG_{hom}) and heterogeneous nucleation (ΔG_{het}). The figure shows the nucleation and growth stages. Adapted from [39]

The second crucial stage of CO_2 foaming is the cell growth, in which the formed nuclei transfer into foam bubbles. During the growth stage the dissolved gas in the polymer/gas matrix diffuses to the nucleated sites with $r \geq r^*$. The driving force behind this stage is the pressure difference between inside and outside the gas cells, which acts against surface and viscous forces. The rate of cell growth is generally described using the following equation [59]:

$$\frac{dr}{dt} = \frac{r}{4\eta_{matrix}}\left(\Delta p - \frac{2\sigma}{r}\right), \tag{5}$$

where η_{matrix} is the viscosity of the polymer/gas matrix.

From equation (5) it becomes clear that the viscosity of the polymer/gas matrix at the processing temperature plays also an important role determining the growth extent. For instance, in the conventional CO_2 foaming process, the viscosity of polymer/gas matrix is very low during the cell growth since it proceeds at temperatures higher than the glass transition temperature of the neat polymer. This allows the growing gas cell inside the polymer matrix to expand for longer times, which leads to the production of porous polymers with micropores and cell densities lower than 10^{11} cm^{-3} [46].

In order to apply the nucleation theory, the microscopic thermodynamic parameters Δp, σ, η_{matrix} and C_0 must be determined. These parameters are very difficult to measure directly via conventional methods. Therefore, Tsivintzelis et al. [60] modeled the key thermodynamic properties of polystyrene/$scCO_2$ with the Non-Random Hydrogen Bonding (NRHB) theory [61] and combined them with the classical homogeneous nucleation theory. By comparing the theoretical and the experimental results, they showed that at specific conditions, namely temperature and pressure, which refer to a constant initial energy barrier for nucleation $\left({}^{-\Delta G^*_{hom}}/_{kT}\right)$, all the produced porous polymers have similar pore diameters and cell population densities within the studied temperature range.

Furthermore, it has been proved mathematically that it is necessary to nucleate, grow, and stabilize 10^{14}-10^{16} nuclei/cm^3, to successfully produce lightweight porous polymers with pore sizes below 200 nm [21,62]. Thus, based on equation (4), to create this large number of nucleation sites, a high concentration of dissolved $scCO_2$ is fundamental.

The effect of dissolving higher amounts of $scCO_2$ on decreasing the pore size and increasing the cell density has been proved several times, particularly on producing porous polymer with pore size above 1 μm. For instance, starting with the same polymer and increase the solubility of $scCO_2$ in the polymer matrix by increasing the pressure while keeping the temperature constant, leads to the production of porous polymers with smaller pore sizes. This behavior has been investigated on polystyrene [52,60], PMMA [50], polycarbonate [63], and many more [64,65].

A vital factor determining the solubility of $scCO_2$ in the polymer matrix is the polymer nature and its affinity to CO_2. For example, using CO_2-philic polymers like fluorine-containing polymers, silicone-based polymers, acrylate and acetate polymers facilitate the production of porous polymer with smaller pore sizes. Reglero et al. [66] have investigated the CO_2 uptake of PMMA compared to polystyrene between 25 to 80 °C under 300 bar after 16 h. They showed that within this temperature range the CO_2 uptake of PMMA is more than 16 wt% while it is about 10 wt% for polystyrene. Shieh and Liu [67] performed a similar study over a wide pressure range from 35 to 350 bar, which shows that the interaction of PMMA and CO_2 is better due the existence of the carbonyl group in PMMA. For this reason, almost all the successful produced single-phase porous polymers via $scCO_2$ foaming with pore size smaller than one micron reported in the literature are based on high

CO_2-philic polymers such as acrylate polymers [68–70], polyetherimides (PEI) [71,72], polyethersulfones (PES) [71], and polyimides (PI) [73].

Therefore, many studies tried to enhance the CO_2 uptake of low CO_2-philic polymers by blending these polymers with high CO_2-philic polymers. Therewith, the number of nucleation sites can be increased. The properties of the produced porous polymers can be optimized by adjusting the blend ratio between the polymers. Otsuka et al. [74] prepared a polymer blend composed of highly dispersed nanoscale PMMA domains in a PS matrix by polymerizing MMA monomers in the PS matrix. After foaming the blend with CO_2 at room temperature, a porous polymer with average pore size of 40-50 nm was achieved. However, the pore structure was quite heterogeneous and not defined. Costeux et al. [75] prepared polymer blends of a styrene-acrylonitrile copolymer with poly(ethyl methacrylate) or poly(methyl methacrylate-co-ethyl acrylate) by thermal mixing. After foaming, the best porous polymers with average pore sizes below 100 nm were obtained from miscible blends.

- **Heterogeneous Nucleation:**

Another way to increase the number of nucleation sites is the foaming of nanocomposites, which form after addition of nucleating agents/nanofillers to a polymer matrix. Several nucleating agents have been employed for this approach, e.g. silica, aluminum oxide, zinc oxide nanoparticle, polyhedral oligomeric sislesquioxanes (POSS), carbon nanotubes, graphite and nanoclays. In case of nanocomposites, one talks about heterogeneous nucleation instead of homogeneous nucleation, since the use of this nanomaterials reduces the initial energy barrier for nucleation (see Figure 2.5). The heterogeneous nucleation rate is determined by the following energy barrier:

$$\Delta G^*_{\text{het}} = \frac{16\pi\sigma^3}{3\Delta p^2} f(\theta) \tag{6}$$

where $f(\theta)$ is the ratio between homogeneous and heterogeneous nucleation. This ratio is always less than one and depends on the wetting angle of the polymer-additive-gas interface [76].

Siripurapu et. al. [77] investigated the foaming behavior of films of PMMA and 10 nm silica nanoparticles using $scCO_2$. They reported that in the presence of nanoparticles the pore

sizes were smaller with higher pore densities as compared to the neat PMMA. Realinho et. al. [78] used organically modified montmorillonite oMMT as nucleating agent for a PMMA matrix. The experiments showed that upon the addition of oMMT the pore size of the obtained porous polymers reduced significantly from 8.1 μm (without oMMT) to 290 nm (10 wt% oMMt) associated with increasing pore densities. Another study was carried out on polylactide-based nanocomposites by Ema et. al. [55]. The results showed that the incorporation of nanoclay, which induced the heterogeneous nucleation, led to the production of porous polymers with an average pore size of 200 nm. In summary, the addition of nucleating agents led to an enhanced number of nucleation sites in many cases. However, the benefit of this approach is more significant in case of CO_2-philic matrices.

To sum up, there are two main challenges to produce porous polymers with pore sizes lower than 100 nm via $scCO_2$ foaming method. The first challenge is to create a high number of nucleation sites in the polymer matrix, which is associated with a very long saturation time (several days or weeks). The second challenge is that one must avoid the coalescence of the growing cells.

2.2. Nanofoams by Continuity-Inversion of Dispersion (NF-CID)

Recently, Strey and Müller [22] developed a new method called "Nanofoam by Continuity Inversion of Dispersion" (NF-CID) that combines the template strategy with the conventional CO_2 foaming. In this method, colloidal crystals of polymer nanoparticles instead of the compact polymer block are subjected to scCO_2 at high pressure. Thereby the voids between the polymer nanoparticles serve as nucleation sites, which transform into foam bubbles after the foaming. Using polymer nanoparticles, the number of voids in the colloidal crystal is of the order of 10^{16} cm^{-3}, which ensures the availability of a high number of nucleation sites in polymer matrix.

The method can be divided into five steps (see Figure 2.6): Firstly, thermoplastic polymer nanoparticles of adjustable size ($d_{part} \geq 20$ nm) and narrow size distribution are synthesized via emulsion [79,80], miniemulsion [80], or microemulsion [81,82] polymerization (step **1**). Hereafter, the nanoparticle dispersion is dried by evaporation of the solvent (step **2**). Eventually, a colloidal crystal consisting of close-packed nanoparticles is formed. In step **3**, the voids between the particles are filled with a supercritical fluid (sc-fluid), e.g. CO_2, at an adjustable temperature and pressure. Because of the small size of the nanoparticles and the huge internal surface area of the colloidal crystal, the sc-fluid molecules diffuse almost instantaneously into the polymer nanoparticles. Time-resolved small angle neutron scattering (SANS) measurements showed that colloidal crystals of PMMA nanoparticles are saturated within 30 s [83]. Due to the saturation of the polymer nanoparticles with the sc-fluid, the glass temperature T_g of the respective polymer is considerably reduced. Thereby, the lowered glass temperature T_g^* depends strongly on the solubility of a given sc-fluid in the polymer, which is a function of temperature and pressure [67]. For instance, PMMA which exhibits a glass temperature T_g of 105 °C transfers to the rubbery state already at $T = 40$ °C, if it is exposed to CO_2 adjusting a pressure of $p \geq 60$ bar [84]. In step **4** (continuity inversion), the temperature is increased above the T_g^* of the polymer nanoparticles saturated with the sc-fluid at the respective pressure. Thus, the polymer particles lose their spherical shape and form a connected polymer matrix. Due to the high interfacial tension between the sc-fluid and the saturated polymer matrix, the octahedral and tetrahedral voids (ideal packing) filled with sc-fluid transform to spherical nanodroplets in the highly viscous polymer matrix to minimize the interfacial energy. After a certain exposure time (t_{exp}), (step **5**) the pressure is released to 1 bar at a temperature above the

critical temperature of the blowing agent T_c, the density of the sc-fluid changes gently from liquid-like to gas-like. Accordingly, each spherical nanodroplet transforms gradually into a larger pore. At the same time, the polymer matrix solidifies due to the rapid increase of the polymer's glass transition temperature to its original value, caused by the diffusion of sc-fluid molecules out of the polymer.

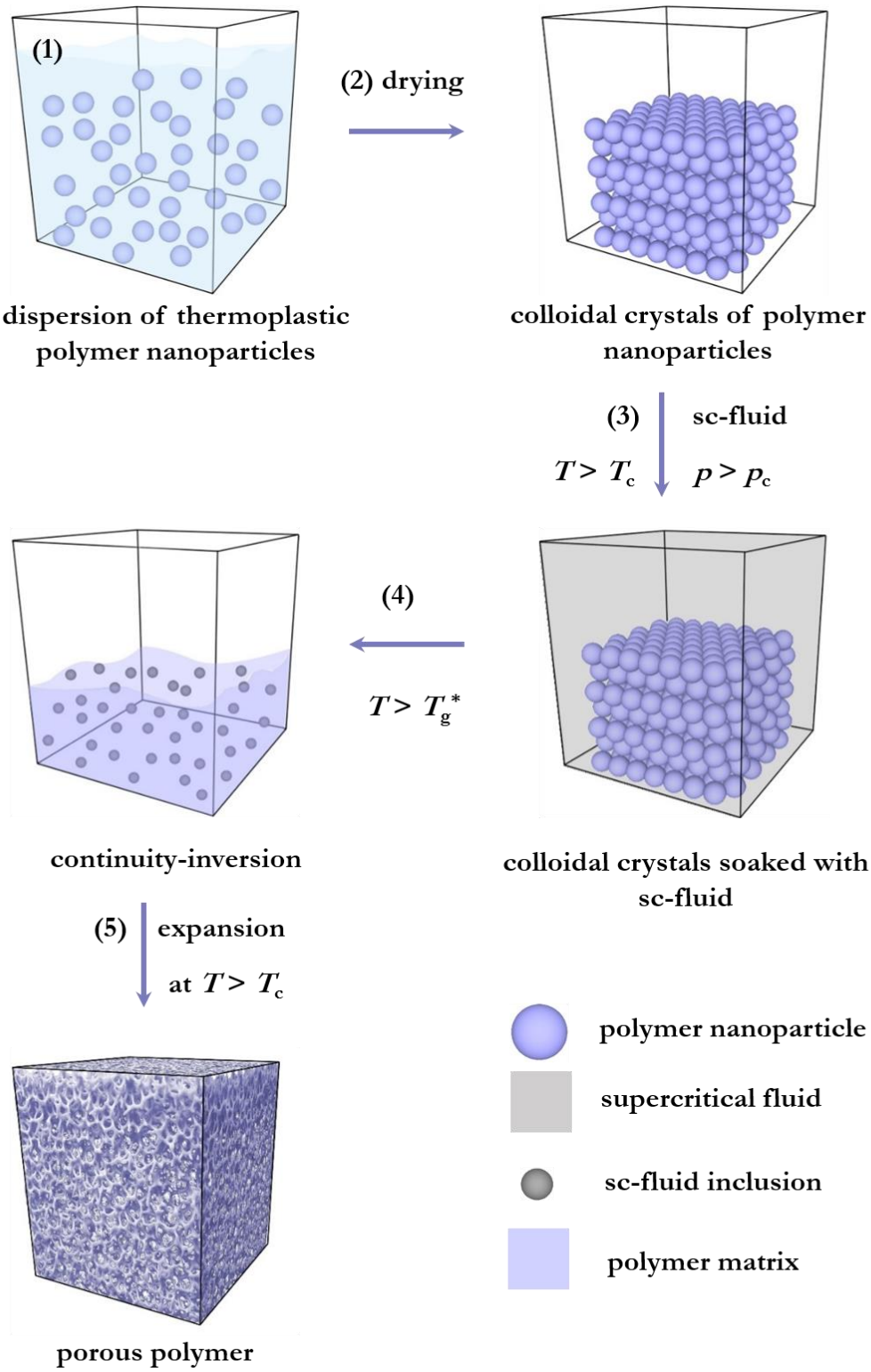

Figure 2.6: Schematic representation of the NF-CID principle. (1) Synthesis of thermoplastic nanoparticles by emulsion, miniemulsion, or microemulsion polymerization. (2) Drying of the dispersion results in closed-packed nanoparticles, which are in step (3) filled with a sc-fluid, decreasing the T_g of the polymer. (4) Increasing the temperature above the lowered T_g^*, the voids between the particles filled with the sc-fluid transform into spherical nanodroplets in the highly viscous polymer matrix. (5) The expansion of the system at $T > T_c$ leads to both foaming and fixation of the polymer. Redrawn from [85].

Müller and Strey stated that one can predict the pore size of the produced porous polymer by just knowing the particle size of the used nanoparticles, temperature and pressure at which the foaming takes place. By assuming spherical geometry, the diameter of the spherical nanodroplets d_{scfluid} in the highly viscous polymer matrix is directly related to the diameter of the polymer nanoparticles d_{particle}, according to

$$d_{\mathrm{scfluid}} = d_{\mathrm{particle}} \sqrt[3]{\frac{N_{\mathrm{particle}} \phi_{\mathrm{scfluid}}}{N_{\mathrm{scfluid}} (1-\phi_{\mathrm{scfluid}})}} . \tag{7}$$

Here, ϕ_{scfluid} is the volume faction of the sc-fluid and N_{particle} and N_{scfluid} are the number of particles and spherical sc-fluid nanodroplets, respectively. The volume of the sc-fluid nanodroplets and pores depends on the density of the sc-fluid at high and low pressure (1 bar), i.e. $\rho_{\mathrm{scfluid,l}}$ and $\rho_{\mathrm{scfluid,g}}$. Thus, the diameter d_{pore} of a pore is given by

$$d_{\mathrm{pore,predicted}} = d_{\mathrm{scfluid}} \sqrt[3]{\frac{\rho_{\mathrm{scfluid,l}}}{\rho_{\mathrm{scfluid,g}}}} = d_{\mathrm{particle}} \sqrt[3]{\frac{\rho_{\mathrm{scfluid,l}} N_{\mathrm{part}} \phi_{\mathrm{scfluid}}}{\rho_{\mathrm{scfluid,g}} N_{\mathrm{scfluid}} (1-\phi_{\mathrm{scfluid}})}} . \tag{8}$$

From this equation it can be concluded that the pore size in the porous polymer should be directly adjustable by the diameter of the used polymer nanoparticles. Assuming that the particles are ideally close-packed and that the octahedral and tetrahedral voids are close enough to build one inclusion when the polymer becomes ductile, $N_{\mathrm{particle}}/N_{\mathrm{scfluid}} = 1$ and $\phi_{\mathrm{scfluid}} \approx 0.26$. Thus, for CO_2 an expansion from p = 250 bar to 1 bar at 80 °C results in $d_{\mathrm{pore}} \approx 5.4 \cdot d_{\mathrm{part}}$, using ρ_{CO2} (250 bar, 80 °C) = 686.6 kg.m^3, ρ_{CO2} (1 bar, 80 °C) = 1.5 kg.m^3.

The diameter of the polymer particle d_{particle} and the course of the NF-CID procedure has an impact on the pore size, geometry and homogeneity of the obtained porous polymer. Particularly the transition from sc-fluid filled voids in the colloidal crystal to nanodroplets in the highly viscous polymer matrix, i.e. continuity-inversion (step 4), and the pressure release (step 5) are crucial steps of the procedure. Both steps are highly sensitive to aging phenomena, i.e. Ostwald ripening [86,87] and coalescence [88,89], which are triggered by the minimization of the interfacial energy via a reduction of the interfacial area. However, the kinetics of these phenomena depend strongly on the viscosity of the polymer matrix, which is controlled by the distance of the adjusted temperature from the glass temperature T_g^* of the polymer saturated with the sc-fluid, as well as the exposure time and the course of expansion.

Aging Phenomena

As mentioned before, two phenomena are responsible for the aging of pores during the foaming process; Ostwald ripening [86,87] and coagulation followed by coalescence [88,89]. Ostwald ripening describes the growth of larger droplets at the expense of the smaller ones. The driving force of this process is explained by the Young-Laplace equation

$$\Delta p = p_{\text{inside}} - p_{\text{outside}} = 4\sigma / d_{\text{scfluid}} \,, \qquad (9)$$

where Δp is the Laplace pressure, p_{inside} and p_{outside} the pressure inside and outside the sc-droplet and σ the interfacial tension between the sc-fluid and polymer matrix. Figure 2.7 illustrates the ripening mechanism for sc-droplets in a molten polymer matrix. As can be seen, the molecular diffusion of CO_2-molecules from the smaller to the larger droplets is driven by the larger Laplace pressure in the smaller droplets. Thus, Ostwald ripening can be reduced by decreasing the polydispersity of sc-droplets inside the polymer matrix and by decreasing the solubility of sc-fluid in the polymer.

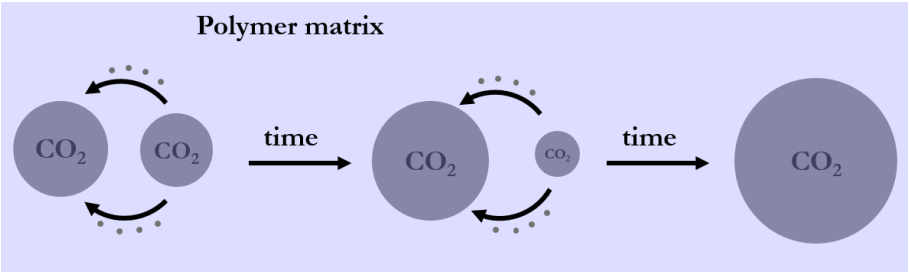

Figure 2.7: Schematic illustration of Ostwald ripening: a larger sc-droplet grows at the expense of a smaller one, due to the high Laplace pressure in the small droplets.

The coagulation of the sc-droplets is primarily determined by their diffusion, which mainly depends on the temperature, the droplet size and the viscosity of the molten polymer matrix and thus on the distance to the glass temperature T_g^* of the polymer saturated with the sc-fluid. Whether the coagulation of two droplets is followed by their coalescence (Figure 2.8), depends on the interfacial tension between the sc-fluid (here CO_2) and the polymer as well as on the rigidity of the interface. Thus, the rate of coagulation followed by coalescence can be reduced by increasing the viscosity of the molten polymer matrix and the rigidity of the interface, as well as by decreasing the interfacial tension.

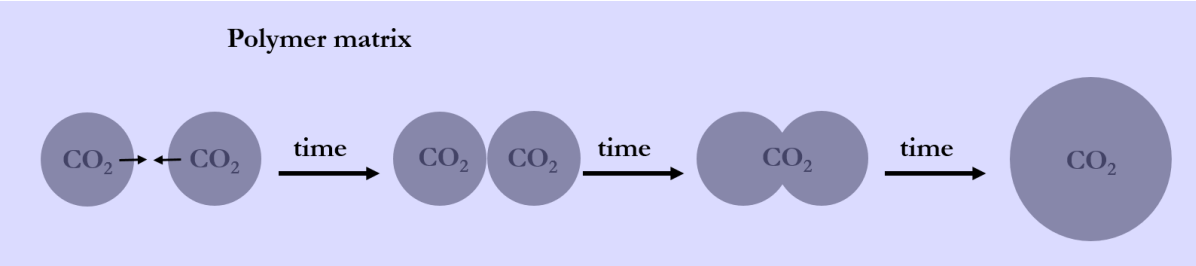

Figure 2.8: Schematic illustration of coagulation followed by coalescence. The rate of coagulation depends on the diffusion coefficient of the sc-droplets and the rate of coalescence on the interfacial tension and the interface rigidity.

2.2.1. Synthesis of Polymer Nanoparticles

As already described above, the starting point of the NF-CID method is the synthesis of spherical nanoparticles of thermoplastic polymers. In the last decades, the synthesis of spherical polymer nanoparticles has been intensively studied and many approaches have been developed [90]. Up to now, the most-commonly used and best-established method is emulsion polymerization [91,92].

Generally, polymerization is defined as a chemical reaction, in which small repeating units (monomers) react with themselves to form a macromolecule (polymer). Depending on the functionality of the monomers, there are two basic types of polymerization: (1) Step-growth or condensation polymerization, in which difunctional or polyfunctional monomers react together while eliminating low-molecular weight molecules (by-products). (2) Chain-growth or addition polymerization, where a monomer which contains at least one carbon-carbon double bond adds to another to form a polymer e.g. polystyrene (scheme 2.1). The mechanism of chain-growth polymerization involves three stages: initiation, propagation and termination. The initiation step takes place by means of an initiator which starts the polymerization. The reactive initiator can be a radical (free radical polymerization), cation (cationic polymerization), anion (anionic polymerization), or an organometallic complex (coordination polymerization). According to the environment where the polymerization proceeds, it can be further classified as: bulk, solution, suspension and emulsion polymerization. In the following description I will focus on free-radical emulsion polymerization, which I used to synthesize the polystyrene nanoparticles.

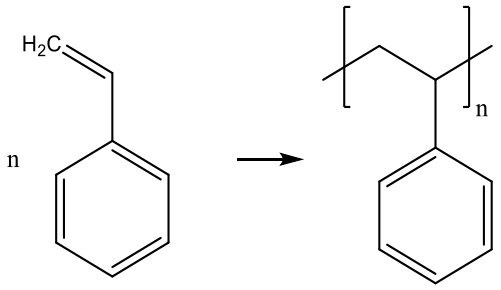

Scheme 2.1: Addition polymerization of styrene, which was used in this thesis.

2.2.2. Emulsion Polymerization

Emulsion polymerization enables the synthesis of spherical polymer nanoparticles. The main feature of this method is that polymerization takes place in an aqueous medium, in which the solubilities of both the monomer and the resulting polymer are very low. As the word emulsion implies, usually an oil-in water emulsifier (surfactant) or any surface-active species is added to stabilize the emulsion. The polymerization is started by addition of an initiator, which is usually water-soluble e.g. potassium peroxodisulfate. Water is used as a polymerization medium, due to its high heat capacity the heat generated by the exothermic free-radical reactions can be absorbed avoiding the overheating of the reaction mixture.

The physical and colloidal properties of the polymer nanoparticles produced via emulsion polymerization are highly dependent on the particle nucleation mechanism and the kinetics of the polymerization. However, understanding and quantitively describing the mechanism of emulsion polymerization is not trivial, since it is a multistep process controlled by a free radical reaction. During this process several chemical and physical events take place simultaneously in two different phases. Figure 2.9 represents the different components and structures that are present in the initial stage of emulsion polymerization. Large monomer droplets of the order of several micrometers exist in an aqueous phase containing dissolved monomer molecules, surfactants, and initiator molecules. After the activation of the initiator, oligomers are formed in the aqueous phase, leading to the formation of particle nuclei, which start to grow with time (the different mechanisms are discussed later). The surface-active species stabilizes not only the monomer droplets but also the growing polymer particles and prevent the particles from coagulation.

To understand the mechanisms and the kinetics of emulsion polymerization, considerable efforts have been made during the last decades.

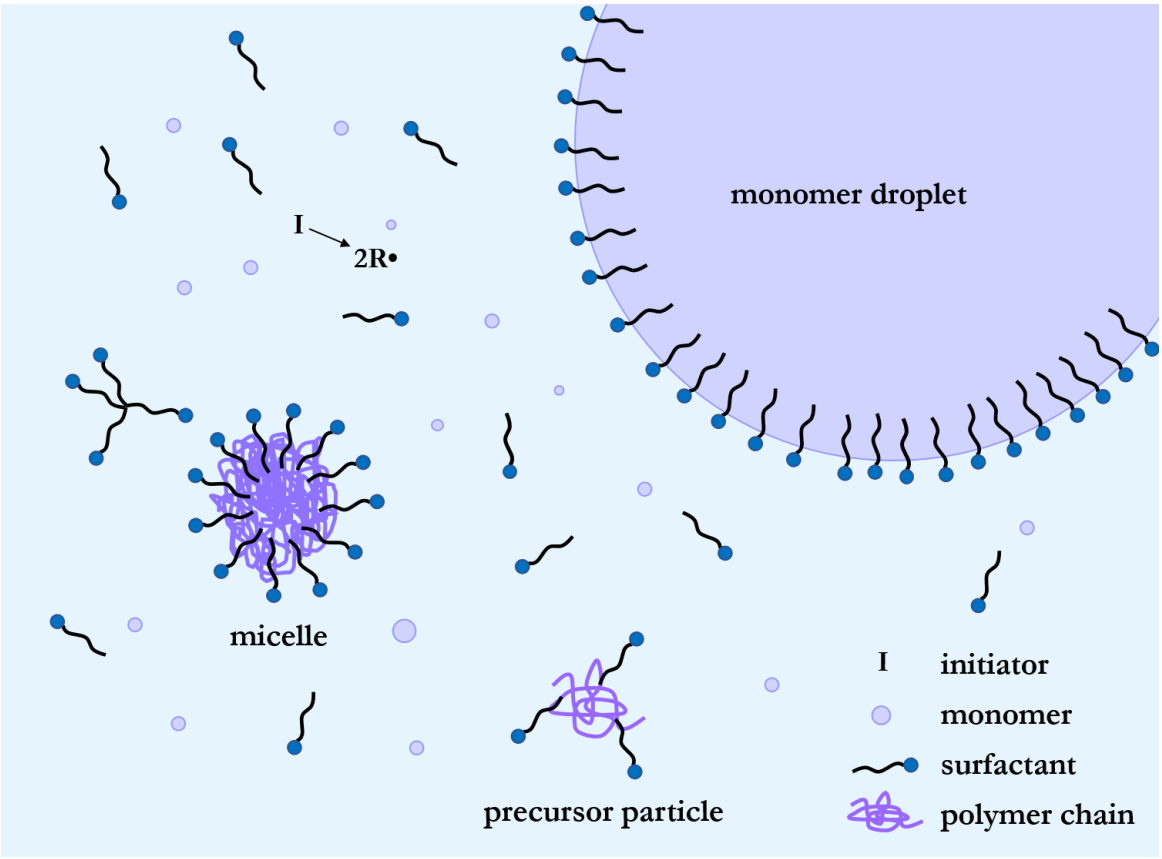

Figure 2.9: Schematic representation of the emulsion polymerization showing the initial state and the different participated components. In the beginning most of the monomer molecules are in very large monomer droplets and just few monomer molecules are dissolved in the water phase, the water-soluble initiator is in the water phase along with surfactant molecules (monomeric dissolved or forming micelles), and the growing polymer chains which serve as precursor particles.

The first qualitative model of emulsion polymerization was proposed by Harkins [93], who divided the process in three distinctive intervals as shown in Figure 2.10. At the beginning, the initiator molecules dissociate to form a radical which reacts with the dissolved monomer molecules in the aqueous phase and start to grow. When the growing polymer chains reach a critical chain length, they tend to either enter a monomer-swollen micelle or form a locus for a precursor particle (see Figure 2.11). At this point Interval I starts, which is the so-called particle nucleation step. In the particle nucleation step, monomer droplets coexist next to surfactant molecules, micelles (if the surfactant concentration is above the critical micelle concentration CMC) and precursor particles. This interval ends directly after all monomer molecules inside a micelle are consumed. Thereafter Interval II or the particle growth stage begins, in which growing polymer particles coexist with monomer droplets. Thereby, the monomer molecules diffuse from the monomer droplets into the growing

particles to ensure that the monomer concentration within the particles is constant. This stage ends once all monomer droplets disappear. Generally, 10 – 60% of the monomer is consumed within this stage. Consequently, Interval III proceeds, where the remaining monomers within the latex particles continue to polymerize and both the monomer concentration and the rate of polymerization decrease toward the end of polymerization.

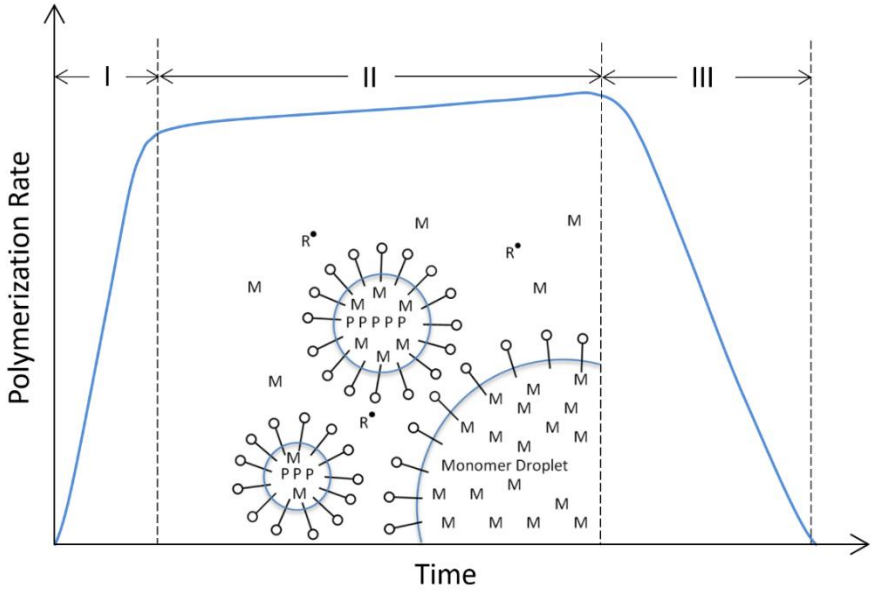

Figure 2.10: Typical rate of polymerization as a function of monomer conversion. The three distinct intervals of emulsion polymerization process are also indicated: (I) particle nucleation, (II) particle growth, and (III) consumption of residual monomer. Taken from [94].

On the bases of Harkins model, the first quantitative model of the processes of particle formation and growth during emulsion polymerization has been established by Smith and Ewart [95]. This is known as the Smith-Ewart theory, which describes the time evolution of the number of particles containing radicals by considering kinetic events that lead to the capture and loss of free radicals with the growing polymer particles. They showed that the rate of polymerization, which proceeds exclusively in the growing particles is given by:

$$R_{\mathrm{p}} = k_{\mathrm{p}}[\mathrm{M_p}]\bar{n}N_{\mathrm{T}} \qquad (10)$$

where k_{p} is the propagation rate constant, $[\mathrm{M_p}]$ the monomer concentration within the mature particles, N_{T} the number of mature particles and $\bar{n}$ the average number of radicals per particle. Furthermore, Smith and Ewart derived an expression to predict the number of produced mature polymer particles using

$$N_T = k\left(p_w/\mu\right)^{0.4}(a_s S_0)^{0.6} \qquad (11)$$

where k is a constant related to the rate of radical entry into micelles and polymer particles, S_0 the initial surfactant concentration, a_s the interfacial area occupied by a surfactant, μ the rate of volume increase of polymer particles and p_w the rate of radical generation.

According to this theory, the number of polymer particles can be increased and the particle size can be decreased (among other things) by increasing the surfactant concentration while keeping a constant rate of radical generation.

For the particle nucleation step (Interval I) there are three proposed mechanisms (see Figure 2.11): The first one is called **(1)** micelle nucleation. It suggests that a waterborne free radical, with or without reacting with a monomer dissolved in the water phase, enters a monomer-swollen micelle and continues the propagation therein. In order to have a significant number of monomer-swollen micelles the surfactant concentration must be above its critical micelle concentration (CMC). The second proposed mechanism is **(2)** homogeneous nucleation. Here a waterborne free radical reacts and propagates with the monomers dissolved in the aqueous phase until it reaches a critical chain length ($RM_c^{\bullet}$) and becomes insoluble in water. Then the hydrophobic chain coils up and forms a particle nucleus in the aqueous phase. The formation of stable particles results from the flocculation of relatively unstable particle nuclei/chains followed by the adsorption of surfactant molecules on the particle surface. This mechanism is suggested to be predominant at surfactant concentrations below the CMC. The third and less probable mechanism is **(3)** droplet nucleation. Where a free radical grows in the aqueous phase enters a monomer droplet (also called a monomer reservoir) and propagate therein. Generally, molecules the droplet nucleation is unlikely to happen in presence of surfactant, because the monomer droplets exhibit an extremely small oil-water interfacial area compared to the interfacial area of micelles.

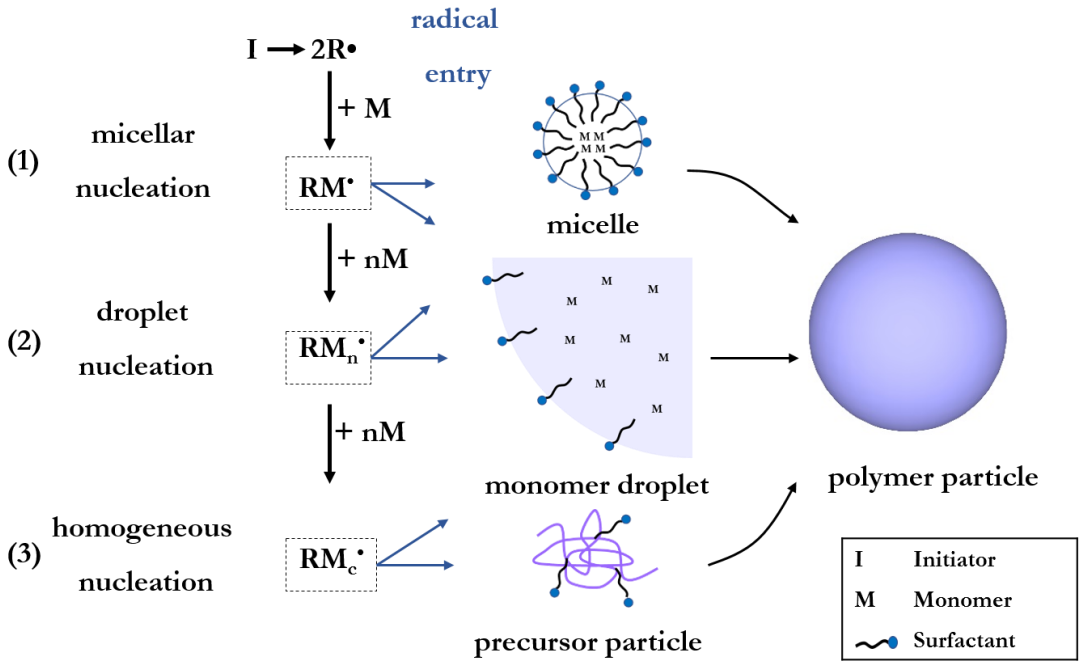

Figure 2.11: The three proposed particle formation mechanisms in a typical emulsion polymerization: (1) Micellar nucleation: the polymerization proceeds in a monomer-swollen micelle. (2) Droplet nucleation: a free radical enters a monomer droplet and the polymerization proceed therein. (3) Homogeneous nucleation: a free radical growing chain exceeds its solubility limit and precipitates to form a precursor particle. Redrawn from [91]

2.3. Porous Polystyrene via NF-CID Method

The goal of this part of the thesis at hand is to produce porous polystyrene with $50 < d_{pore}/nm < 250$ with open-cellular morphology using the NF-CID method. Therefore, the influence of the template, i.e. polymer particle size and packing structure of the corresponding colloidal crystal, on the porous polymers will be investigated. In addition, the influence of the NF-CID process parameters; temperature, exposure time, pressure and the course of expansion will be also systematically examined.

2.3.1. Synthesis of Nanoparticles and Colloidal Crystals of Polystyrene

For a successful conduction of the NF-CID method the properties of the polymer nanoparticles forming the colloidal crystals, which will be subjected to $scCO_2$ and later on foamed, is of vital importance. From the simple geometric consideration given in equation (8), it can be concluded that the size of the nanoparticles will have a significant effect on the pore size of the porous polymers. Aiming for pore size $50 < d_{pore}/nm < 250$, the particle diameter should be considerable small. Another particle property, which might have an influence on the morphology of the porous polymer is the polydispersity of the particles. Therefore, in order to study the influence of the properties of the nanoparticles on the pore size and morphology of the porous polymers obtained by NF-CID method, PS nanoparticles were synthesized via emulsion polymerization using sodium dodecyl sulfate (SDS) as surfactant to stabilize the emulsion (more information about the procedure can be found in the appendix). To adjust the properties of the polymer particles, a set of emulsion polymerizations was performed at 80 °C, where the surfactant concentration [SDS] was varied between 0 mM and 26.2 mM, while all other polymerization conditions were kept constant. After each polymerization the dispersion was characterized by dynamic light scattering (DLS). The measured hydrodynamic diameters (d_H) at 90° were plotted against the concentration of SDS as shown in Figure 2.12 (left, ▲). The figure shows that the hydrodynamic diameter decreases strongly from $d_H = 432 \pm 2$ nm to 78 ± 2 nm, when [SDS] is increased from 0 to 6.5 mM. Increasing [SDS] further the hydrodynamic diameter reduces considerably less and stays almost constant at $d_H = 50 \pm 2$ nm for [SDS] ≥ 9.8 mM. Furthermore, the diameter ($d_{particle}$) and polydispersity (*PDI*) of the particle were characterized, by examining the assembled colloidal crystals obtained after drying the

dispersion at T = 20 °C using scanning electron microscopy (SEM). Analyzing the SEM images (shown in Figure 2.13 and 2.15) using the image processing program *ImageJ*, the same trend was observed for the physical particle diameter $d_{particle}$ as shown in Figure 2.12 (left, ●). As expected, the hydrodynamic diameter which includes the hydration shell is $<\Delta d> \approx 10$ nm larger than the physical diameter of the dried nanoparticles. The decrease in the particle diameter by increasing [SDS] is related to the availability of more surfactant molecules, which can form a larger interfacial area between water and monomer/or polymer.

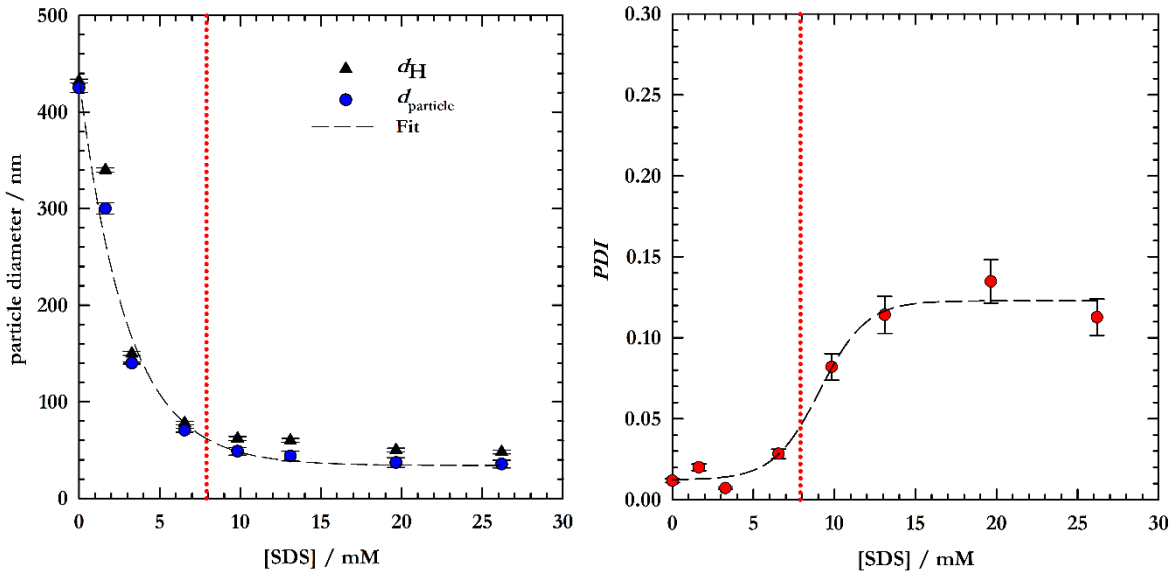

Figure 2.12: (left) Plot of the particle diameter of PS nanoparticles synthesized by emulsion polymerization at T = 80 °C (d_H ▲ is the hydrodynamic diameter of the PS nanoparticles in a diluted aqueous solution, while $d_{particle}$ ● is the physical particle diameter of the dried PS nanoparticles) as a function of the sodium dodecyl sulfate concentration [SDS]. (right) The polydispersity index *PDI* (calculated from SEM images) of the synthesized PS nanoparticles as a function of [SDS]. Both d_H and $d_{particle}$ decrease by increasing [SDS] while *PDI* increases. The red dotted lines in both plots indicate the critical micelle concentration CMC of SDS in the water-styrene system. [96]

Taking a closer look at the SEM images of the assembled colloidal crystals of the synthesized PS nanoparticles (Figure 2.13 and 2.15), it is obvious that they can be classified into two categories with regards to their polydispersity. At [SDS] ≤ 6.5 mM colloidal crystals of monodisperse nanoparticles were found, whereas for [SDS] > 6.5 mM colloidal crystals of polydisperse nanoparticles were obtained. The determination of the *PDI* from the SEM images shows that the *PDI* increases from 0.01 at [SDS] = 0 mM to *PDI* = 0.11 at [SDS] = 26.2 mM as shown in Figure (2.12, right).

The transition from monodisperse to polydisperse particles with increasing [SDS] might be explainable by considering the polymerization nucleation mechanism (see section 2.2.2). At [SDS] lower than the CMC, the homogenous nucleation of polymer chains takes mainly place, while at [SDS] above the CMC, the micellar nucleation is more favored. Looking at the *PDI* as a function of [SDS] (Figure 2.12, right), one sees that the polydispersity increases at [SDS] > 6.5 mM and reaches a plateau at [SDS] around 11 mM. The CMC of SDS in pure water, however, was reported to be 13.1 mM at 80 °C [97]. To study whether the CMC of SDS in the water-styrene mixture is lower than the CMC of SDS in pure water, the interfacial tension of the water-styrene mixture was measured as a function of [SDS] at the polymerization temperature of T = 80 °C by K. Abitaev, she showed that the CMC of SDS in water-styrene mixture is 7.9 ± 0.5 mM, which is indeed in the range, in which the *PDI* of the synthesized PS nanoparticle increases the most. This result indicates that the systematic variation in the particle polydispersity is indeed linked to the different particle formation mechanism during the emulsion polymerization process

In Figure 2.13 SEM images of colloidal crystals consisting of monodisperse PS nanoparticles synthesized at [SDS] ≤ 6.5 mM are shown. As discussed before, the physical diameter d_{particle} of the PS nanoparticles decreases from 425 ± 5 nm to 70 ± 2 nm by increasing [SDS] from 0 to 6.5 mM. As can be seen the colloidal crystals formed by these nanoparticles are highly ordered in a hexagonal arrangement exhibiting both macro- and micro-structural defects, i.e. vacancies, dislocations, line defects, and cracks as shown in Figure 2.14. These packing defects are expected to be unfavorable for the NF-CID method. Since after the addition of CO_2 the foaming of the large vacancies, which are much larger than the voids between the particles will most probably lead to the formation of porous polymers with large pores.

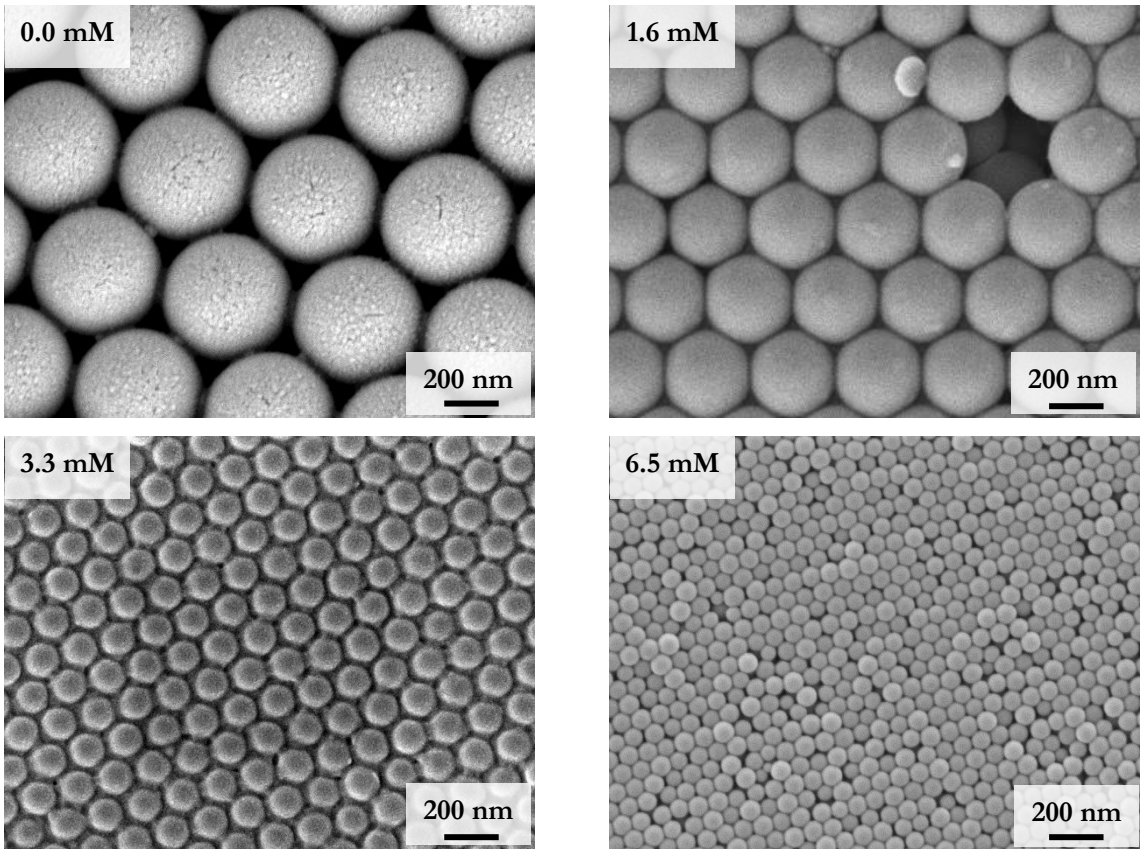

Figure 2.13: SEM images of colloidal crystals of monodisperse PS nanoparticles synthesized by emulsion polymerization using different surfactant concentrations [SDS] = 0.0, 1.6, 3.3 to 6.5 mM, with physical particle diameters of $d_{particle}$ = 425 ± 5, 300 ± 6, 140 ± 1 and 70 ± 2 nm, respectively. In this range of [SDS] the assembled colloidal crystals are highly ordered in a hexagonal arrangement exhabiting packing defects. From [96]

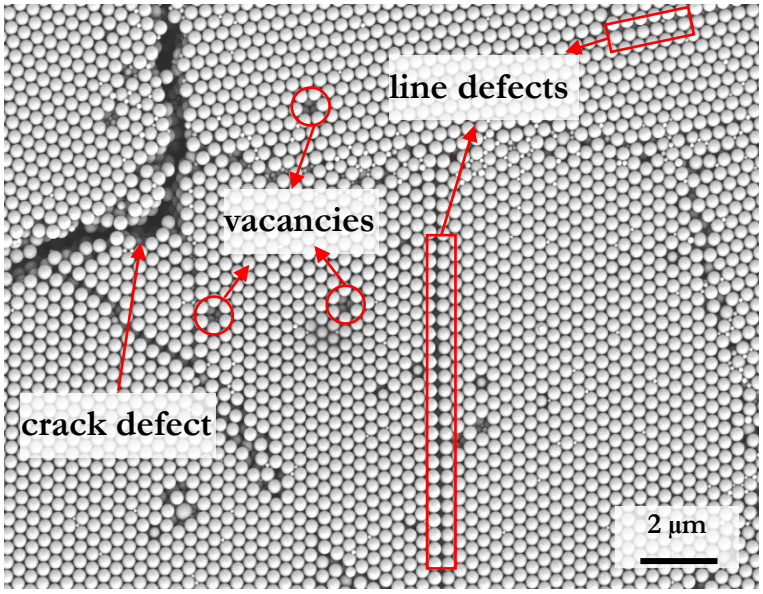

Figure 2.14: SEM image of a colloidal crystal of monodisperse PS nanoparicles (synthesized at [SDS] = 0 mM) showing several types of defects. Beside line defects and crack defects, some vacancies can be observed.

On the contrary, Figure 2.15 shows that, colloidal crystals formed by PS nanoparticles with PDI > 0.08 (synthesized at [SDS] above the CMC) are much denser packed but less ordered compared to the colloidal crystals formed by the monodisperse particles (Figure 2.13). Using [SDS] = 9.8 mM - 26.2 mM PS nanoparticles with $d_{particle}$ between 48 ± 4 nm and 34 ±4 nm were obtained. At [SDS] = 9.8 mM, one sees that the colloidal crystal consists both an ordered hexagonal layer structure and an unordered densely packed structure with less structural defects. Instead these defects are filled by the smaller particles leading to the formation of densely packed colloidal crystals at the expense of the ordered arrangement.

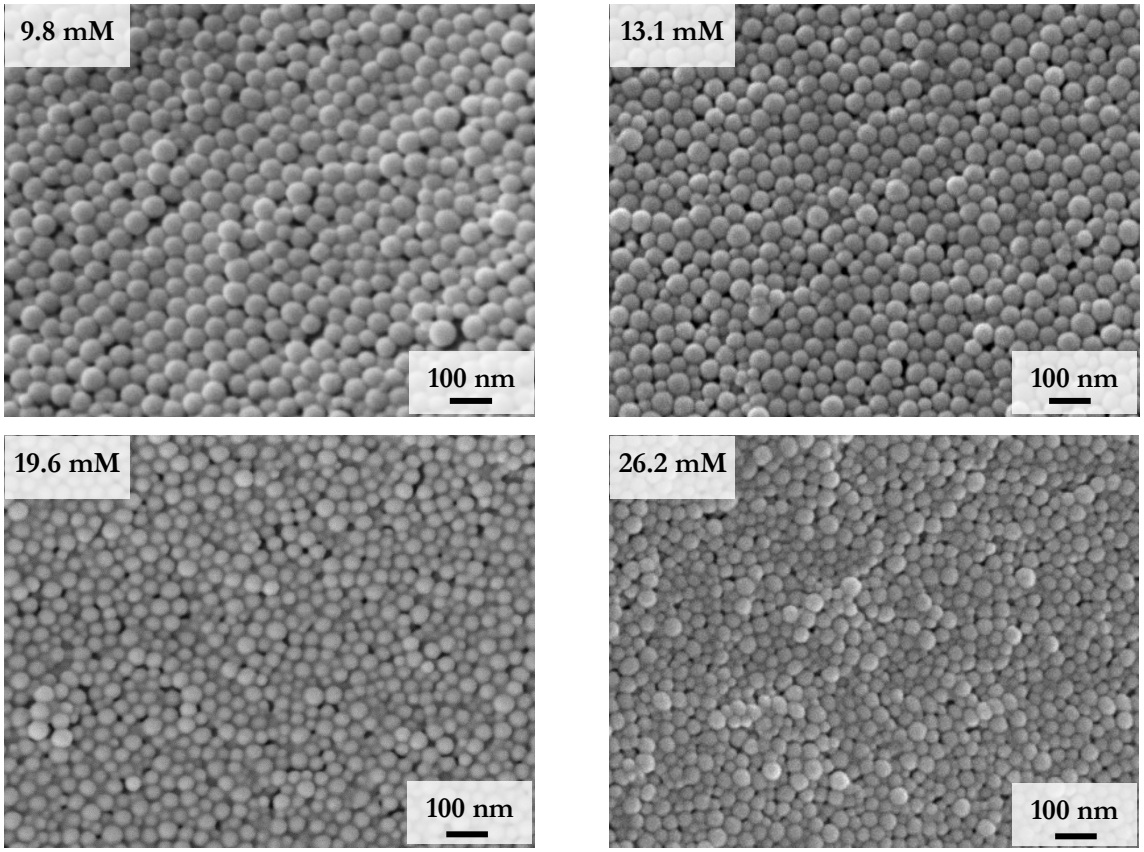

Figure 2.15: SEM images of closely packed colloidal crystals of polydisperse PS nanoparticles synthesized via emulsion polymerization using different surfactant concentrations [SDS] = 9.8, 13.1, 19.6 and 26.2 mM, with physical particle diameters $d_{particle}$ = 48 ± 4, 44 ± 5, 36 ± 5 and 34 ± 4 nm, respectively. In this range of [SDS] the colloidal crystals lose the ordered arrangement while a densely packed arrangement is formed. From [96]

Another important parameter which might influence the pore size and the morphology of the porous polymers, obtained following the NF-CID method, is the average molecular weight of the synthesized polymer, which determines the glass transition temperature of the material. Therefore, the average molecular weight of the different polymer particles was characterized by means of gel permeation chromatography (GPC). The results of the GPC measurement are listed in Table 2.1 and plotted in Figure 2.16. The results reveal that the

number average molecular weight $\overline{M}_n$ increases sharply form 5.9 kg.mol^{-1} to 15.4 kg.mol^{-1} between [SDS] = 6.5 mM and 9.8 mM, i.e. close to the CMC of SDS in water-styrene mixture. This finding indicates that the polymerization mechanism changes from homogeneous to micellar nucleation. In addition, all synthesized polymers have a broad molecular weight distribution (PDI_{Mw}), which is characteristic for free radical polymerization.

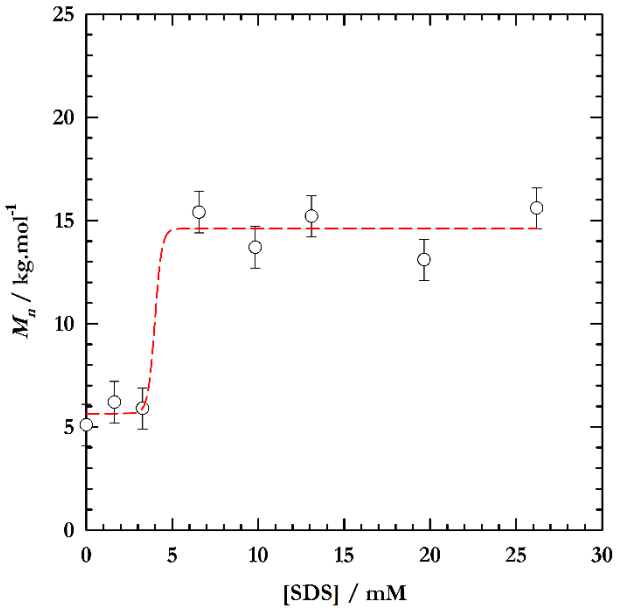

Figure 2.16: Plot of the average number molecular weight of the syntheized PS particle as a function of the sodium dodecyl sulfate concentration [SDS]. The curve exhibits a sharp increase in the $\overline{M}_n$ form 5.9 kg.mol^{-1} to 15.4 kg.mol^{-1} between [SDS] = 6.5 mM and 9.8 mM, which is close to the CMC. This indicates the particle nucleation mechanism of the polymer chains changes form homogeneous to micellar nucleation.

The glass transition temperature T_g, which is the most NF-CID-relevant physical property of the synthesized PS nanoparticles was determined using differential scanning calorimetry (DSC). The T_g values listed in Table 2.1 show that the T_g values follow the trend in average number molecular weight. For the PS nanoparticles synthesized at low [SDS] a glass transition temperature T_g of 74 ± 2 °C is found, while for the PS nanoparticles synthesized at [SDS] ≥ 6.5 mM T_g is located at 92 ± 2 °C.

Table 2.1: Overview of the physical particle diameter $d_{particle}$, number average molecular weight $\overline{M}_n$, molecular weight polydispersity index PDI_{Mw} and the measured glass transition temperature T_g of the synthesized PS nanoparticles at different [SDS]. [96]

[SDS] / mM	$d_{particle}$ / nm	$\overline{M}_n$ / kg.mol^{-1}	PDI_{Mw}	T_g / °C
0.0	425 ± 5	5.1	11.2	72 ± 2
1.6	300 ± 6	6.2	6.5	76 ± 2
3.3	140 ± 1	5.9	9.1	75 ± 2
6.5	70 ± 2	15.4	2.8	93 ± 2
9.8	48 ± 4	13.7	3.7	95 ± 2
13.1	44 ± 5	15.2	3.5	91 ± 2
19.6	37 ± 5	13.1	4.8	88 ± 2
26.2	34 ± 4	15.6	6.5	94 ± 2

2.3.2. Effect of the Polymer Nanoparticles

After the synthesis and characterization of the assembled colloidal crystals of the PS dispersions, the effect of the particle size and polydispersity of the PS nanoparticles on the NF-CID method, with special focus on the pore size and the morphology of the porous polymers, was investigated.

Firstly, a series of experiments was performed on colloidal crystals formed by PS nanoparticles of different size keeping the other parameters of NF-CID constant. Following the NF-CID method (shown in Figure 2.6), the high-pressure cell containing the respective colloidal crystal was filled with CO_2 at room temperature and a pressure of 250 bar. Accordingly, the voids between the particles were filled with CO_2. As a result of the small size of the nanoparticles and the huge surface of the colloidal crystal, the polymer nanoparticles saturate with CO_2 on the time scale of 30 s [83]. Due to the saturation, the glass transition temperature T_g of the polymer reduces considerably. Adjusting the temperature to 55 °C (above the reduced glass transition T_g^* of the matrix), the polymer particles lose their spherical shape and form a connected polymer matrix. Consequently, the so-called "continuity inversion" (Figure 2.6, step 4) takes place, in which the octahedral and tetrahedral voids (ideal packing) filled with $scCO_2$ transform into spherical nanodroplets in the highly viscous polymer matrix to minimize the interfacial energy. After an exposure time (t_{exp}) of 15 minutes, the pressure was released at T = 55 °C within 5-10 s. Due to the significantly lower solubility of CO_2 in the polymer at ambient pressure the dissolved CO_2 molecules diffuse out of the polymer, which causes the solidification of the polymer matrix. If no aging process occurred, each CO_2 droplet transforms into a pore.

As we found that both the nanoparticle diameter and the glass transition temperature vary with [SDS], the influence of the particle diameter on the pore size of the porous polymers will be discussed as following: the first part considers the PS nanoparticles with $T_g = 74 \pm 2$ °C (synthesized at [SDS] < 6.5 mM), while the second part considers those with $T_g = 92 \pm 4$ °C (synthesized at [SDS] ≥ 6.5 mM).

Foaming the colloidal crystals with T_g = 72 ± 2 °C

While, porous polymers were successfully obtained by foaming colloidal crystals of monodisperse PS nanoparticles with $d_{particle}$ = 300 nm and 140 nm, crystals of larger particles ($d_{particle}$ = 425 nm, synthesized at [SDS] = 0.0 mM) did not foam but burst upon expansion. In Figure 2.17 the SEM images of the resulting porous polymers are shown.

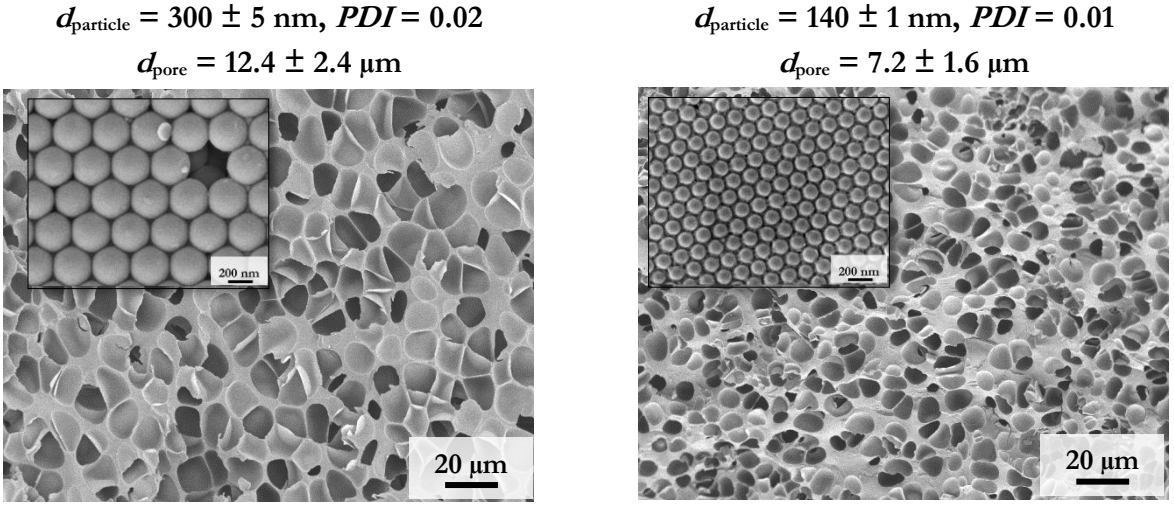

Figure 2.17: SEM images of the PS porous polymers obtained via the NF-CID method using $scCO_2$ at T = 55 °C and p = 250 bar. After t_{exp} = 15 min the pressure was rapidly released at 55 °C. The PS porous polymers are based on colloidal crystals of PS monodisperse nanoparticles (left) $d_{particle}$ = 300 nm with *PDI* of 0.02 and (right) $d_{particle}$ = 140 nm with *PDI* of 0.01. The insets represent the SEM image of the corresponding colloidal crystal. [96]

Foaming the colloidal crystal of monodisperse PS nanoparticles with $d_{particle}$ = 300 ± 5 nm, a porous polymer with d_{pore}= 12.4 ± 2.4 µm was obtained, while the colloidal crystal of monodisperse PS nanoparticles with $d_{particle}$ = 140 ± 1 nm delivered a porous polystyrene with d_{pore}= 7.2 ± 1.6 µm. These results clearly show that the pore size of the porous polymers is correlated to the particle diameter of the polymer nanoparticles. However, calculating the pore size of the porous polymer assuming an ideal inversion and expansion processes without aging phenomena a pore size d_{pred} = 1.7 µm and 0.8 µm, respectively, are predicted using equation (8). Obviously, this discrepancy between the obtained and the predicted pore sizes can be attributed to aging phenomena (Ostwald ripening and coalescence), which may have occurred during both the continuity inversion and the expansion step. The presence of structure defects in both colloidal crystals (see Figure 2.14) might ease the aging mechanism of the $scCO_2$ droplets in the polymer melt via Ostwald ripening. Vacancy defects, for instance, lead to the formation of larger spherical $scCO_2$ droplets along with the small spherical droplets, which originate from the voids between

the well-packed particles. Moreover, aging via coagulation followed by coalescence is possible when the viscosity of the polymer melt becomes considerably low due to high amount of CO_2 dissolved at T = 55 °C and p = 250 bar.

Foaming colloidal crystals with T_g = 92 ± 4 °C

Foaming the colloidal crystals of PS nanoparticles with T_g values = 92 ± 4 °C led to porous polymers with various morphologies. On the one hand, foaming a colloidal crystal of monodisperse PS nanoparticle with $d_{particle}$ = 70 nm a porous polymer with a pore size of d_{pore} = 8.4 ± 2.8 μm was obtained as shown in Figure 2.18, top. Again, the obtained pore size is considerably larger than the predicted value d_{pred} = 0.4 μm, which is as before can be explained by pronounced aging processes, i.e. mainly Ostwald ripening caused by the packing defects in the colloidal crystal (See SEM image of the colloidal crystal shown in the inset of Figure 2.18, top).

On the other hand, foaming densely packed colloidal crystals of relatively polydisperse (PDI > 0.08) PS nanoparticles with d_{part} = 48 ± 4 nm and d_{part} = 44 ± 5 nm delivers porous polymers (Figure 2.18, bottom) with a bimodal morphology, where large pores d_{pore} > 10 μm coexist with small pores d_{pore} = 1.80 ± 0.40 μm and 3.40 ± 0.80 μm, respectively. The bimodal morphology in these two samples can be attributed to formation of densely packed colloidal crystals containing some packing defects, which are expected to cause the formation of the large pores d_{pore} > 10 μm. Note that the predicted pore size is equal to d_{pred} = 0.27 μm and d_{pred} = 0.24 μm, respectively.

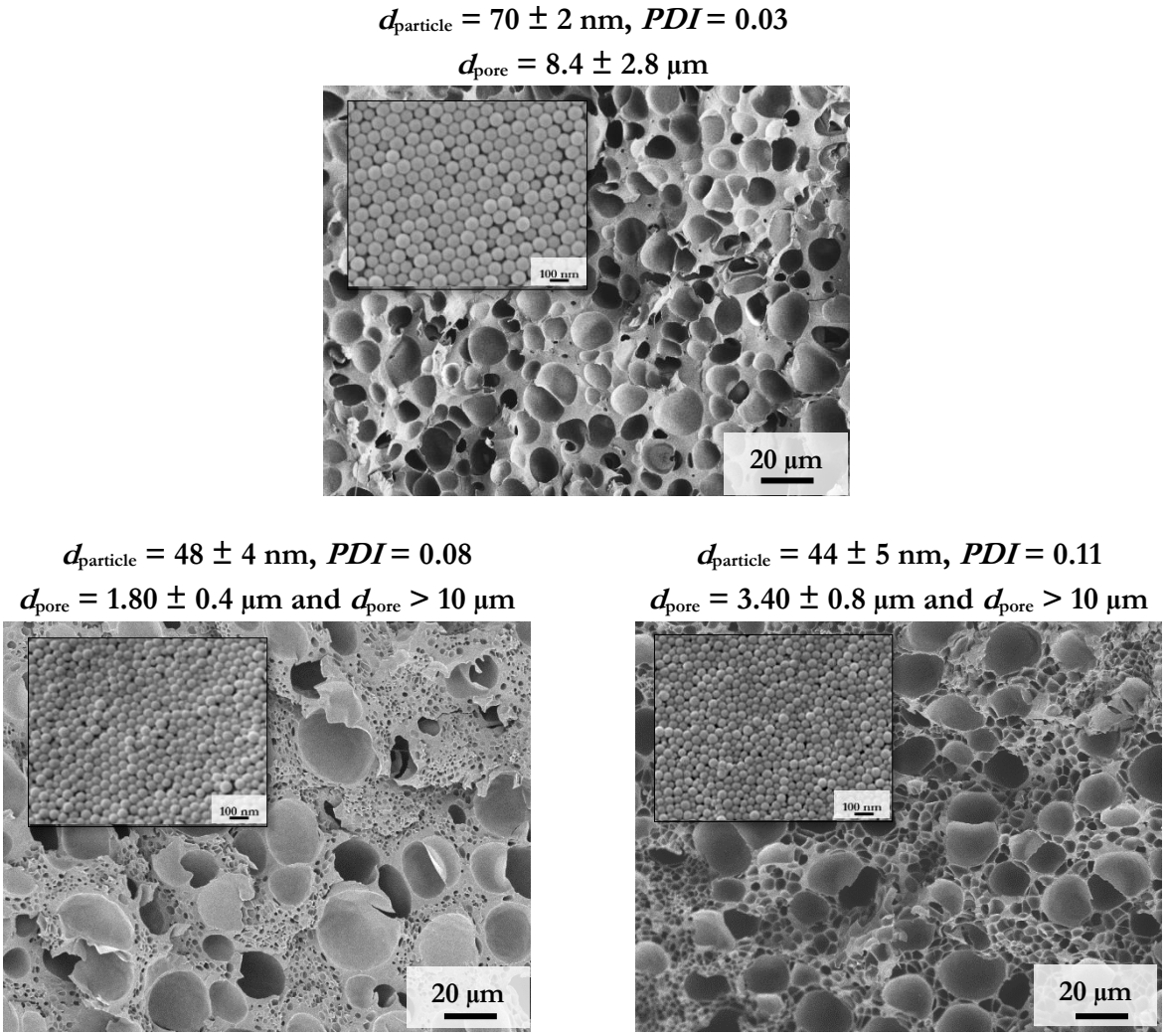

Figure 2.18: SEM images of the PS porous polymers obtained via the NF-CID method using $scCO_2$ at T = 55 °C and p = 250 bar. After an exposure time of 15 min the pressure was rapidly released at T = 55 °C. The PS porous polymers are based on a colloidal crystal of (top) monodisperse PS nanoparticles $d_{particle}$ = 70 nm with *PDI* of 0.03, (bottom, left) relatively polydisperse PS nanoparticles $d_{particle}$ = 48 nm with *PDI* of 0.08, (bottom, right) and relatively polydisperse PS nanoparticles $d_{particle}$ = 44 nm with *PDI* of 0.11. The insets on each image represent the SEM image of the corresponding colloidal crystal. [96]

By foaming the colloidal crystals of PS nanoparticles with $d_{particle}$ < 40 nm and larger polydispersity index (*PDI* > 0.10) a unimodal morphology with small pore size was achieved. For instance, a porous polymer with d_{pore} = 1.60 ± 0.40 µm was obtained foaming a colloidal crystal of nanoparticles with $d_{particle}$ = 36 nm (Figure 2.19, top), whereas, a porous polymer with d_{pore} = 0.90 ± 0.20 µm was found when a colloidal crystal of the PS nanoparticles with $d_{particle}$ = 34 nm is foamed (Figure 2.19, bottom).

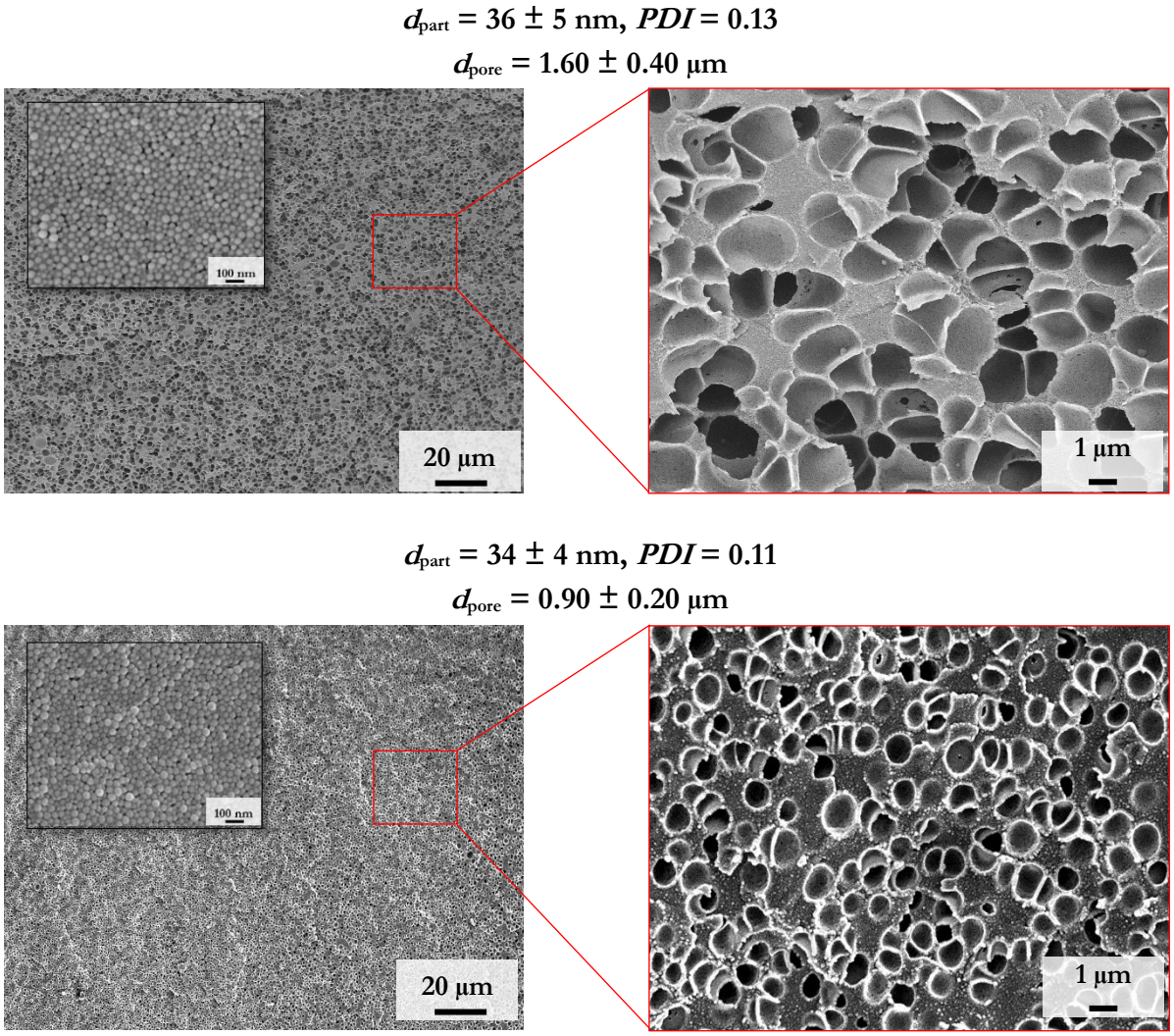

Figure 2.19: SEM images of the PS porous polymers obtained via the NF-CID method using $scCO_2$ at T = 55 °C and p = 250 bar. After an exposure time of 15 min the pressure was rapidly released at T = 55 °C. The PS porous polymers are based on a colloidal crystal of PS nanoparticles (top) $d_{particle}$ = 36 ± 5 nm with *PDI* of 0.13 and (bottom) $d_{particle}$ = 34 ± 4 nm with *PDI* of 0.11. The insets represent the SEM image of the corresponding colloidal crystal. [96]

To sum up, the investigations so far showed that the NF-CID method can be used to produce porous polystyrene exhibiting closed-cellular morphology and pore sizes larger than 0.9 µm, which is a factor of 5-20 larger than the theoretically predicted size. Depending on the PS particle diameter and the *PDI*, the method suffers to a different degree from aging phenomena. On the one hand, porous polymers of the rather monodisperse nanoparticles (*PDI* < 0.03) suffer strongly from packing defects in the colloidal crystal, which led to pore sizes d_{pore} > 7.2 µm. On the other hand, foaming colloidal crystals of the rather polydisperse nanoparticles (*PDI* > 0.08) led to porous polymers with pore sizes d_{pore} < 3.4 µm. Thereby, the porous polymers with the smallest pore size (d_{pore} = 1.6 and 0.9 µm) and a homogeneous morphology were obtained from colloidal crystals with

$d_{particle}$ of 36 nm and 34 nm, respectively. The fact that colloidal crystals with $d_{particle}$ = 48 nm and 44 nm led to porous polymers with a bimodal morphology might indicate that these colloidal crystals are not (efficiently) densely packed.

Therefore, the packing efficiency of the colloidal crystals with $PDI \geq 0.08$ was studied by the Brunauer-Emmett-Teller (BET) method, which measures the total pore volume of pores that are smaller than 50 nm. Thus, the performed measurements detected the voids between the nanoparticles, while the volume of the defects, which are larger than 50 nm cannot be measured. The pore volume per gram of the studied samples is listed in Table 2.2. Therewith, the packing efficiency/density of the colloidal crystals was estimated. The results show that with a packing efficiency of 78 %, homogenous unimodal porous polymers were produced, while smaller packing efficiencies led to bimodal morphology.

Table 2.2: Overview of the pore volume per gram (V_{pore}) measured by BET and the estimated packing efficiency for colloidal crystals with $PDI \geq 0.08$.

[SDS]/mM	$d_{particle}$/nm	morpology	V_{pore}/cm^3.g^{-1}	packing efficiency Ø
9.8	48 ± 4	bimodal	0.33	75 %
13.1	44 ± 5	bimodal	0.32	75 %
(13.1)*	48 ± 6	unimodal	0.27	78 %
19.6	36 ± 5	unimodal	0.27	78 %
26.2	34 ± 4	unimodal	0.18	84 %

* PS nanoaprticles were synthesized at 80 °C under certain conditions to increase the polydispersity and thus the packing efficiency of the colloidal crystals. The procedure is described in the appendix.

In order to prove this correlation two colloidal crystals of PS nanoparticles with a similar particle diameter $d_{particle}$ of 48 nm but two different *PDI* (0.08 and 0.12) were foamed using the NF-CID method. BET measurements provided an increase of the packing efficiency from 75 % to 78 % with increasing *PDI*. The SEM images of the produced porous polymers are shown in Figure 2.20. The results prove the correlation between the packing density and the morphology of the obtained porous polymer. As can be seen, foaming the colloidal crystal with Ø = 78 %, a porous polymer with a homogenous unimodal morphology and a pore size d_{pore} = 0.83 ± 0.20 µm was obtained, while foaming the colloidal crystal with Ø = 75 % delivered a porous polymer with bimodal morphology, i.e. large pores > 10 µm

and small pores $d_{pore} \approx 1$ µm. Note that both colloidal crystals are assembled from PS nanoparticle having identical $d_{particle}$ and T_g.

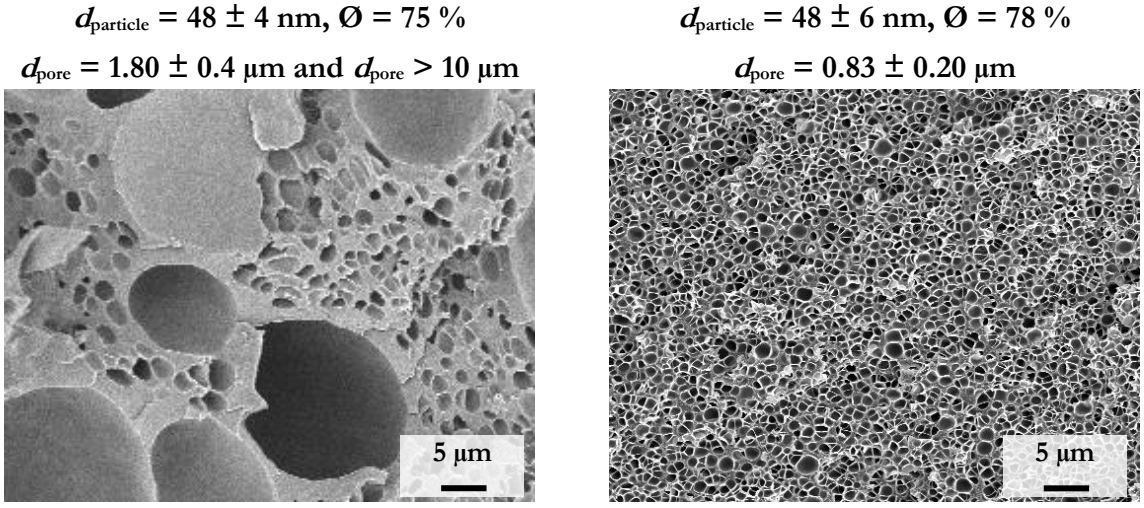

Figure 2.20: SEM images of the PS porous polymers obtained via the NF-CID method using $scCO_2$ at T = 55 °C and p = 250 bar. After an exposure time of 15 min the pressure was rapidly released at T = 55 °C. The PS porous polymers are based on a colloidal crystal of PS nanoparticles: (left) $d_{particle}$ = 48 ± 4 nm with a packing efficiency Ø of 75 % and (bottom) $d_{particle}$ = 48 ± 6 nm with a packing efficiency Ø of 78 %.

2.3.3. Effect of NF-CID Foaming Parameters

Based on the results of section (2.3.2) colloidal crystals of relatively polydisperse PS nanoparticles with $d_{particle}$ = 48 ± 6 nm, *PDI* = 0.12 and a packing efficiency of 78% were chosen to study the effect of NF-CID parameters, namely temperature and exposure time, on the course of NF-CID method. Figure 2.21 shows the SEM images of the colloidal crystal of these PS nanoparticles.

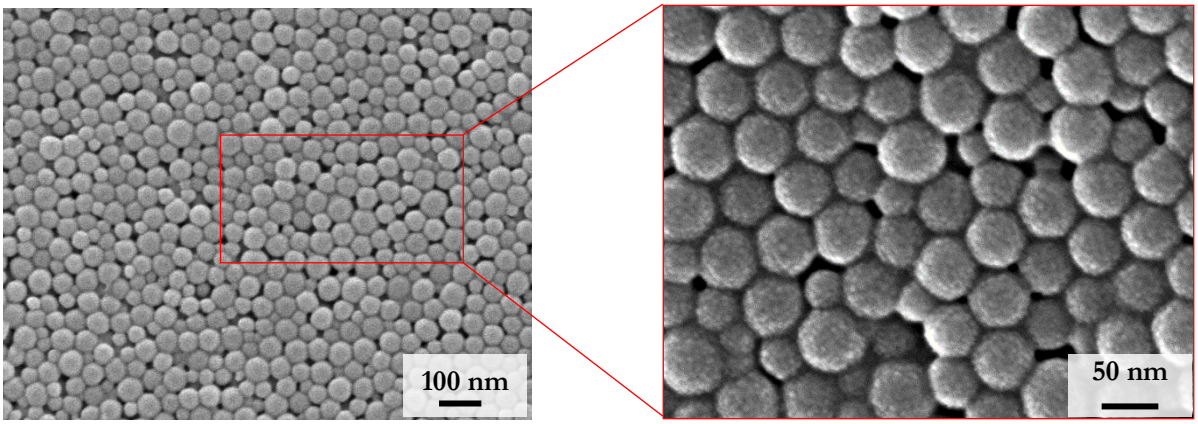

Figure 2.21: SEM image of the closely packed colloidal crystals of PS nanoparticles with $d_{particle}$ = 48 ± 6 nm with a packing efficiency Ø of 78 % obtained via the synthesis of PS nanoparticles by emulsion polymerization followed by isothermal (T = 20 °C) evaporation of the dispersion. Taken from [98]

Effect of temperature on the NF-CID method

Following the NF-CID method the temperature should be adjusted close but slightly above the glass transition temperature T_g^* of the scCO$_2$ saturated PS nanoparticles to obtain a highly viscous matrix. Note that at temperature below T_g^* no foaming of the glassy matrix would be possible, while at too high temperature both Ostwald ripening and coalescence are expected due to the low viscosity of the matrix.

Thus, in order to find the optimal temperature, its influence on the NF-CID method has been studied using colloidal crystals of the relatively polydisperse PS nanoparticles shown in Figure 2.21, adjusting a pressure of p = 250 bar. The exposure time was set again to 15 min, after that the pressure was released by opening the valve rapidly. In Figure 2.22 SEM images of the porous polymers synthesized at five different temperatures (T = 35, 45, 55, 65, and 75 °C) are shown. As can be seen at T = 35 °C, a PS bulk material with almost any pore was obtained, i.e. no foaming has taken place. Instead, even the nanoparticles are still visible. This implies that at 35 °C, the T_g^* of the CO$_2$-loaded PS matrix is not exceeded.

At a temperature of 45 °C, however, nanopores can be observed in the PS matrix which suggest that T_g^* is reached at T = 45 °C. The presence of a highly viscous PS polymer matrix enables the onset of the continuity-inversion from closely packed PS nanoparticles-in-CO_2 to CO_2-nanodroplets in polymer matrix. Analyzing the SEM images, a pore size of d_{pore} = 274 ± 62 nm, a porosity of 34 %, and cell density of 5.3×10^5 cm^{-3} were found. However, the relatively low porosity and low cell density indicate that at T = 45 °C the sample is very close to T_g^* leading to a matrix with very high viscosity. Thus, the continuity inversion was probably not fully completed. Moreover, upon releasing the pressure T_g^* increases, thereby, the matrix instantaneously returns in the glassy state inhibiting the complete foaming of the matrix. Subsequently, the NF-CID method was performed at T = 55 °C. As can be seen in Figure 2.22, a porous polymer with a pore size of d_{pore} = 830 ± 200 nm, a porosity of 49 %, and a cell density of 1.5×10^{12} cm^{-3} was obtained, which implies that at 55 °C the T_g^* of the CO_2-loaded PS particles is exceeded, enabling both the continuity inversion and foaming of the matrix before it solidifies. However, exhibiting a pore size that is a factor 3 lager than the predicted, this suggest that the obtained porous polymer suffers from aging phenomena.

Foaming experiments were also performed at T = 65 °C and T = 75 °C, keeping again the other parameters constant. As can be seen from Figure 2.22, performing the NF-CID method at T = 65 °C led to a PS porous polymer with a larger pore diameter of 1.21 ± 0.28 μm, a porosity of 63 %, and a cell density of 5.3×10^{11} cm^{-3}. The increase of the pore size can be related to the further increasing significance of Ostwald ripening of the CO_2 nanodroplets as well as their coagulation and coalescence which are enhanced at lower viscosities. Interestingly, the foaming experiment performed at a further increased temperature of T = 75 °C led to a bimodal cell morphology with even larger pore sizes of 13 and 4.5 μm. Imaging the porous structure at lower magnification (Figure 2.21 inset SEM image of 75 °C), it becomes obvious that the larger pores are formed preferentially along the grain boundaries of the colloidal crystals.

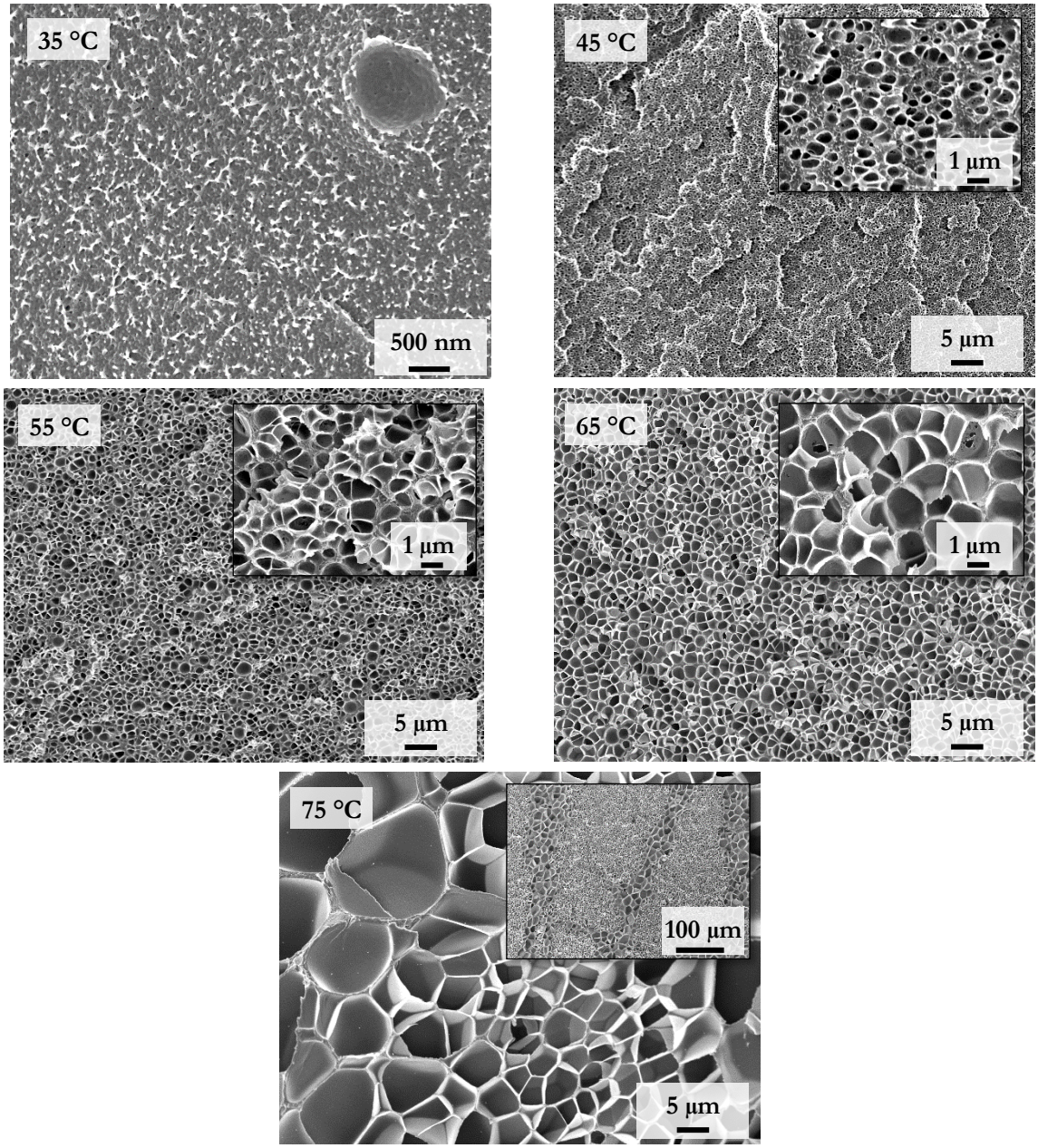

Figure 2.22: SEM images of PS porous polymers obtained via the NF-CID method. Colloidal crystals (Figure 2.21) of PS nanoparticles $d_{particle}$ = 48 ± 6 nm with Ø = 78 % were filled with $scCO_2$ at p = 250 bar and at various temperatures T = 35, 45, 55, 65 as well as 75 °C. After t_{exp} = 15 min the pressure was rapidly released. While no foaming of the colloidal crystals is observed at T = 35 °C, at T = 45 °C pores with a diameter of d_{pore} = 274 ± 62 nm were observed, which agrees with the value predicted by equation (8) d_{pore} = 274 nm. At T = 55 °C porous polymer exhibiting a pore size that is a factor 3 lager than the predicted was obtained.

Summarizing the results of the foaming experiments performed on colloidal crystals with the same PS nanoparticles ($d_{particle}$= 48 ± 6 nm) but at different temperatures while the other parameters were kept constant, it can be concluded that the onset of foaming was obtained at 45 °C. Increasing the temperature by 10 K, the colloidal crystal of PS nanoparticles was evenly foamed. However, the obtained porous polymer suffers already from aging processes.

Effect of exposure time on the NF-CID method

In order to study whether coarsening has taken place at T = 55 °C, the exposure time was increased to 30 min and 60 min while the other parameters of the NF-CID method were kept constant. Figure 2.23 shows the SEM images of the porous polymers obtained from foaming experiments at different exposure times in direct comparison. As can be seen, the size of the pores increases while the number of pores decreases with increasing exposure time, confirming the assumption that coarsening processes were already present at T = 55 °C. Analyzing the SEM images, an increase of the pore size d_{pore} from 830 ± 200 nm to 1700 ± 500 nm to 2900 ± 500 nm was observed by increasing the exposure time from 15 min (top, left) to 30 min (top, right) to 60 min (bottom) respectively. Considering the SEM images taken from the porous polymers with t_{exp} = 30 min and 60 min, it becomes obvious that the plateau borders become thicker with increasing exposure time. This indicates that the most of coarsening is occurring during the continuity-inversion step.

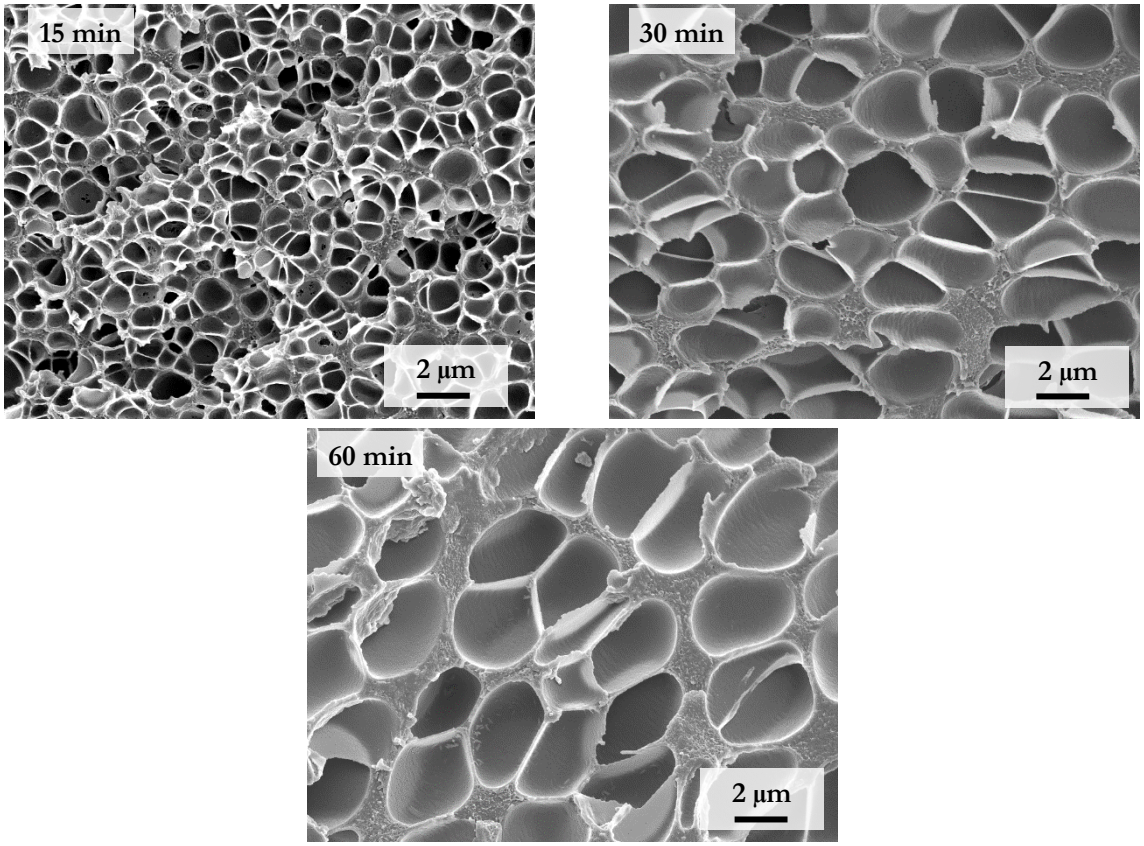

Figure 2.23: SEM images of PS porous polymers obtained via the NF-CID method. Colloidal crystals of PS nanoparticles $d_{particle}$ = 48 ± 6 nm with Ø = 78 % were filled with $scCO_2$ at p = 250 bar and T = 55 °C. After different exposure times the pressure was rapidly released. Increasing the exposure time from t_{exp} = 15 min (top, left) to t_{exp} = 30 min (top, right) and to t_{exp} = 60 min (bottom) led to an increase of the mean pore size d_{pore} from 800 ± 200 nm to 1700 ± 500 nm to 2900 ± 500 nm, respectivley.

2.3.4. Modification of NF-CID Method

Being part of the CRC 1333 "Molecular Heterogeneous Catalysis in Confined Geometries", one main goal of this thesis was the synthesis of porous polymers as supports for heterogeneous molecular catalysis. This means, on the one hand, an open-cellular morphology is needed to allow the access of surrounding fluids containing the different reaction partners. On the other hand, the pore sizes should be smaller than 50 nm. However, so far, all the produced porous polymers following the NF-CID method have a pore size larger than 50 nm and a closed-cellular morphology.

The investigation on the effect of particle size, temperature and exposure time on the morphology and the pore size of the porous polymers revealed that one can control the properties of the obtained porous polymer by these parameters, while the smallest available pore size is defined by the diameter of the PS nanoparticles. In addition, the aging processes which occur during the continuity-inversion step can be controlled by adjusting both the temperature and the exposure time. However, the aging processes occurring during the expansion step are not avoidable as long as the expansion is conducted at a temperature higher than the T_g^* of the polymer saturated with $scCO_2$. Thus, the NF-CID method suffers from the following conceptional problems. On the one hand, a temperature only slightly higher than T_g^* is essential to ensure the full continuity-inversion and to minimize coarsening during the inversion process. On the other hand, temperatures which are too close to T_g^* might inhibit the complete foaming of the sample, which returns quickly into the glassy state during expansion

Therefore, the NF-CID process has been modified conducting the inversion and expansion step at different temperatures. (1) To ensure a full inversion, the continuity-inversion is performed at a temperature above but close T_g^*. (2) To limit the aging processes, the expansion (during depressurization) is performed at low temperatures, i.e. low viscosity. (3) To enhance the expansion an additional heating step is conducted after the depressurization step.

Procedure of the modified NF-CID method

The modified NF-CID method is sketched in Figure 2.24: The steps (1-4) of the original NF-CID method are performed as before (until the continuity-inversion, Figure 2.6). Using PS nanoparticles with $d_{particle}$ = 48 ± 6 nm and Ø = 78 % the continuity inversion was

performed at p = 250 bar, T = 65 °C and an exposure time of t_{exp} = 30 min. The expansion step was then modified as follows: (1) After an exposure time of t_{exp} = 30 min, the sample is cooled down to T = 25 °C, while keeping the pressure at p = 250 bar. At this temperature the polymer matrix is in the glassy state. Due to the temperature decrease, the density of CO_2 increases, i.e. the size of the inclusion decreases slightly. (2) At T = 25 °C the pressure is released. This step has to performed slowly (~10 min) to prevent the glassy matrix from bursting. Being in the glassy state the polymer matrix with the CO_2 inclusion do not expand during this pressure quench. (3) Thereafter, a rapid temperature increase is carried out by transferring the sample quickly to a water bath of T = 65 °C for 10 min leading to an additional expansion, since the solubility of CO_2 in the polymer decreases as a result of the temperature increase. Thus, a porous polymer with open-cellular morphology is obtained.

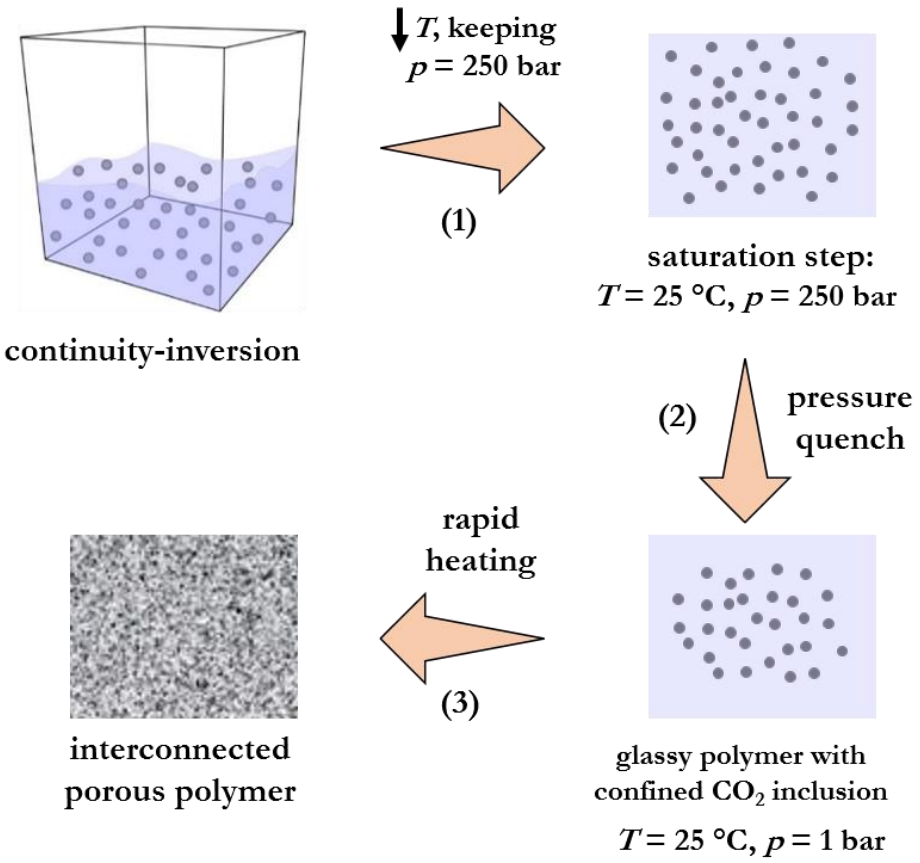

Figure 2.24: Schematic representation of the modified NF-CID method. The steps (1-4) of the conventional NF-CID until the continuity inversion are performed as before, at a temperature and pressure, that ensures the full inversion of the voids between the particles in the colloidal crystal soaked with CO_2 into $scCO_2$ droplets in the polymer matrix. After an exposure time of 30 min, the system is cooled down to T = 25 °C keeping the pressure constant at p = 250 bar. Afterwards, the expansion is performed by releasing the pressure slowly at T = 25 °C. Followed by a rapid heating step leading to an additional expansion. Therewith, an interconnected nanoporous polymer is obtained.

The modified NF-CID method was applied on a colloidal crystal of relatively polydisperse PS nanoparticles with $d_{particle}$ = 48 ± 6 nm, *PDI* = 0.12, and Ø = 78 %. The SEM images of the obtained porous polymer are shown in Figure 2.25. It revealed that a bimodal structure consisting of larger spherical pores which are surrounded by an open-cellular morphology with a pore size of d_{pore} ≈ 50 nm. This kind of porous structure with such a morphology are known as interconnected porous polymers [99]. The observed large pores most probably can be attributed to presence of the structural defects in the colloidal crystal. Moreover, it was found that the porous polymer is surrounded by a dense, nonporous layer, which is because of the desorption of CO_2 from the polymer surface during the pressure release step.

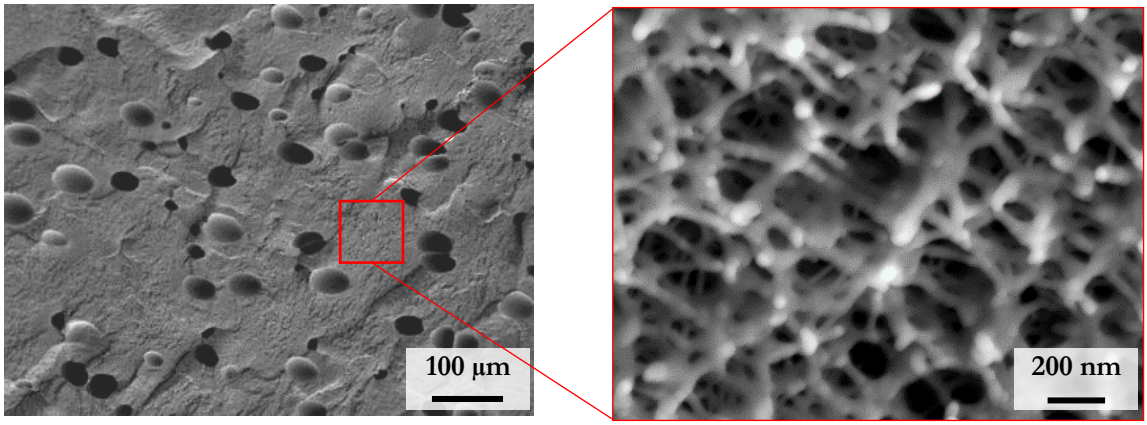

Figure 2.25: SEM-image of the porous polystyrene produced following the modified NF-CID method based on relatively polydisperse PS nanoparticle with $d_{particle}$ = 48 ± 6 nm, *PDI* = 0.12 with Ø = 78 %: Continuity-inversion at T = 65 °C, p = 250 bar. After 30 min the system was cooled down to T = 25 °C keeping the pressure at p = 250 bar. Then the pressure was slowly released at T = 25 °C, followed by a rapid heating step to T = 65 °C for 10 min. (left) At low magnification the SEM image shows the presence of large pores with d_{pore} ≈ 30 µm. (right) A higher magnification showing the nanoporous interconnected structure with d_{pore} ≈ 50 nm.

Colloidal crystals of monodisperse PS nanoparticles were also foamed following the modified NF-CID method to examine the role of the template (colloidal crystals) on method. The investigations were carried out on two colloidal crystals; one formed of PS nanoparticles of $d_{particle}$ = 425 ± 10 nm with *PDI* = 0.01 and the second one of $d_{particle}$ = 70 ± 4 nm with *PDI* = 0.03. Foaming of these less densely packed colloidal crystals of monodisperse PS nanoparticles led to the formation of a nonhomogeneous polymer with some large pores but no nanoporous structure obtained.

2.4. Porous Organic/Inorganic Hybrid Materials

In the previous section I could show that using the modified NF-CID method the synthesis of interconnected porous polymers with a pore size of the order of 50 nm is feasible. However, a potential weakness of utilizing these porous polymers as support materials in catalysis is their instability against harsh organic solvents and high temperatures. In order to overcome this weakness, the formation of a metal oxide layer on the pore wall was envisaged allowing also a further decrease and finetuning of the pore diameter.

2.4.1. Background

Organic/inorganic hybrid materials with their complex features have numerous applications in fields like energy, microelectronics, and optics [100]. With respect to their synthesis at mild condition one can learn from living nature e.g. nacre (see Figure 2.26), which produces minerals at ambient conditions through biomineralization [101]. Hereby, the formation of the inorganic part of the bio/inorganic composite is usually controlled by biotemplates in localized volumes as shown in the case of the formation of nacre in Figure 2.27. Within these confinements, the organisms govern the mineralization process and hence the morphology and orientation of the minerals through control of the precursor ions and mineral phases [102].

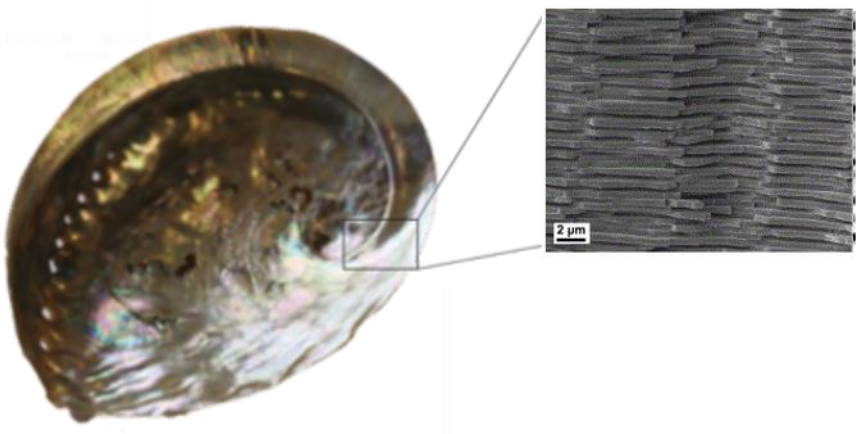

Figure 2.26: (left) Image of the inner nacreous layer of abalone shell. (right) SEM image of a fracture surface in nacre showing 0.5 µm tablets of aragonite ($CaCO_3$) held together by a 10-50 nm layer of an organic biopolymer. SEM image is taken from [103].

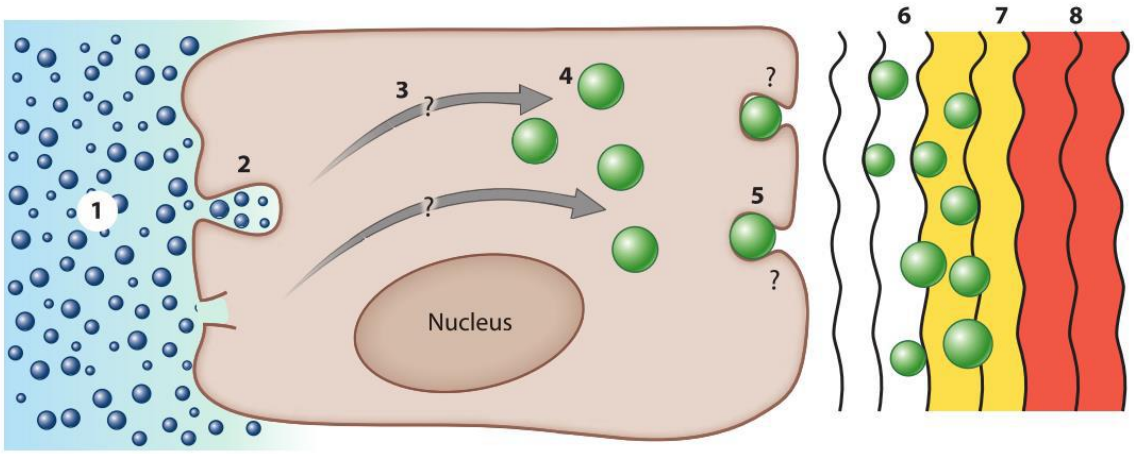

Figure 2.27: Abalone shell - Nacre scheme of generalized crystallization pathway in biologically controlled extracellular biomineralization: (1) The medium from which the ions are captured (sea water or body fluids). (2) The endocytosis of fluid droplets. (3) Transport within the cell to specialized vesicles. (4) Specialized vesicles in which the formation of disordered minerals occurs. (5) The exocytosis of mineral-bearing vesicles into the extracellular space. (6-8) The final formation of the mature mineralized tissue. Taken from [104].

Inspired by biomineralization, organic/inorganic mesoporous hybrid materials can be synthesized with more technologically relevant materials like functional oxides making use of the mild reaction conditions of the chemical bath deposition (CBD) method. CBD is a method for the deposition of a thin solid film of metal oxides in solution using a controlled chemical reaction to manipulate the deposition rate [105]. The precipitation occurs from thermodynamically instable supersaturated solutions. There are two suggested mechanisms leading to the formation of a solid phase on a templated substrate as sketched in Figure 2.28. By the heterogeneous precipitation (nucleation), the ions coordinate/attach at the template surface and start to form the thin film which grows from the substrate. This mechanism is called "ion-by-ion" formation. By the homogeneous precipitation (nucleation), the particles are firstly nucleated in the solution and subsequently arranged on the template surface forming a thin inorganic film. This mechanism is called "cluster-by-cluster" formation. Note that a general introduction into nucleation mechanism is given in section (2.1.2).

In more details, the samples are placed in a liquid precursor solution of the corresponding oxide and mineralized at a temperature below 100 °C. Importantly, the control over the mineralization process enables selective deposition of inorganic particles on organic

templates with adjustable features (size, crystallinity, and polarity), which can help to tune the properties of the corresponding organic/inorganic materials.

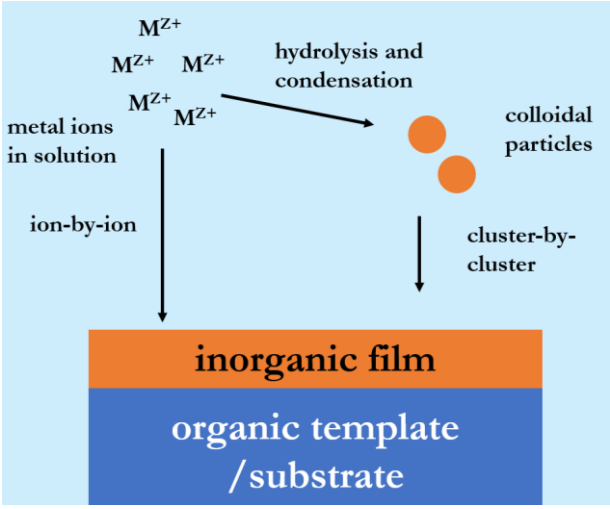

Figure 2.28: Schematic representation of two main deposition processes which lead to the formation of a thin inorganic film on templated substrate in soultion: by ion-ion process, cluster-by-cluster process, or mixed. Adapted from [105].

In this thesis at hand, the CBD method was utilized to synthesize highly porous organic/inorganic hybrid materials to increase the stability of the PS porous polymers against harsh organic solvents and high temperatures. The inorganic functional phase of choice was zinc oxide (ZnO), which is widely used as a semiconductor with tunable optical properties and potential applications in catalysis, photovoltaic and optoelectronic. The synthesis of nanocrystalline ZnO particles following CBD is a well-established method and provides smooth, homogeneous films [106]. ZnO has been synthesized in confined spaces, where the pore size of the host matrix defined the shape and size of the obtained nanoparticles. For instance, nanocrystalline, size-selected ZnO was deposited inside the pores of a "wormhole" mesoporous silica [107]. Applying an organometallic route ZnO species were hosted in the matrix of MCM-48 [108]. Furthermore, ZnO nanoparticles confined in mesoporous carbon [109] and zeolites [110] were synthesized. In contrast to the above described ZnO/host matrix nanocomposites suspended in solution, biotemplated three-dimensional ZnO nanonetworks [111], macroporous foams [112], foams with string-beaded morphology [113], nanotubes within the nanochannels of porous anodic alumina templates [114], and densely packed ZnO nanowires in confined space [115] were produced as well.

2.4.2. Synthesis of Porous PS/ZnO Hybrid Materials

Proof of Principle:

As a first step towards a new class of highly porous organic/inorganic hybrid materials with pore size smaller than 50 nm, the mineralization of porous polystyrene with a relatively large pore diameter of d_{pore} = 1.21 ± 0.28 μm was performed as a proof of principle [98]. As described in section (2.3.3) these porous polystyrene was obtained via the NF-CID method using colloidal crystals of relatively polydisperse PS nanoparticles with $d_{particle}$ = 48 nm amd Ø = 78 %, adjusting p = 250 bar, T = 65 °C, and t_{exp} = 15 min (see Figure 2.21). In order to mineralize ZnO on the pore walls of the porous polymers, the CBD method was applied on a cube of porous PS polymer, which is generally described by [116]. In brief it consists of the following steps: Zinc acetate dihydrate, used as a zinc source, was hydrolyzed slowly in a methanol solution at slightly elevated temperature (60 °C). As a consequence of homogeneous or heterogeneous nucleation ZnO nanoparticles were formed, leading to the formation of a thin ZnO layer on the pore wall. The mineralization was performed in presence of the base tetraethylammonium hydroxide (TEAOH), which is needed to stabilize the pH, while polyvinylpyrrolidone (PVP) was used as a structure-directing agent to control the size of ZnO particles within the nanometer range.

In order to get a thicker inorganic film, the solution was refreshed every 1.5 h (1 deposition cycle), because after this time, agglomeration processes start to dominate over the particle formation [117]. As can be seen in the SEM image of Figure 2.29 (top, right), the morphology of the initial porous PS polymer (Figure 2.29, top, left) is preserved after 10 ZnO deposition cycles, and an approximately 50 nm thick inorganic film is formed on the pore walls (approx. 200 nm). The top inset in Figure 2.29 (top, right) clearly shows the smooth polymer walls and the granular ZnO film. The chemical composition analysis by SEM/EDX (Figure 2.29, bottom) confirmed the deposition of ZnO on the polymer walls. As the ZnO layers are considerably thinner than the penetration depth of the electrons (ca. ~ 500 nm), the carbon signal observed in the EDX spectrum correlates to the underlying polymer substrate. Furthermore, since the applied mineralization approach allows for a precise control of the inorganic film thickness within several nanometers, the diameter of the pores can also be finely tuned by varying the number of the deposited cycles.

To understand the mechanism of the ZnO mineralization of the porous polymers, one has to be aware of the fact that charged pore walls are needed for the formation of an inorganic film. While the styrene monomer itself possess uncharged functional groups, the SDS molecules used in the emulsion polymerization provide the charging of the hydrophobic pore walls via the incorporation of the hydrophobic alkyl chains in the polymerized polystyrene particles pointing their charged polar heads outwards. When the colloidal crystals of closely packed PS nanoparticles are foamed, the sulfate groups become a part of the pore walls making them polar and appropriate for the mineralization process avoiding further hydrophilization post-treatment steps (e.g., O_2-plasma).

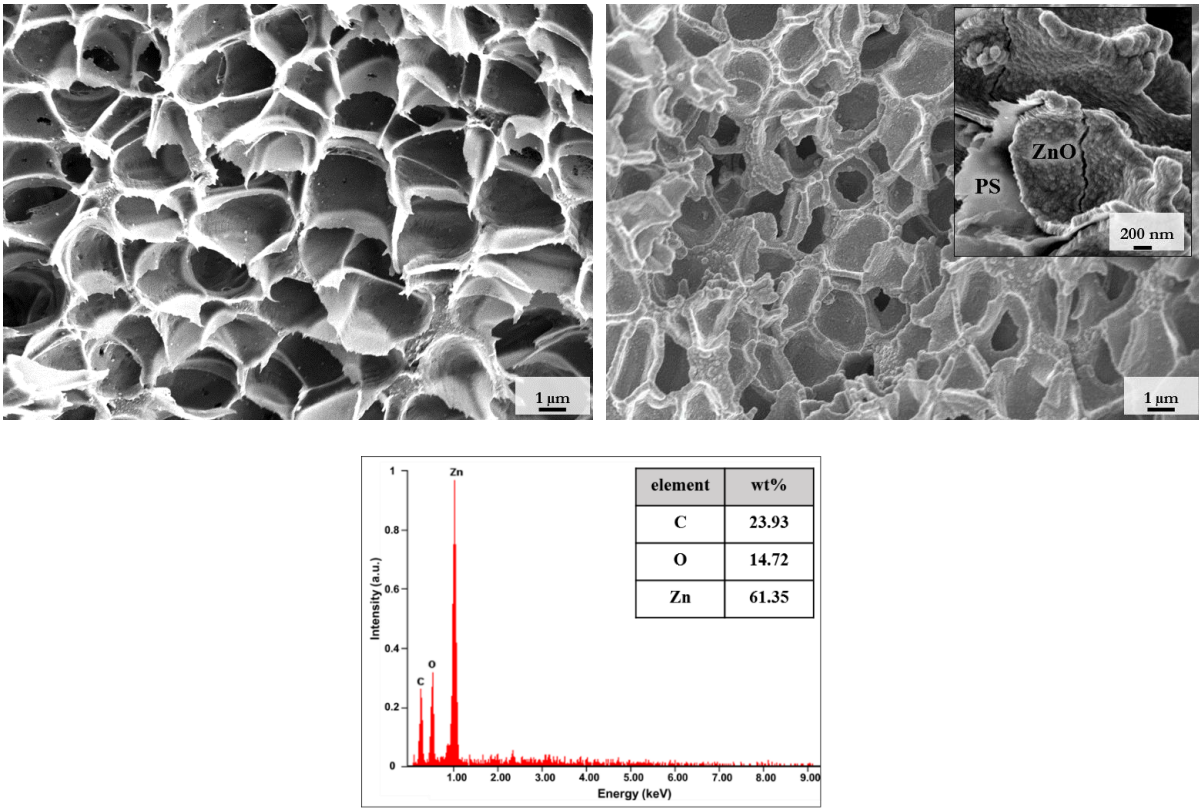

Figure 2.29: (top, left) SEM image of a porous PS polymer obtained via the NF-CID method from colloidal crystals of closely packed PS nanoparticles ($d_{particle}$ = 48 nm) filled with $scCO_2$ at p = 250 bar, T = 65 °C, and an exposure time of 15 min. (top, right) SEM image of the porous PS/ZnO hybrid material obtained after 10 ZnO deposition cycles. The upper inset represents ZnO mineralized pores with smooth polymer walls and the granular ZnO film. (bottom) EDX elemental analysis of porous PS/ZnO hybrid, which confirms the mineralization of PS foams.Taken from [98].

However, the detailed study of the obtained porous PS/ZnO hybrid materials showed that the porous polymer was not completely mineralized, i.e. the mineralization took place only on the outer surface of the porous polymer. This observation can reasonable be explained

by the closed-cellular morphology of the used porous polymers. Thus, the presence of open-cellular morphology and charged pore walls are essential for the successful infiltration and subsequent mineralization of the porous polymer.

Mechanical Properties of Porous PS and PS/ZnO Hybrid Materials

The mechanical properties of the porous PS polymer with d_{pore} = 1.21 ± 0.28 µm synthesized by the NF-CID method and the porous PS/ZnO hybrid material obtained after mineralization (SEM images in Figure 2.29) have also been investigated by carrying out uniaxial compression studies. The stress/strain curves are shown in Figure 2.30. Both materials show a behavior which is known for solid foams [118]. Thus, the curves can be divided in two regimes, i.e., a linear-elastic regime (due to the cell wall bending) and a plateau regime of deformation (controlled by the elastic buckling and subsequent failure of the cell walls). Analyzing the stress/strain curves, an elastic modulus of $E_{porous\text{-}PS}$ = 26.7 MPa and a yield stress of 1.20 MPa were found for the porous PS polymer (blue), while larger values of $E_{PS/ZnO}$ = 37.4 and 1.75 MPa were found for the porous PS/ZnO hybrid, as expected due to the presence of the ZnO layer.

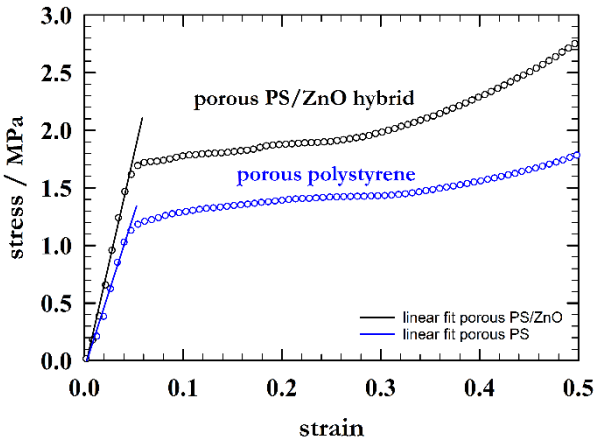

Figure 2.30: Stress/strain curves of the porous PS polymer with dpore = 1.21 ± 0.28 µm (blue) and the porous PS/ZnO hybrid material (black) (shown in Figure 2.30) obtained by uniaxial compression test. An elastic modulus of $E_{porous\text{-}PS}$ = 26.7 MPa and a critical stress of 1.20 MPa was found for porous PS polymer (blue), while larger values of $E_{PS/ZnO}$ = 37.4 and 1.75 MPa were found for the porous PS/ZnO hybrid material, as expected due to the presence of the ZnO layer. Take from [98]

The value found for the yield stress of the porous PS polymer is comparable with data found in literature. According to [119], the yield stress of porous polystyrene decreases with decreasing pore size and density of the foam. They studied a porous polystyrene with a pore

size of 5 μm and a density of 0.3 g cm^{-3}, and found a critical stress of 11.1 MPa, which is one order of magnitude larger than the porous polystyrene investigated in the study at hand. Taking into account that the porous polystyrene studied here has a smaller pore diameter of 1.21 ± 0.28 μm and an expected lower density, the obtained lower yield stress is in a agreement with the trends discussed by Arora et al. [119].

Mineralization of the interconnected porous polymer

In view of the overall goal of this part of the thesis to provide robust porous materials with pores smaller than 50 nm the interconnected porous polystyrene obtained via the modified NF-CID method (Figure 2.25) was placed in ZnO deposition solution and mineralized with 10 deposition cycles. As can be seen from the SEM images in Figure 2.31, the morphology of the initial interconnected porous polystyrene (Figure 2.31, left) is preserved in the obtained porous materials (Figure 2.31, right). Compared to the mineralization experiment of the porous polymer with d_{pore} = 1.21 μm (Figure 2.29), where a thin ZnO film was formed on the PS pore walls, only single ZnO particles or clusters of ZnO particles were observed on the pore walls of the interconnected porous polystyrene with 50 nm pore size.

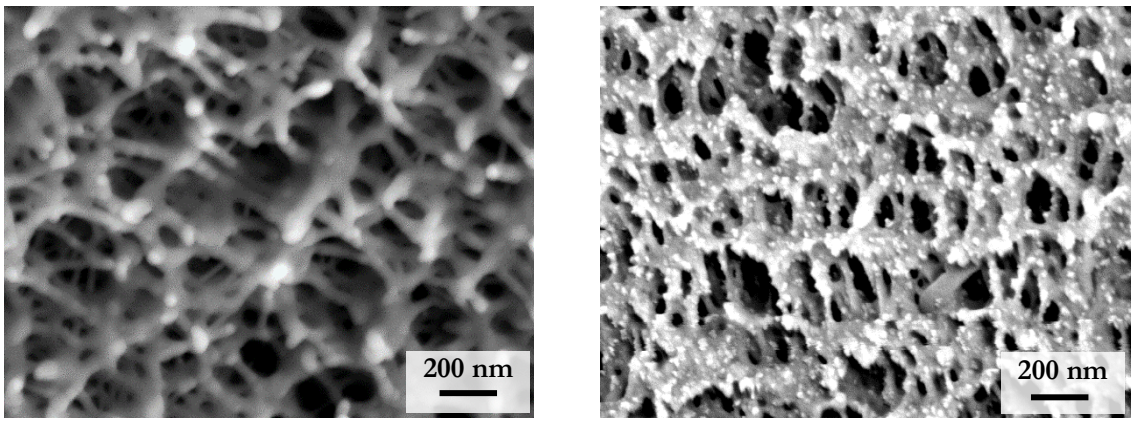

interconnected porous polystyrene **interconnected porous PS/ZnO hybrid material**

Figure 2.31: (left) SEM image of interconnected porous polystyrene obtained via the two-stage NF-CID method. (right) SEM image of interconnected porous PS/ZnO hybrid material obtained after 10 ZnO deposition cycles.

In order to study whether the mineralization process has only taken place at the outer surface or also the inner surface of the interconnected porous polystyrene an EDX mapping analysis was performed. The results shown in Figure 2.32 revealed that most of the formed

ZnO particles were indeed deposited mainly on the outer surface of the interconnected polystyrene rather than on the inner surface.

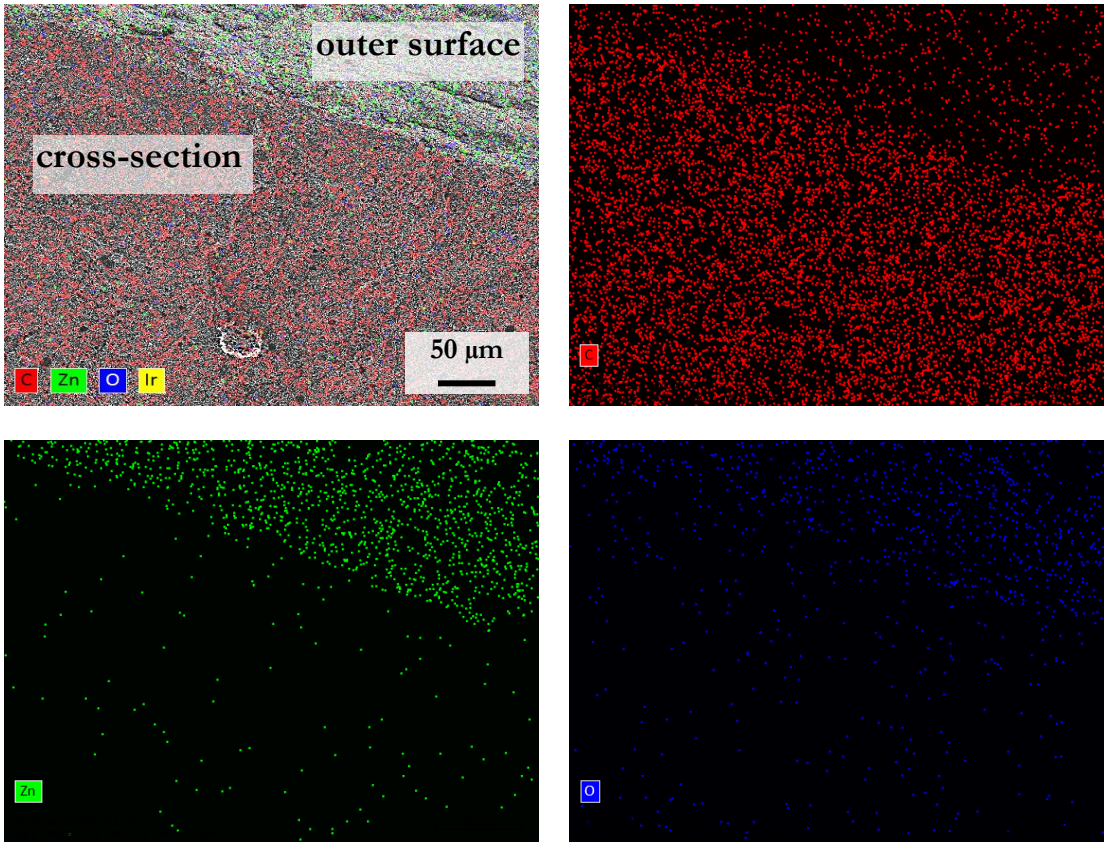

Figure 2.32: EDX mapping elemental analysis showing the composition of the interconnected nanoporous polystyrene after 10 ZnO mineralization cycles. (top, left) overlapped EDX map followed by separate map images of (top, right) carbon, (bottom, left) zinc and (bottom, right) oxygen. The analysis reveals that the mineralization occurred mostly on the outer surface of the interconnected porous polystyrene.

Unfortunately, these first experiments on the synthesis of porous PS/ZnO hybrid materials with pore size smaller than 50 nm were not successful. The reason could be manifold at first, the mineralization process and conditions might be depending on the size of the confinement. Second, the hindered diffusion of the diffusion of the mineralization solution in the interconnected porous polymer might be an issue and last but not least the pore walls generated by the modified NF-CID process might not fully covered with SDS molecules and thus not enabling the formation of ZnO film due to the lack of charges.

Therefore, the next steps towards the synthesis of a porous organic/inorganic hybrid materials are to investigate the influence of the confinement on the mineralization process, the influence of the diffusion in nanopore and the composition of the outer and inner surfaces.

3 Catalysis in Liquid-Confined Spaces

This chapter aims to explore the influence of liquid confinement on the asymmetric Rh catalysis using the 1,2-addition of boroxine **2** to *N*-tosylimine **1** in the presence of $[RhCl(C_2H_4)_2]_2$ and chiral diene ligands as a benchmark reaction (scheme 3.1). The influence of the confinement on homogeneous organometallic catalysis was investigated by utilizing cyclodextrins [14], self-assembled container molecules [9,15], micellar-based systems [16,120], water-in-oil and oil-in-water microemulsions [17] and much more [18]. In particular, Rh-catalyzed asymmetric additions were often investigated in micellar systems [120]. However, asymmetric catalysis with Rh-diene complexes in bicontinuous microemulsions has not been reported so far. Therefore, the influence of microemulsions as organized nanostructured reaction media for Rh-catalyzed asymmetric 1,2-addition will be investigated for the first time.

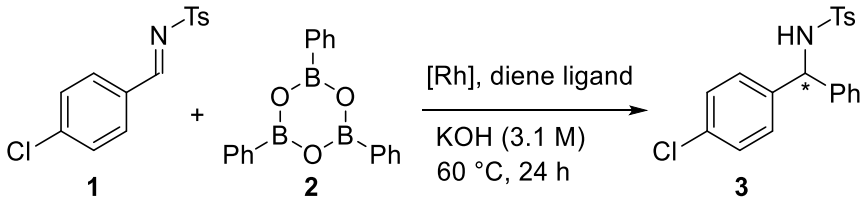

Scheme 3.1: Envisioned Rh-catalyzed asymmetric 1,2-addition of boroxine **2** to *N*-tosylimine **1** in the presence of a chiral diene ligand.

This benchmark system contains multiple components, i.e. nonpolar, slightly polar reactants, aqueous/organic solvent mixtures and a base, which often requires careful optimization of the reaction conditions due to slow reaction rates and poor yields [121–123]. Thus, we expect that bicontinuous structured microemulsions would overcome the limitations of conventional solvents caused by mass transport due to the existence of polar and nonpolar nano-domains. Additionally, the location of reactants **1** and **2** and the Rh/ligand complex within either the polar or nonpolar nano-domains or at the amphiphilic film of the microemulsion will have a strong influence on the catalysis. Thus, by tuning the polarity of Rh-catalyst systems the location of the catalyst will be varied. Therefore, two series of novel chiral diene ligands **4** - **6** with different polarities (scheme 3.2) were utilized in this study. For instance, ligands **4** create a symmetric, relatively nonpolar ligand sphere around the Rh center, whereas the unsymmetrically substituted ligands **5** and **6** generate a less symmetric and much more polar environment around the Rh center.

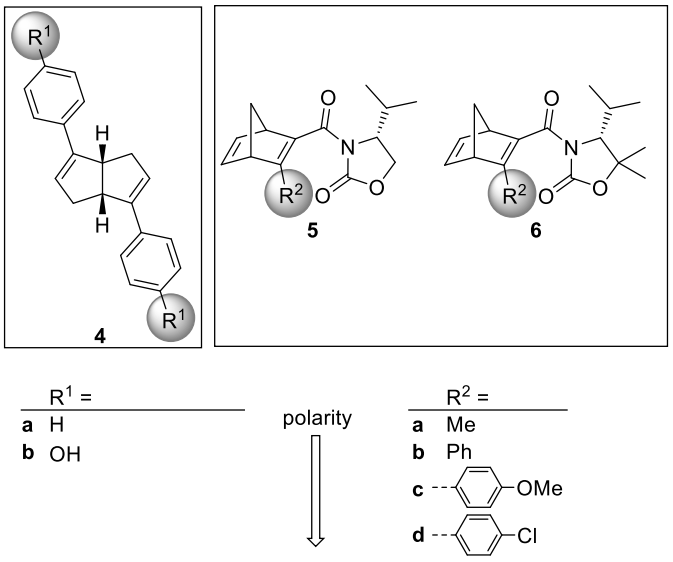

Scheme 3.2: Chiral diene ligands for the investigated Rh-catalyzed asymmetric 1,2-addition of boroxine **2** to N-tosylimine **1**.

The homogeneous Rh-catalyzed asymmetric 1,2-addition of boroxine **2** to *N*-tosylimine **1** is usually performed in dioxane or toluene a reaction medium [121,123]. However, water and dioxane are miscible, thus, we decided to formulate a balanced microemulsion of water and toluene. After the formulation of a bicontinuous microemulsion for this asymmetric 1,2-addition, a series of the homogeneous Rh-catalyzed asymmetric 1,2-addition applying the different ligands was performed in the microemulsion and compared with the results in conventional reaction media (toluene and dioxane).

This chapter begins with a short introduction on microemulsions, their phase behavior, their nanostructures, and the characterization via scattering methods. Secondly, it includes a brief background about the Rh-catalyzed asymmetric 1,2-addition and a description of the reaction mechanism (catalytic cycle). Thereafter, the results are discussed, which begins with the formulation and characterization of the toluene-based balanced microemulsion, followed by the results obtained from catalysis in both the conventional solvents and the nanostructured microemulsion, and then the kinetic studies performed on the Rh-catalyzed asymmetric 1,2-addtion applying different ligands as described. The chapter ends with a general conclusion and outlook.

This chapter summarizes the results of an ongoing collaborative research with the workgroup of Prof. Dr. Sabine Laschat from the Institute of Organic Chemistry of the University of Stuttgart. The ligands that were investigated in this work were synthesized by Laschat's group, where all reactions were also carried out.

This chapter is based on the published article:

M. Deimling[+], M. Kirchhof[+], B. Schwager[+], Y. Qawasmi[+], A. Savin, T. Mühlhäuser, W. Frey, B. Claasen, A. Baro, T. Sottmann, S. Laschat, Asymmetric Catalysis in Liquid Confinement: Probing the Performance of Novel Chiral Rhodium–Diene Complexes in Microemulsions and Conventional Solvents, *Chem. Eur. J.* **2019**, *25*, 9464.

Author Contributions:

The author was assisted by Mrs. Barbara Schwager, Mr. Max Deimling, and Mr. Manuel Kirchhof. B. Schwager conducted parts of the phase diagram measurements. M. Deimling and M. Kirchhof synthesized the ligands and performed the catalyses.

3.1. Basics of Microemulsions and Asymmetric 1,2-Addition

3.1.1. General Introduction and Phase Behavior of Microemulsions

Microemulsions are thermodynamically stable and macroscopically homogeneous mixtures of at least two immiscible components (e.g. water and oil) and an amphiphilic component. Contrary to regular solutions, microemulsions are composed of nanometer-scaled water- and oil-domains separated by an amphiphilic film. The amphiphilic film is formed due to the adsorption of the amphiphilic component at the interface between oil and water. As a result of their adsorption at the interface, the interfacial tension σ_{AB} between the water-phase and oil-phase decreases drastically. Adjusting the properties of the amphiphilic film by several parameters e.g. temperature, pressure, co-surfactant/surfactant ratio or electrolyte concentration, a variety of nanostructures are accessible ranging from spherical over cylindrical droplets to network-like and bicontinuous structures [124–126].

The amphiphilic components, i.e. surfactants, consist of both a hydrophilic and a lipophilic part. The lipophilic part of the surfactant (tail) is usually a long hydrocarbon chain, while the hydrophilic part (head) can be ionic or non-ionic. According to the nature of the head group, the surfactants can be classified into four categories: anionic, cationic, zwitterionic, and non-ionic surfactants. The so-called "n-alkyl polyglycol ether" (C_iE_j) surfactants (see scheme 3.3), in which the ethylene oxide units form the surfactant head group, are considered as one of the most common non-ionic surfactants.

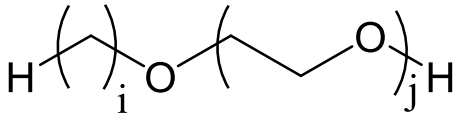

Scheme 3.3: General chemical structure of n-Alkyl polyglycol ether (C_iE_j) surfactants.

Ternary or pseudo-ternary microemulsion systems exhibit a rich phase behavior showing one-phase microemulsion, two-phase and three-phase states. Therefore, studying the phase behavior of these systems is the key point to understand the properties of a microemulsion. Since only non-ionic surfactants were used in this study, the following part will consider only microemulsions stabilized by non-ionic surfactants. The phase behavior will be explained and discussed based on ternary systems of the type water – oil – C_iE_j.

Phase Behavior

The phase behavior of ternary systems of the type water (A) – oil (B) – non-ionic surfactant (C) at constant pressure can be represented using the Gibbs phase triangle. Because of the complex phase behavior of the ternary system, it is helpful to consider firstly the phase diagrams of the corresponding binary systems of water (A) – oil (B), oil (B) - non-ionic surfactant (C), and water (A) – non-ionic surfactant (C) [127]. Figure 3.1 shows the phase behavior of the three corresponding binary systems.

The binary system water (A) – oil (B) is the simplest one. It shows a normal behavior of water and oil mixtures, where these two components are immiscible, i.e. the miscibility gap extends over almost the whole composition and temperature range and the upper critical point lies above the boiling point of the mixture. The phase diagram of the binary system oil (B) – non-ionic surfactant (C) exhibits a lower miscibility gap with an upper critical point cp_{α}. The corresponding critical temperature T_{α} depends on the nature of both the surfactant and the oil. Generally, it holds that, the more hydrophilic the oil or the more hydrophobic the surfactant, the lower T_{α}. The binary phase diagram of the system water (A) – non-ionic surfactant (C) has a lower miscibility gap lies far below the melting point of the mixture and thus can be neglected. In addition, the system exhibits an upper miscibility gap with lower critical point cp_{β}. The shape of the upper miscibility gap and the corresponding critical temperature T_{β} also depends on the nature of surfactant. For hydrophilic surfactants T_{β} is found at high temperatures.

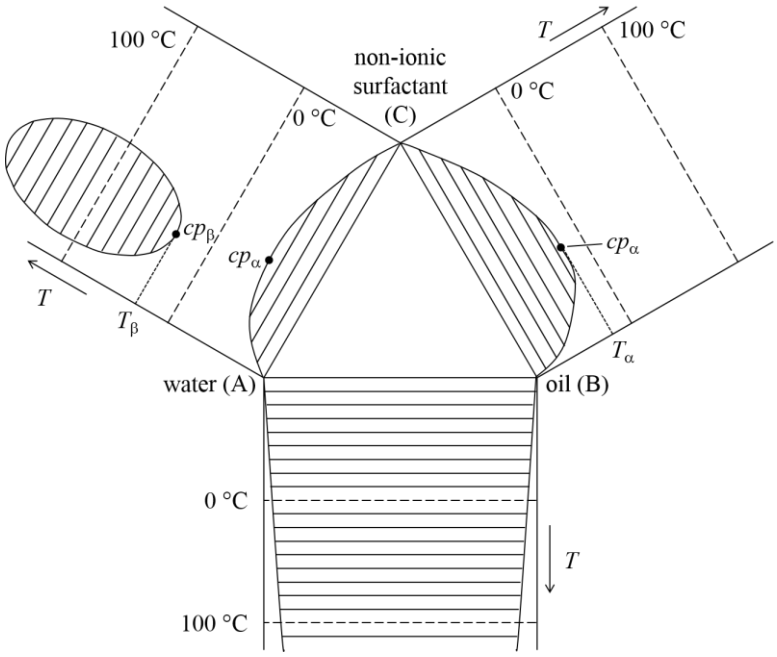

Figure 3.1: Schematic view of the phase behavior of three binary systems of water (A), oil (B) and non-ionic surfactant (C) at constant pressure. A – B are mutually immiscible, while B – C binary system shows a lower miscibility gap. The A – C binary system shows a lower miscibility gap at temperatures below 0 °C and an upper miscibility gap. Redrawn from [127].

If the three binary phase diagrams are combined and flipped up, one obtains a phase prism of the ternary system water (A) – oil (B) – non-ionic surfactant (C) as shown in Figure 3.2. Otherwise stated, the phase prism is composed by stacking many isothermal Gibbs phase triangles, representing the interplay between the three binary systems at different compositions and temperatures. The complex behavior of the ternary system is mainly a result of the overlap between the lower miscibility gap of the oil (B) – non-ionic surfactant (C) system and the upper miscibility gap of the water (A) – non-ionic surfactant (C) system. For instance, the non-ionic surfactant is mostly soluble in water at low temperatures, whereas it prefers oil at high temperatures. This characteristic property of the surfactant as a function of temperature is due to the weakening of the hydrogen bonds between the water and the ethoxy units in the surfactant head group with increasing temperature [128]. The temperature-dependent amphiphilic properties of the non-ionic surfactant is the main reason for the significant temperature-dependence of the phase behavior of the ternary system.

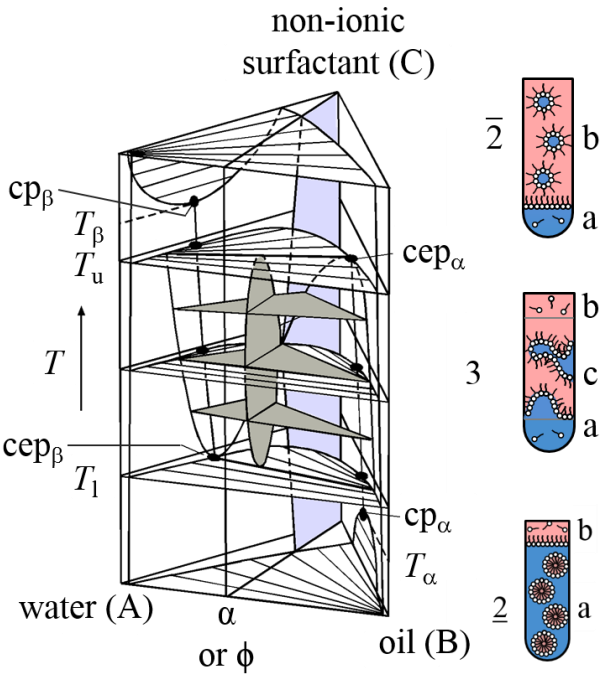

Figure 3.2: Schematic phase prism of the system water (A) – oil (B) – non-ionic surfactant (C). The temperature-dependent phase behavior of the three components is generated by stacking isothermal phase triangles. The cross-section drawn at a constant water-to-oil ratio α is the so-called $T(\gamma)$-section. The three-phase region is colored in grey, while the one-phase region is colored in violet [129].

At temperatures lower than T_l, an oil-in-water microemulsion (a) coexists with an oil-excess phase (b). This state is denoted as **2**, the dash points out the position of the surfactant-rich phase as shown in the lower test tube in Figure 3.2, right. Increasing the temperature above T_l, the solubility of the surfactant in water decreases gradually, while its solubility in oil increases. Consequently, a three-phase region **3** appears, in which a surfactant-rich or middle-phase (c) coexists with an oil- and water-excess phase as represented in the middle test tube in Figure 3.2, right. Further temperature increase leads to the formation of a water-in-oil microemulsion (b) coexists with a water-excess phase as shown in the upper test tube Figure 3.2, right. Since the density of the surfactant-rich oil phase is usually lower than the one of water excess-phase this state is denoted as $\overline{\mathbf{2}}$.

The determination of the entire phase prism of the type shown in Figure 3.2 is quite complex and time-consuming. Nevertheless, studies showed that the investigation on different sections through the phase prism are more convenient for understanding and describing the phase behavior of ternary systems. Typically, the sections are taken at fixed ratio of two components and the composition of the third component is varied as a function of temperature as shown in Figure 3.3. [126]

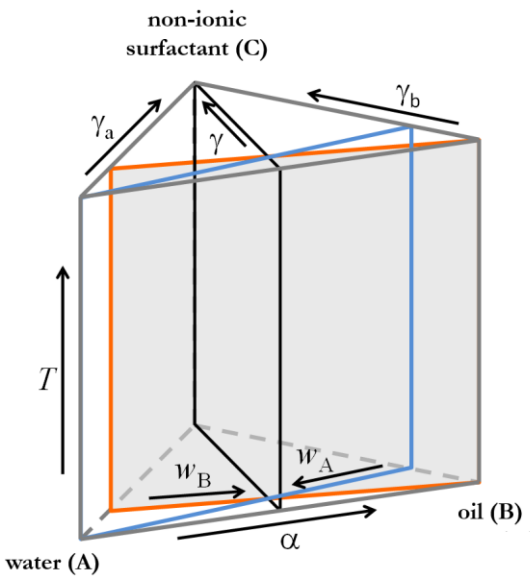

Figure 3.3: Phase prism of a ternary system with highlighted sections: (black) The $T(\gamma)$ section at constant oil mass fraction in the water-oil mixture, (orange) the $T(w_B)$ section at a constant mass fraction of surfactant in the water-surfactant mixture, and (blue) the $T(w_A)$ section at a constant mass fraction of surfactant in the oil-surfactant mixture. [126]

A useful section is the $T(\gamma)$ section or the so-called fish-cut diagram at a constant oil mass fraction α in the mixture of oil and water:

$$\alpha = \frac{m_B}{m_A + m_B} \qquad (1)$$

where m_B and m_A are the mass of oil and water, respectively. The $T(\gamma)$ section is determined as a function of the temperature and the overall surfactant mass fraction γ:

$$\gamma = \frac{m_C}{m_A + m_B + m_C} \qquad (2)$$

where m_C is the mass of surfactant.

An exemplary $T(\gamma)$ section though the phase prism is highlighted in Figure 3.4 with sketched test tubes demonstrating the different phase behaviors. As can be seen, the phase boundaries resemble the shape of a fish, which is why $T(\gamma)$ section is also referred to as fish-cut.

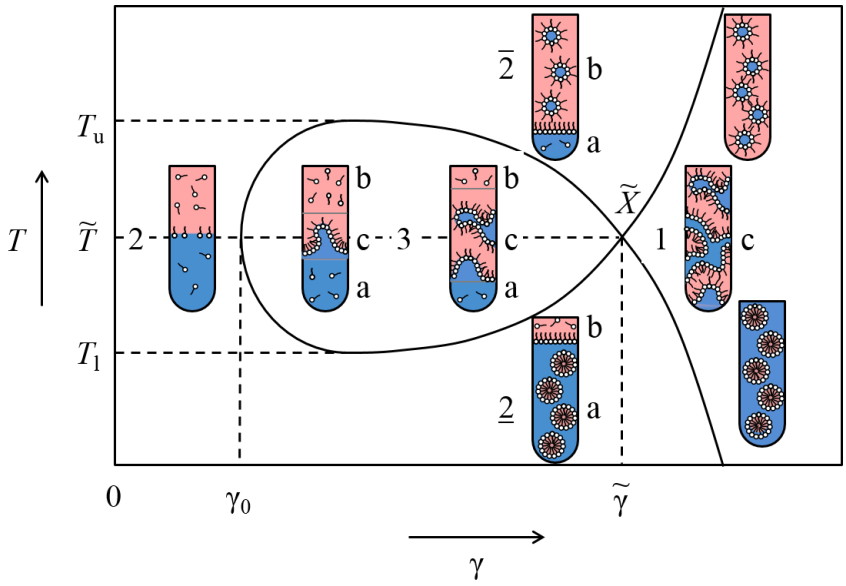

Figure 3.4: *T*(γ)-section of the microemulsion system water (A) – oil (B) – non-ionic surfactant (C) at constant oil mass fraction α. The test tubes show the state of the system at different temperatures and surfactant mass fractions γ. $\underline{2}$: coexistence of an oil-in-water microemulsion with an oil-excess phase. $\overline{2}$: coexistence of water-in-oil microemulsion with a water-excess phase. **1**: one phase microemulsion. **3**: coexistence of a microemulsion phase with water- and oil-excess phases. At surfactant mass fractions below γ_0 the surfactant is either dissolved monomerically in both phases or absorbed at the macroscopic interface [126,130].

At surfactant mass fraction γ lower than γ_0, the surfactant is mostly monomerically soluble in both water- and oil-phases and partially adsorbed at the interface between the two phases. Here, the water- and oil-phase coexist over the entire temperature range. At surfactant mass fractions $\gamma_0 < \gamma < \tilde{\gamma}$, the excess surfactant will preferentially dissolve in the water-phase at low temperatures. Thus, an oil-in-water microemulsion coexists with an oil-excess phase $\underline{2}$. At high temperatures, however, the surfactant prefers the oil-phase which lead to the formation of a water-in-oil microemulsion in coexistence with a water-excess phase $\overline{2}$. At intermediate temperatures, the surfactant is almost equally soluble in both water and oil. Here, a three-phase region **3** appears, i.e. a surfactant-rich bicontinuously structured phase and two excess phases of water and oil. Close to $\tilde{\gamma}$ the surfactant-rich bicontinuously structured phase has a small volume which increases with increasing surfactant mass fraction at intermediate temperatures. At the same time, the volume of the two excess phases decreases. In the range of $\gamma_0 < \gamma < \tilde{\gamma}$ the following phase transition sequence $\underline{2} \rightarrow 3 \rightarrow \overline{2}$ can be found with increasing temperature. This phase inversion behavior is attributed to the gradual change of the solubility of the surfactant in the water and oil phase.

At the so-called optimum point $\tilde{X}$ where γ is equal to $\tilde{\gamma}$, the three-phase region disappears and the one-phase microemulsion **1** appears. By increasing the amount of surfactant mass fraction γ, the one-phase region extends. The $\tilde{X}$ point defines the minimum amount of surfactant needed to solubilize the water and oil at a given α, which also indicates the efficiency of the surfactant, as well as the corresponding temperature $\tilde{T}$, which indicates the phase inversion temperature PIT.

3.1.2. Nanostructures of Microemulsions

As already mentioned, microemulsions are not molecular dispersion solutions but structured mixtures of three components. In microemulsions, the surfactant molecules adsorb at the interface between the water- and the oil-phase and form an amphiphilic film. Depending on the properties of the amphiphilic film, microemulsions with various nanostructures are feasible. The nanostructure and the corresponding phase behavior of microemulsions can be understood with the local curvature of the amphiphilic film. Mathematically, the curvature can be described by two principal curvatures c_1 and c_2 at any point [125]:

$$c_1 = \frac{1}{R_1} \quad \text{and} \quad c_2 = \frac{1}{R_2} \tag{3}$$

where R_1 and R_2 are the principal curvature radii. Figure 3.5 shows the radii of a spherical and a sponge-like structure, which refer to a micellar and a bicontinuous microemulsion structure, respectively.

The mean curvature H of the amphiphilic film is given by:

$$H = \frac{1}{2}(C_1 + C_2) \tag{4}$$

By definition the curvature H is positive if the amphiphilic film is curved around the oil (oil-in-water microemulsions) and negative if it is curved around the water (water-in-oil microemulsions).

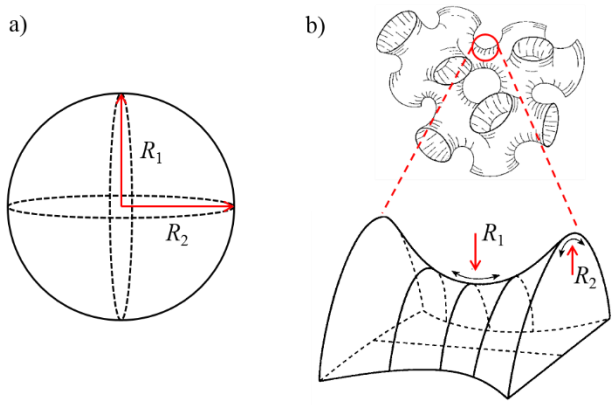

Figure 3.5: The principal curvature radii R_1 and R_2 of (a) a spherical and (b) a sponge-like structure. Redrawn form [131].

To differentiate nanostructures in microemulsions with the mean curvature H, one must consider the effect of temperature on the molecular structure of the surfactant and thus on the amphiphilic film. For instance, the head group of the non-ionic surfactant C_iE_j is strongly hydrated at low temperatures. Therefore, the effective hydrophilic head group requires a relatively large space at the interface, while the hydrophobic chains have a relatively small effective size in comparison. As a consequence, the amphiphilic film is curved around the oil because of the head group size is much larger than the chain volume. This leads to an oil-in-water microemulsion with a mean curvature of $H > 0$ as shown in Figure 3.6, bottom.

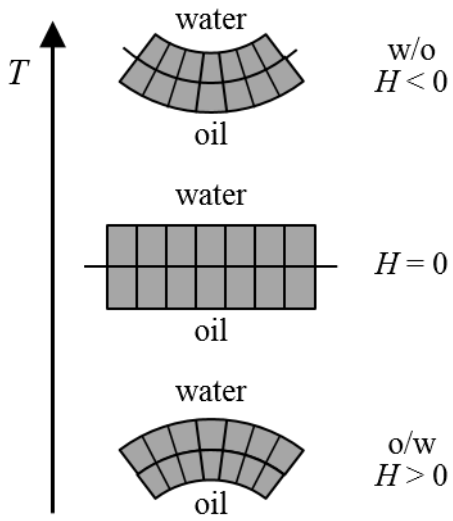

Figure 3.6: Mean curvature H of a non-ionic surfactant film at the water/oil interface as a function of temperature T. The surfactant molecules are sketched in a wedge- or rectangular-shape. The decrease in H with increasing T is due to the shrinkage of the hydration shell of the surfactant head group, while the effective size of the hydrophobic tail increases compared to that of the head group. [126]

Increasing the temperature gradually, the head group partially dehydrates thereby the effective size of the head group decreases. On the other hand, the size of the hydrophobic chain increases due to the increasing number of possible chain conformations. These trend leads to a gradual change of the curvature of the amphiphilic film from $H > 0$ at low temperatures (Figure 3.6, bottom) to $H < 0$ at high temperatures (Figure 3.6, top) via a locally planar film with $H = 0$ at intermediate temperatures (Figure 3.6, middle).

Nanostructure of balanced microemulsions

It has been proved that the phase behavior and the phase inversion are related to the curvature of the amphiphilic film, from the comprehensive investigation on the nanostructure of non-ionic microemulsions. The relation between the phase behavior and the nanostructure of the balanced microemulsion, i.e. a microemulsion at a constant water-to-oil ratio of $\alpha = 0.5$, is discussed and schematically shown in Figure 3.7.

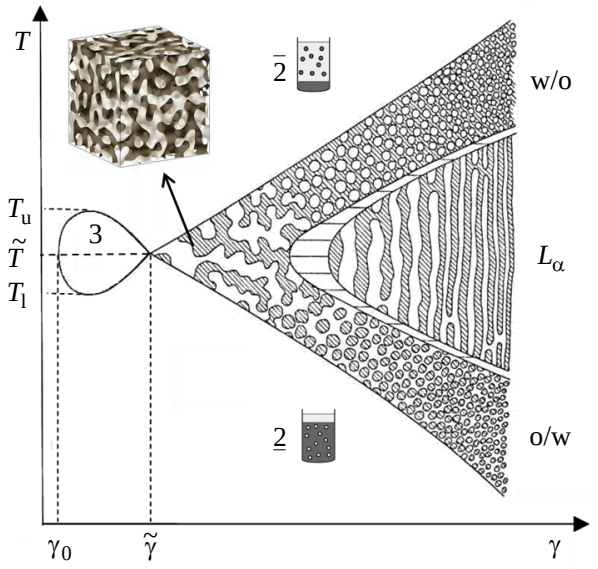

Figure 3.7: $T(\gamma)$-section of a balanced non-ionic microemulsion system at $\alpha = 0.5$ with the corresponding nanostructures. The change of the nanostructure with increasing temperature is correlated to the temperature dependence of the mean curvature H of the amphiphilic film: an oil-in-water microemulsion exists at low temperatures, a water-in-oil microemulsions appears at high temperatures, while at intermediate temperatures $T \approx \tilde{T}$ a bicontinuous or $L\alpha$-phases are formed. The inlet represents a bicontinuous sponge-structure taken from [125].

At far low temperatures $T << \tilde{T}$, the amphiphilic film is curved around the oil due to the hydration of the head group of the surfactant ($H > 0$). Accordingly, at low surfactant mass fraction $\gamma < \tilde{\gamma}$, a small amount of the oil can be solubilized in water in form of droplets

with a relatively small radius. Thereby, most of the oil becomes the excess phase which coexists with the water-in-oil microemulsion. At a constant temperature, the number density of the microemulsion droplets increases with increasing γ and therefore more oil is solubilized. After reaching enough amounts of the surfactant, the oil-excess phase disappears and a single-phase microemulsion consisting of densely packed oil-droplets in water appears.

By increasing temperature, but still $T < \widetilde{T}$, the curvature of the amphiphilic film decreases. Thereby, the droplet size increases and more oil is solubilized. Consequently, at higher temperatures (still below the $\widetilde{T}$) the formation of a single-phase microemulsion can be observed. This contributes to the trend of boundary $\underline{2} \rightarrow 1$ with increasing T.

At intermediate temperatures $T \approx \widetilde{T}$, the curvature of the amphiphilic film decreases and reaches $H = 0$. Thus, at $\gamma > \tilde{\gamma}$ the droplets lose their spherical shape and form a bicontinuous sponge-like structure. In this case, the macroscopically connected water- and oil-domains are separated by a continuous amphiphilic film. The bicontinuous structure can be described with the characteristic length scale ξ, which can be interpreted as the "mean diameter" of the formed oil- or water-domains and defined as:

$$\xi = \frac{d_{TS}}{2} \qquad (5)$$

with the periodicity d_{TS}, which can be obtained from small-angle neutron scattering (SANS) or small-angle X-ray scattering (SAXS) experiments. The maximum value of the characteristic length scale ξ can be found at the optimum surfactant mass fraction $\tilde{\gamma}$. By increasing the surfactant mass fraction, the characteristic length scale ξ decreases.

At high temperatures $T > \widetilde{T}$, the inverse behavior of the microemulsion emerges, i.e. the amphiphilic film is curved around the water at $T >> \widetilde{T}$ because of the dehydration of the hydrophilic head group of the surfactant ($H < 0$). This leads to the formation of small water droplets in oil. At constant γ, increasing the temperature further leads to steady decrease of the radius of the water droplets. Above the upper phase boundary shows the trend $1 \rightarrow \overline{2}$. Thereby, a surfactant-rich w/o microemulsion coexists with a water-excess phase.

3.1.3. Reactions in Microemulsions

The usage of microemulsions in organic synthesis is an intensively investigated approach. For instance, they are widely utilized as a template for the synthesis of nanoparticle and even in the preparative organic synthesis as reaction media. Therewith, the size of the nanoparticle can be adjusted, and the reaction rate can be increased [132]. The interest of organic synthesis in microemulsions is related to, on the one hand, their ability to overcome the reactants incompatibility, which is frequently encountered in organic reactions [133]. On the other hand, the formation of oil and water nanodomains in microemulsions offer enormous internal interfacial areas [134].

In the homogeneous organometallic catalysis, the usage of micellar systems as reaction media lead to an enhanced catalytic performance [135]. This enhancement was correlated with several phenomena such as the increased local concentration of the reactants inside the micelle, and the so-called medium effect, i.e. polarity, micro-viscosity, and charge effect inside the micelle. Therefore, the micellar systems are envisioned as nanoreactors [9]. Further on, also water-in-oil and oil-in-water microemulsion were utilized as a reaction media for organometallic catalysis, for instance, investigation on the palladium-catalyzed hydroxycarbonylation of 1-dodecene in w/o and o/w microemulsion revealed that the dimension of the oil–water interface and the local concentrations of the substrates at the interface, regulate the catalytic performance in these reaction media [17].

Although the homogeneous organometallic-catalyzed asymmetric reactions were successfully performed in micellar systems and water-in-oil and oil-in-water microemulsions, asymmetric catalysis in bicontinuously structured microemulsions have not been reported so far, to the best of our knowledge. Therefore, the influence of bicontinuous microemulsions as a nanostructured reaction medium on the Rh-catalyzed asymmetric 1,2-addition will be studied applying catalysts with different polarities.

3.1.4. Asymmetric 1,2-Addition

The formation of carbon-carbon bonds is a central matter in organic chemistry, in which stereochemistry plays a crucial rule. A control of the stereoselectivity is achieved using homogeneous organometallic catalysts with suitable chiral ligands. These catalyses are referred as homogeneous asymmetric catalysis and can be defined as a type of catalysis where a transition-metal complex containing a chiral ligand directs the formation of a chiral compound under homogeneous conditions.

Among others, asymmetric catalysis with chiral Rh-diene complexes has experienced much progress over the last two decades [136,137]. During that time a broad range of chiral diene ligands has been synthesized, such as bicyclic [121], acyclic [138] and planar chiral dienes [139]. Rh- and Ir-complexes containing chiral diene ligands turned out to be particularly successful for asymmetric C-C, C-O and C-N bond formations.

Rh-complexes catalyze, for example, the arylation reactions from organoboron reagent e.g. arylboronic acids. Since arylboronic acids enable simple and efficient transfer of aryl groups to metal centers through transmetallation [140]. Specific example is the Rh catalyzed asymmetric 1,2-addition of boroxine **2** to *N*-tosylimine **1** shown in scheme 3.4, which was used as a benchmark reaction in this study. For this catalysis, two series of novel chiral diene ligands **4** - **6** being suitable (see scheme 3.4) were examined in this study. On the one hand, ligands **4** were chosen because the concave diarylbicyclo[3.3.0]octadiene core creates a symmetric, relatively nonpolar ligand sphere around the Rh center, which can be controlled by attachment of substituents at the 4-position of the phenyl rings. On the other hand, the unsymmetric norbornadiene ligands **5** and **6** with the attached oxazolidinone unit generate a less symmetric and much more polar environment around the Rh center.

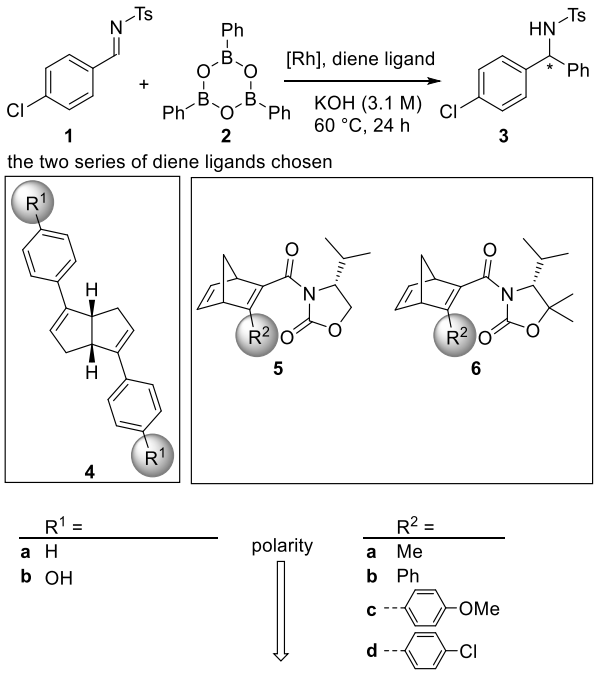

Scheme 3.4: Envisioned Rh-catalyzed asymmetric 1,2-addition of boroxine **2** to *N*-tosylimine **1** in the presence of novel chiral bicyclo[3.3.0]octadiene and norbornadiene based ligands 4 – 6.

Catalytic cycle of the Rh-catalyzed 1,2-addition

The mechanism of the Rh-catalyzed 1,2-addition of boroxine **2** to *N*-tosylimine **1** was studied using the density functional theory (DFT) calculation method based on ligand **4a** [141]. The proposed catalytic cycle is shown in scheme 3.5. In the first step, the active dimeric hydroxy Rh-complex **8** is formed from the dichloride Rh-complex **7** via an ion-exchange step (I). Then the dimeric hydroxy Rh-complex **8** dissociates to afford monomeric (monometallic) phenylboronate Rh-complex **9** via a transmetallation with phenylboronic acid **10** during which a water molecule is dissociated (II). In the next step, the monomeric phenylboronate Rh-complex **9** reacts with another phenylboronic acid **10** molecule, therewith, a diboron adduct **11** is released and the phenyl Rh-complex **12** is formed (III). Then the coordination of the *N*-tosylimine **1** to the phenyl Rh-complex **12** leads to the formation of the complex **13** (IV), which through an enantioselective arylation of the *N*-tosylimine **1** transfers into the Rh-complex **14** (V). Then the arylated Rh-complex **15** is protonated by a water molecule and the Rh-complex **16** is formed (VI). In the last step the chiral secondary arylamines **3** decoordinates and the active Rh-complex **8** is regenerated (VII).

One must take into account, that dioxane as the reaction medium and a reaction temperature of 70 °C are considered for the proposed catalytic cycle. When the Rh-catalyzed asymmetric 1,2-addition is performed in another reaction medium or other ligands are applied, different transition states may take place.

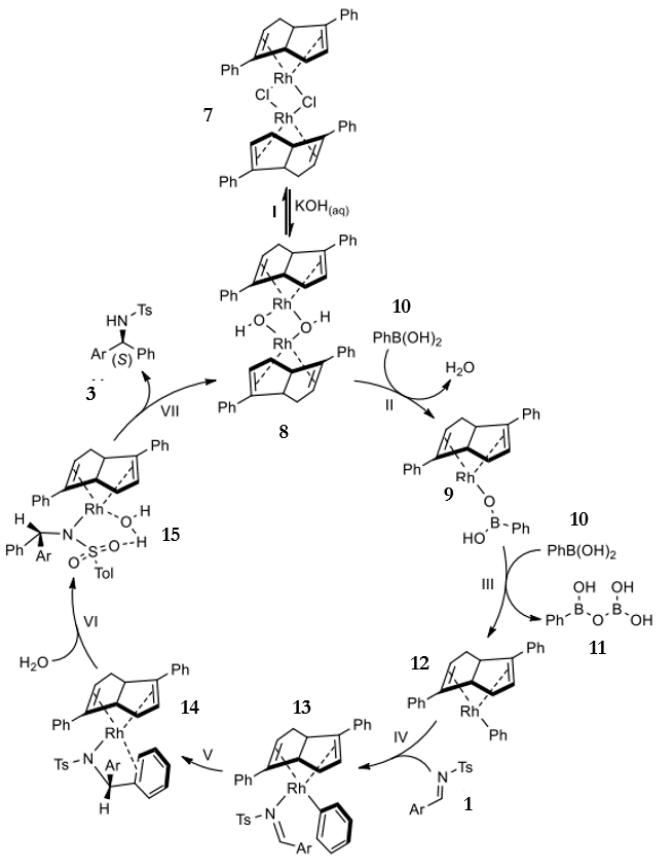

Scheme 3.5: Proposed catalytic cycle of Rh-catalyzed asymmetric 1,2-addtion of boroxine **1** to *N*-tosylimine **2** applying ligand **4a**. Based on the results of [141]

3.2. Rh-catalyzed Asymmetric 1,2-Addition in Microemulsions

The goal of this chapter is to study the effect of liquid confined spaces of bicontinuous microemulsion on the homogeneous Rh-catalyzed asymmetric 1,2-addition. Therefore, the catalysis will be conducted in a nanostructured microemulsion, as well as in conventional solvents (dioxane and toluene). Assuming that the bicontinuous structure allows for the easiest access of the catalyst/ligand system with respect to both KOH and the reactants, a thermodynamically stable bicontinuous structured microemulsion of toluene and water will firstly formulated for the Rh catalysis asymmetric 1,2-addition. The aqueous domains of the microemulsion are a good solvent for KOH, which is needed to activate catalyst/ligand system, while the hydrophobic reactants *N*-tosylimine **1** and boroxine **2** supposed to stay in the toluene domains, while the catalyst/ligand system possessing both polar and non-polar characteristic can reside in the amphiphilic film.

3.2.1. Formulation and Optimization of Microemulsions

The Rh-catalyzed asymmetric 1,2-addition is usually conducted at T = 60.0 °C, due to the limited solubility of *N*-tosylimine **1** and boroxine **2** in toluene at low temperatures. Therefore, the bicontinuous microemulsion containing water/KOH, toluene/reactants **1** and **2** as well as the surfactant and catalyst/ligand system should be stable around T = 60.0 °C. In order to formulate such a microemulsion, the system H_2O – cyclohexane – octaethylene glycol monodecyl ether ($C_{10}E_8$) was chose as starting system [142]. However, in order to avoid the formation of liquid crystalline phases and to decrease the temperature-sensitivity of the system, the surfactant ($C_{10}E_8$) was replaced by a shorter carbon chain and smaller ethylene oxide group surfactant pentaethylene glycol monohexyl ether (C_6E_5). The phase behavior of the H_2O – cyclohexane - C_6E_5 microemulsion system was investigated as a function of temperature and surfactant mass fraction γ, i.e. $T(\gamma)$-section at a constant mass fraction α = 0.50 of oil in the mixture of water and oil was recorded.

As shown in Figure 3.8, the phase boundaries show the typical behavior of non-ionic microemulsion systems.

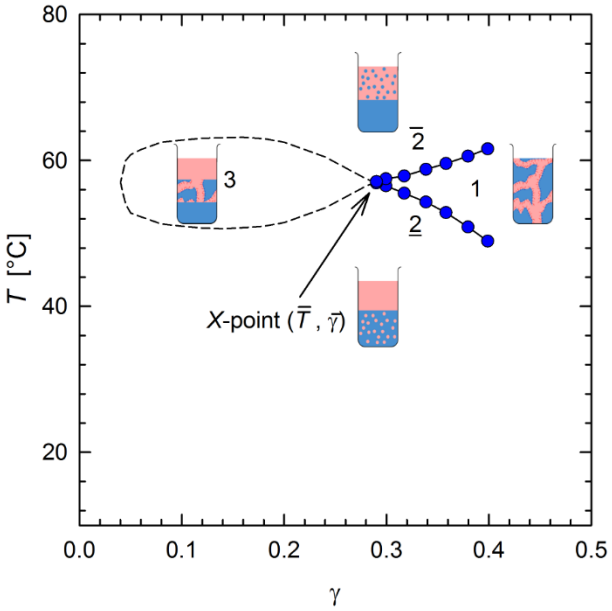

Figure 3.8: *T*(γ)-section of the system H_2O – cyclohexane - C_6E_5 (●) at α = 0.50 (starting system). Schematic test tubes visualize the state of the sample at different temperatures and surfactant mass fractions γ. **2**: coexistence of an oil-in-water microemulsion with an oil-excess phase; $\overline{\mathbf{2}}$: coexistence of water-in-oil microemulsion with a water-excess phase; **1**: one phase microemulsion; **3**: coexistence of microemulsion phase with water- and oil-excess phase. Taken from [143].

At low temperatures, an oil-in-water microemulsion coexists with an oil-excess phase (denoted as **2**), while at high temperatures a water-in-oil microemulsion coexists with a water-excess phase (denoted as $\overline{\mathbf{2}}$). At temperatures in between, either three phases, i.e. a microemulsion phase which coexists with a water- and an oil-excess phase (denoted as **3**), or a one-phase microemulsion can be observed. The pivotal point of these phase diagrams is the so-called $\tilde{X}$-point, which indicates the minimum surfactant mass fraction $\tilde{\gamma}$ that is needed to solubilize equal amounts of water and oil into each other at the phase inversion temperature $\tilde{T}$ (PIT). Note that the envisaged bicontinuous structure is formed near the PIT at $\gamma \geq \tilde{\gamma}$. The $\tilde{X}$-point of H_2O – cyclohexane – C_6E_5 system (at α = 0.50) is located at $\tilde{T}$ = 57.0 ± 0.5 °C and $\tilde{\gamma}$ = 0.285 ± 0.005.

Based on the system H_2O – cyclohexane–C_6E_5 (Figure 3.8) and with the goal to formulate a toluene microemulsion, 50 wt% of cyclohexane were replaced with toluene in a first step (Figure 3.9, a, □; parameter β defines the mass fraction of toluene with regard to the total mass of cyclohexane-toluene, i.e. β = 0.50). As can be seen, the one-phase region shifts to lower temperatures and lower surfactant mass fractions. This shift is related to the shrinkage of the lower miscibility gap of the binary oil – non-ionic surfactant system, which is induced by the partial replacement of cyclohexane with toluene. In order to compensate this

temperature shift, 40 wt% of the surfactant C_6E_5 was replaced with the hydrophilic sugar surfactant C_8G_1 (n-octyl β-D-glucopyranoside) (Figure 3.9, b, ■; the mass fraction of C_8G_1 in the surfactant mixture is denoted by the parameter δ, i.e. δ = 0.40). Due to the partial replacement of C_6E_5 with C_8G_1 the phase boundaries were shifted back to higher temperatures. The $\tilde{X}$-point of H_2O – cyclohexane/toluene – C_6E_5/C_8G_1 system (α = 0.50, β = 0.50, δ = 0.40) is located at $\tilde{T}$ = 47.7 ± 0.5 °C and $\tilde{\gamma}$ = 0.220 ± 0.005. Again, this shift of the phase boundaries can be related to the influence of the hydrophilic C_8G_1 on the upper and lower miscibility gap of the binary side systems water – surfactant and oil – surfactant, which both shift to higher temperatures. Thus, all cyclohexane can be replaced with toluene in the next step (Figure 3.9, b, △). The phase boundaries of the resulting H_2O – toluene – C_6E_5/C_8G_1 system (α = 0.50, β = 1.00, δ = 0.40) are located at lower temperatures exhibiting a $\tilde{X}$-point at $\tilde{T}$ = 29.0 ± 0.5 °C and $\tilde{\gamma}$ = 0.200 ± 0.005.

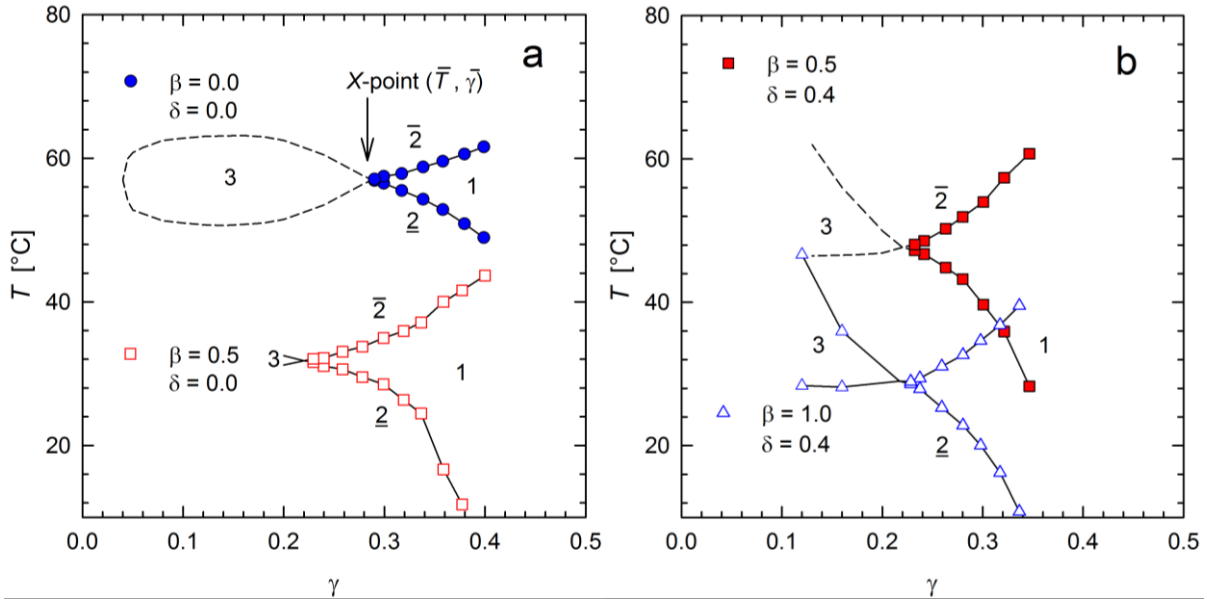

Figure 3.9: (a) $T(\gamma)$-sections of the systems H_2O – cyclohexane – C_6E_5 (●) (α = 0.50, β = 0.00) and H_2O – cyclohexane/toluene – C_6E_5 (□) (α = 0.50, β = 0.50). Replacing 50 wt% of cyclohexane with toluene shifts the phase boundaries and the $\tilde{X}$-point to lower temperatures and lower surfactant mass fractions. (b) $T(\gamma)$-sections of the systems H_2O – cyclohexane/toluene – C_6E_5/C_8G_1 (■) (α = 0.50, β = 0.50, δ = 0.40) and H_2O – toluene – C_6E_5/C_8G_1 (△) (α = 0.50, β = 1.00, δ = 0.40). Replacing 40 wt% of the surfactant C_6E_5 with the hydrophilic sugar surfactant C_8G_1 shifts the phase boundaries back to higher temperatures which allowed the replacment of the remaining cyclohexane with toluene. Taken from [143].

Envisaging a reaction temperature of $T \approx 60$ °C, the next step was to shift the one-phase region of the system H_2O – toluene – C_6E_5/C_8G_1 (△) (α = 0.50, β = 1.00, δ = 0.40) i.e. the region of the bicontinuous structure (close to the $\tilde{X}$-point), to much higher

temperatures. As the hydrophilic C_8G_1 surfactant allowed to shift the phase boundaries to higher temperatures, the mass fraction of C_8G_1 in the surfactant mixture was increased stepwise from $\delta = 0.40$ to 0.70 (Figure 3.10). The phase boundaries are shifted towards higher temperatures and in addition the one-phase region became wider, due to the weak temperature dependency of the surfactant head group hydration [144]. Furthermore, the $\tilde{X}$-point is shifted to a slightly higher surfactant mass fraction $\tilde{\gamma} = 0.245 \pm 0.005$ at $\tilde{T} = 55.8 \pm 0.5$ °C, which might be related to larger monomeric solubilities of the surfactants in water and toluene and that the amphiphilic film became less ordered (softer) with increasing temperature.

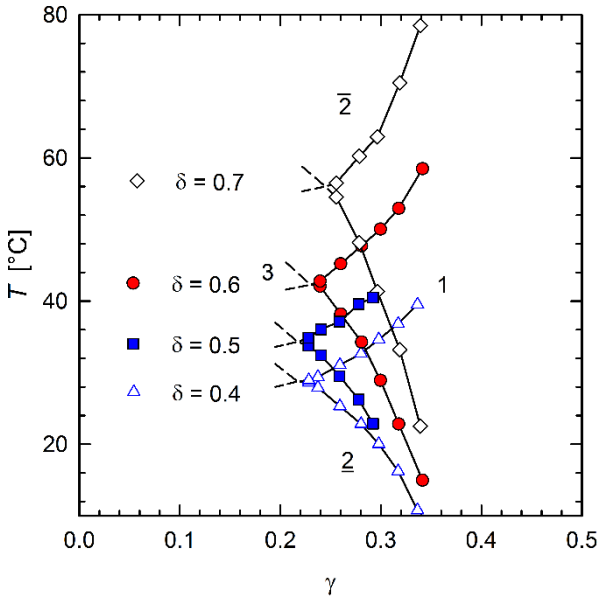

Figure 3.10: $T(\gamma)$-sections of the system H_2O – toluene – C_6E_5/C_8G_1 with different mass fraction δ of C_8G_1 in the surfactant mixture recorded at $\alpha = 0.50$. By increasing δ from 0.40 to 0.70 the one-phase region is widened and shifted towards higher temperatures with a small shift of $\tilde{\gamma}$ to higher surfactant mass fractions. Taken from [143].

Before this toluene-microemulsion H_2O – toluene – C_6E_5/C_8G_1 (Figure 3.10,◇ at $\delta = 0.70$) could be used as a reaction medium, the influence of KOH, the Rh-catalyst/ligands systems as well as the reactants on the phase behavior had to be examined. The influence of KOH and the Rh-catalyst with two different ligands **4a** and **5b** on the phase behavior of the H_2O – toluene – C_6E_5/C_8G_1 system ($\alpha = 0.50$, $\delta = 0.70$) is shown in Figure (3.11, a). It is apparent that a low KOH concentration (**x**) of $\varepsilon = 0.0033$ (the parameter ε is the mass fraction of KOH in the H_2O/KOH mixture), the Rh-catalyst/ligand **4a** (□) as well as Rh-catalyst/ligand **5b** (●) had no effect on the phase behavior of the system.

The effect of the reactant *N*-tosylimine **1** on the phase behavior of the formulated toluene microemulsion is shown in Figure (3.11, b, ■). *N*-tosylimine **1** shifted the phase boundaries to lower temperatures by approximately 15 K. This might be a consequence of a higher polarity of *N*-tosylimine **1** compared to toluene [145]. The same as *N*-tosylimine **1**, the influence of boroxine **2** on the phase behavior of the microemulsion was also studied.

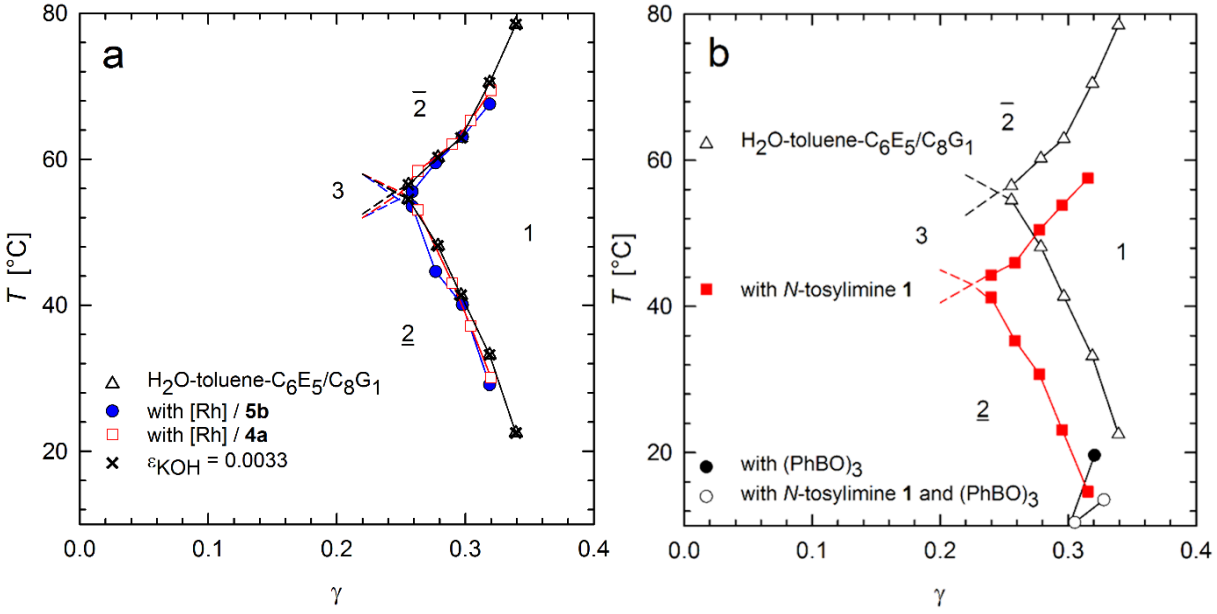

Figure 3.11: Influence of (a) KOH (ε = 0.0033), Rh-catalyst and ligands and (b) the reactants on the *T*(γ)-section of the base system H_2O – toluene – C_6E_5/C_8G_1 (δ = 0.70) (△) at α = 0.50 (a) and α = 0.52 (b). Due to the small concentrations, KOH (**x**), the Rh-catalyst with ligand **4a** (□) and ligand **5b** (●) had almost no influence on the phase boundaries of the base system. (b) On the contrary, the reactants *N*-tosylimine **1** (7.1 wt%) (■) and boroxine **2** (8.8 wt%) (●) in toluene at γ = 0.32 and α = 0.52 caused a strong shift the of phase boundaries to lower temperatures as well as the mixture of **1**/**2** (7.1 wt%/8.8 wt% in toluene at γ = 0.32 and α = 0.54) (○). Taken from [143].

As shown in Figure (3.11, b, ●), using a mixture of **2** and toluene instead of only toluene the phase boundaries were shifted strongly to lower temperatures. Thus, only the upper phase boundary could be measured. This strong effect of boroxine **2** on the phase behaviour might be related to the presumable formation of hydrolysis products e.g. boronic acid. The latter might act as hydrophobic co-surfactants and thus change the curvature of the amphiphilic film, i.e. phase behaviour of the microemulsion system. In order to prove this hypothesis, we measured the interfacial tension between water and toluene as a function of the boroxine concentration in toluene at T = 25 °C using the pendant drop method. The interfacial tension (σ) was found to decrease from 36 mNm^{-1} (value from [146]) to 12 mNm^{-1} with increasing boroxine concentration up to 2.0 wt%, which strongly indicates

the formation of amphiphilic hydrolysis products of boroxine **2**. The observed trends are more detailed discussed in appendix (Figure 5.2).

Since the Rh-catalyzed asymmetric 1,2-addition requires a toluene microemulsion which contains both reactants, we also investigated the influence of the *N*-tosylimine **1**/boroxine **2** mixture (7.1 wt%/8.8 wt% in toluene at $\gamma = 0.32$) on the phase behavior of the microemulsion (Figure 3.11, b, ○). As expected, from the trends found for the microemulsions containing only one reactant, the phase boundaries are shifted to even lower temperatures in the presence of the mixture of **1** and **2**.

Aiming for a bicontinuously structured microemulsion containing KOH, the Rh-catalyst/ligands as well as the two reactants at $T \approx 60°C$, the phase boundaries had to be shifted back to higher temperatures. Interestingly, replacing the remaining C_6E_5 surfactant with C_8G_1, the strong shift of the phase boundaries to lower temperatures caused by **2** and **1** was compensated. Figure 3.12 shows the phase behavior of the reaction microemulsion system H_2O/KOH – toluene/*N*-tosylimine **1**/boroxine **2** – C_8G_1 with $\alpha = 0.54$, $\varepsilon_{KOH} = 0.0033$, **1** (7.1 wt%) and **2** (8.8 wt%). The $\tilde{X}$-point of the reaction microemulsion is located at $\tilde{T} = 48.4 \pm 0.5$ °C and $\tilde{\gamma} = 0.19 \pm 0.005$. The system has a one-phase region between 20 °C to 80 °C at $\gamma = 0.26$, which is suitable for the Rh-catalyzed asymmetric 1,2-addition. The steep lower phase boundary is a consequence of the weak temperature dependency of the amphiphilic film curvature. With increasing temperature, the hydration of the hydroxyl groups decreases while the toluene and reactants molecules have a stronger tendency to penetrate the alkyl chains of the amphiphilic film. However, as both hydration and penetration are only weakly temperature dependent, the reaction microemulsion might be less sensitive to composition changes generated by the Rh-catalyzed asymmetric 1,2-addition.

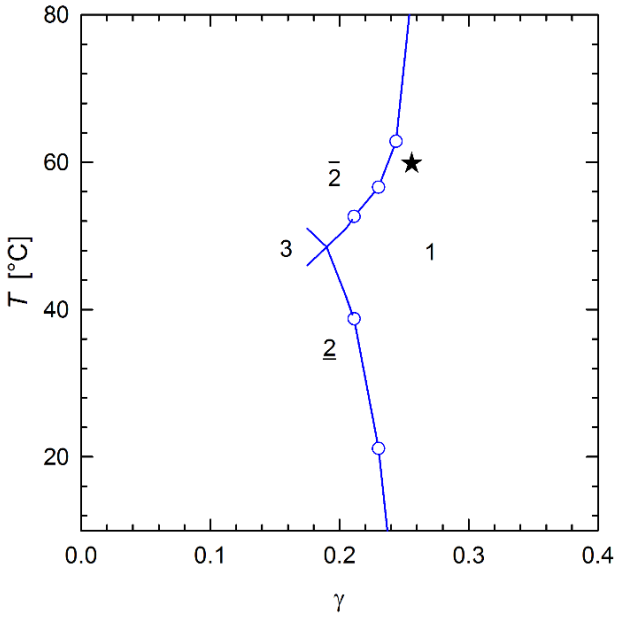

Figure 3.12: *T*(γ)-section of the system H_2O/KOH – toluene/*N*-tosylimine **1**/boroxine **2** – C_8G_1 at α = 0.54, ε_{KOH} = 0.0033, **1** (7.1 wt%) and **2** (8.8 wt%) in toluene at γ = 0.30. Due to the weak temperature dependency of the C_8G_1 surfactant, a wide one-phase region can be observed. The compositio of the microemulsion used for the Rh-catalyzed asymmetric 1,2-addition at γ = 0.26 and *T* = 60 °C is indicated by the star. Taken from [143].

3.2.2. Structural Characterization by Small Angle X-ray Scattering (SAXS)

In order to determine the size of the water and toluene/reactant domains of the microemulsion, SAXS experiment was performed at $\gamma = 0.26$ and $T = 60$ °C. Figure 3.13 displays the scattering curve of the scattering intensity as a function of the scattering vector q. The scattering curves exhibit the typical shape found for bicontinuous microemulsions [147]: Starting from low q-values, the scattering intensity slightly increases, runs through a maximum at middle q-values before the intensity decreases with q^{-3} rather than q^{-4}. Note that this finding can be explained by the combination of film and bulk contrast contributions.

By using the Teubner-Strey model [147]: a correlation length of $\xi_{TS} = 3.3 \pm 0.2$ nm and a size of $d_{TS}/2 = 5.5 \pm 0.2$ nm was obtained for the water and toluene/reactant domains. Considering that the concentration of the catalyst/ligand complex with respect to reactant **1** is 2.5 mol%, on average every second toluene domain contains a catalyst/ligand complex.

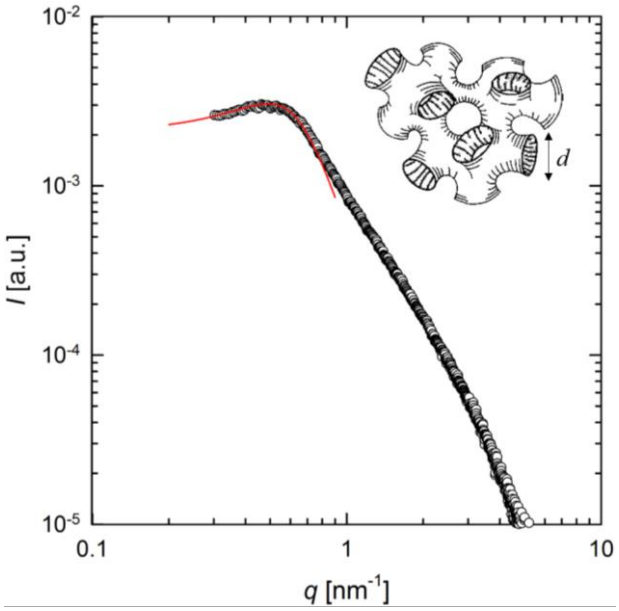

Figure 3.13: SAXS scattering curve (black) of the bicontinuous microemulsion of H_2O/KOH – toluene/*N*-tosylimine **1**/boroxine **2** – C_8G_1 system at $\gamma = 0.26$, $\alpha = 0.54$, $\varepsilon_{KOH} = 0.0033$, **1** (7.1 wt%) and **2** (8.8 wt%) in toluene at $\gamma = 0.30$ and $T = 60.0$ °C. The red solid line is the fit of the scattering peak using the Teubner-Strey model [147]. Taken from [143].

3.2.3. Influence of the Reaction Progress on the Phase Behavior

When the Rh-catalyzed asymmetric 1,2-addition was conducted in the H_2O/KOH – toluene/*N*-tosylimine **1**/boroxine **2** – C_8G_1 microemulsion at T = 60 °C, it was observed that the reaction medium changed from the one-phase bicontinuous microemulsion to the 2-phase state, where an oil-in-water microemulsion coexists with an oil-excess phase, i.e. $\underline{2}$. In order to understand this observation, the influence of the changing reactant/product ratio on the phase behaviour of the toluene microemulsion was studied. As can be seen in Figure 3.14, replacing the two reactants **1** and **2** with the product **3** ($\chi_{reactants}$ denotes the mass fraction reactant **1** and **2** in the mixture of the reactants (**1** and **2**) and product **3**), the lower phase boundary indeed is shifted to higher temperatures. Note that at the reaction temperature (60 °C), after a conversion of 50 wt% of the reactants **1** and **2** to product **3**, the microemulsion transfers from the one-phase to $\underline{2}$ phase state. However, one must keep in mind that the reaction medium contains not only the secondary amine **3** but also byproducts, which influences the phase behavior of the microemulsion as well. This shift of the lower phase boundary by the product **3** is most probably related to both the increasing amount of amine **3**, which is more hydrophobic than *N*-tosylimine **1** and the decreasing amount of boroxine **2** which corresponds to a decreasing amount of its amphiphilic hydrolysis products that act as hydrophobic co-surfactants.

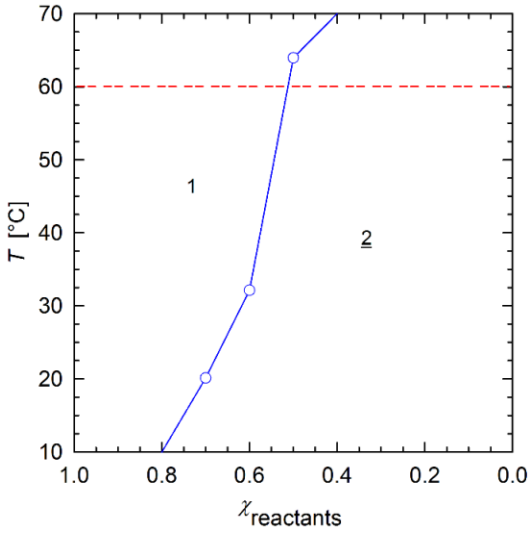

Figure 3.14: Influence of the reactant (1 and 2)/product 3 ratio $\chi_{reactants}$ on the lower phase boundary of the system H_2O/KOH - toluene/**1** and **2**/**3** - C_8G_1 at $\alpha = 0.54$, $\varepsilon_{KOH} = 0.0033$ and $\gamma = 0.26$. The nonpolar component containing toluene/reactant (**1** and **2**) (84.1 wt%/ 7.1 wt%/8.8 wt%) was replaced stepwise with the toluene/ amine **3** mixture (15.9 wt%). $\chi_{reactants}$ denotes the mass fraction of **1** and **2** in the mixture of reactants (**1** and **2**) and product **3**. The red line at 60 °C shows the reaction temperature, at which, after a conversion of 50 wt% of the reactants **1** and **2** to product **3**, the microemulsion transfers from the one-phase to two-phase state. Taken from [143].

3.2.4. Rh-catalyzed Asymmetric 1,2-Additions

After having the balanced microemulsion of water and toluene containing both reactants, KOH and catalyst/ligands complex for the Rh-catalyzed asymmetric 1,2-additon of boroxine **2** to *N*-tosylimine **1**. The aim now is to investigate the influence of the nanostructure liquid confined geometries as a reaction media on the catalysis using the different Rh/ligands systems and compare the results with the homogeneous condition (pure dioxane and pure toluene). Sine the ligands exhibiting different polarities, namely, ligands 4 are relatively nonpolar compared to ligands 5 and 6, the discussion will consider firstly the Rh/ligands 4 and then the Rh/Ligands 5, 6.

i. 1,2-addition catalyzed by Rh/Ligands 4

The application of relatively nonpolar "chiral bicyclo[3.3.0]octadienes" **4** as ligands in Rh-catalyzed asymmetric 1,2-additions of triphenylboroxine **2** to (4-chlorophenyl)-*N*-tosylimine **1** was studied under homogeneous conditions (dioxane and toluene) and in liquid confined spaces (bicontinuous microemulsion) (Table 3.1).

Table 3.1: Comparison of 1,2-additions of boroxine **2** to *N*-tosylimine **1** in conventional solvents and in the microemulsion (ME) catalyzed by a complex of Rh/ligand **4**. The progress of the reactions was monitored by ^{1}H-NMR spectroscopy. Taken from [143].

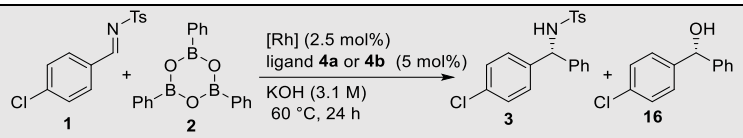

entry	ligand	medium	NMR yield [%]			isolated yield [%]		*ee* [%]*	
			1	**3**	**16**	**3**	**16**	**3**	**16**
1	**4a**	dioxane	–	>99	–	>99	–	>99	–
2	**4a**	toluene	–	90	10	82	9	99	10
3	**4b**	dioxane	–	98	2	97	–	97	–
4	**4a**	ME	2	96	2	93	–	>99	–
5	**4b**	ME	1	95	4	95	–	97	–

*_ee_: enantiomeric excess. (100 % means high enantioselectivity)

Under the reaction conditions given in Table 3.1, the quantitative conversion of *N*-tosylimine **1** and boroxine **2** with Rh/ligand **4a** in dioxane yielded enantiomerically pure product **3** in 99% with >99% *ee* (Entry 1). For comparison with toluene-based microemulsions, the homogeneous catalysis was also performed in toluene [148]. ^{1}H-NMR analysis of the crude product revealed a (90:10) mixture of product **3** and alcohol **16**, which after chromatography purification gives **3** in 82% with high enantioselectivity (99% *ee*) and 9% of **16** (10% *ee*) (Entry 2). Performing the 1,2-addition reaction with ligand **4b** (R = OH) also proceeded cleanly in dioxane (Entry 3).

However, performing the 1,2-addition with catalyst Rh/**4a** in the formulated toluene-based microemulsion (composition assigned by the star on Figure 3.12) under same conditions leads to a crude product mixture (2:96:2) of starting material **1**, product **3** and alcohol **16**, respectively. From which product **3** was subsequently isolated in high yield and enantiomeric excess (93%, >99% *ee*) (Entry 4). Thus, in comparison to the homogeneous catalysis in toluene (Entry 2), the chemoselectivity, i.e. the ratio of amine **3** vs. alcohol **16**, was shifted in favor of **3** and the isolated yield was improved. In the microemulsion, the

asymmetric 1,2-additon in the presence of Rh/**4b** provided a result analogue to **4a** however with slightly lower yields and the same *ee* values (Entry 5).

ii. 1,2-addition catalyzed by Rh/Ligands 5 and 6

Here, the catalytic properties of more polar, less symmetric, and chiral "oxazolidinone norbornadienes" **5** and **6** as ligands in both the confined system, i.e. the toluene-based microemulsion, and in the conventional solvents (toluene and dioxane) were investigated (Table 3.2).

Under the given reaction conditions, ^{1}H-NMR analysis showed that the asymmetric 1,2-additon in dioxane and in the presence of the diene **5b,5b'** (d.r. 98:2) as ligand yielded a crude mixture (10:89:1) of **1**:**3**:**17**. In contrast, the reaction in toluene was significantly retarded, which results in a crude mixture that was dominated by the starting material tosylimine **1** (67%) (Entries 1, 2). However, using the single diastereomer **5b** in dioxane led to amine **3** in only 61% yield but with 90% *ee* (*R*) (Entry 3). The single diastereomers **5d** and **5d'** with the 4-chlorophenyl substituent were studied in parallel experiments in dioxane (Entries 4, 5). In both cases, incomplete conversion and large amounts of aldehyde **17** were detected. Accordingly, only low yields of product **3** (20% with ligand **5d** and 32% with ligand **5d'**) were obtained. Whereas a ligand-controlled enantioselectivity was observed with diastereomer **5d** producing (94% *ee* (*R*)) (Entry 4), while diastereomer **5d'** was less enantioselective leading to (56% *ee* (*S*)) with opposite configuration of the major enantiomer of **3** (Entry 5). In case of ligands **6**, incomplete conversions in conventional solution were monitored by ^{1}H-NMR for all dienes **6** irrespective of their diastereomeric ratios and the substituents. Amine **3** was isolated in moderate yields (48–73%) but high enantiomeric excesses of 92–98% *ee* (*R*) with exception of ligand mixture **6a**,**6a'** (74% *ee* (*R*)) (Entries 6-8).

On the other hand, the 1,2-additions of boroxine **2** to tosylimine **1** in confinement in the presence of in situ generated catalyst from $[Rh(C_2H_4)_2Cl]_2$ and more polar chiral ligands **5** and **6**, clearly differed from those in conventional solvents. The catalysis in the toluene-based microemulsion went to completion with amine **3** as the major product. No starting material **1** was detectable in the crude product but small amounts of byproduct **17** (Table 3.2).

In the microemulsion (composition assigned by the star on Figure 3.12), the use phenyl Evans diene ligand **5b,5b'** (dr 98:2) provided amine **3** in 61% yield with considerably enhanced enantioselectivity (90% *ee* (*R*)) compared to the reaction in dioxane (Entries 1, 9). Using single diastereomer **5b** the isolated yield of **3** was further improved to 84%, while the enantioselectivity was markedly decreased to 22% *ee* (Entry 10). The beneficial influence of the microemulsion on the Rh-catalyzed 1,2-addition was most prominently revealed for the diastereomeric pure 4-chlorophenyl Evans diene **5d**, which strongly favored the formation of amine **3** (97% crude, 79% isolated, 92% *ee* (*R*)) with high enantioselectivity (Entry 11). The diastereomeric pure ligand **5d'** also led to product **3** in much higher yield than in the conventional dioxane solution, though, with less enantiocontrol (59% isolated, 12% *ee* (*R*)) (Entry 12). As compared to the catalysis in the conventional solvent dioxane, the diene **6a**,**6a'**, **6b** and **6c**,**6c'** ligands, respectively, led to increase the yield of product **3** in the microemulsion and maintain the enantioselectivities (Entries 13–15). The more pronounced yield enhancement found for Evans diene **5b** in microemulsion vs. dioxane (Entries 3, 10) as compared to diene **6b** (Entries 7, 14) might be due to different confined environment offered by the toluene-based microemulsion. However, based on the current results it is too early to draw further mechanistic conclusion.

Table 3.2: Comparison of 1,2-addition reactions in conventional solvents and microemulsion (ME) catalyzed by a complex of Rh/ligand **5** and **6**, respectively. The reaction progress was monitored by ^{1}H-NMR spectroscopy. Taken from [143].

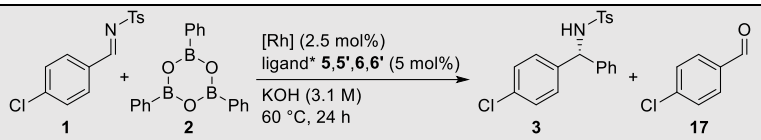

entry	ligand	dr[a]	medium	NMR yield [%]			isolated yield [%]	*ee* [%]
				1	**3**	**17**	**3**	**3**
1	5b,5b'	98:2	dioxane	10	89	1	69	32 (*R*)
2	5b,5b'	98:2	toluene	67	14	13	n.d.	n.d.
3	5b	100:0	dioxane	18	76	6	61	90 (*R*)
4	5d	100:0	dioxane	55	25	20	20	94 (*R*)
5	5d'	0:100	dioxane	15	32	53	32	56 (*S*)
6	6a,6a'	72:28	dioxane	11	68	20	48	74 (*R*)
7	6b	100:0	dioxane	27	55	18	55	98 (*R*)
8	6c,6c'	68:32	dioxane	18	60	22	61	92 (*R*)
9	5b,5b'	98:2	ME [b]	–	83	17	61	90 (*R*)
10	5b	100:0	ME [c]	–	93	7	84	22 (*R*)
11	5d	100:0	ME [c]	–	97	3	79	92 (*R*)
12	5d'	0:100	ME [c]	–	83	17	59	12 (R)
13	6a,6a'	72:28	ME [b]	–	88	12	75	70 (*R*)
14	6b	100:0	ME [b]	–	77	23	65	96 (*R*)
15	6c,6c'	68:32	ME [b]	–	84	16	77	90 (*R*)

[a] dr: diastereomeric ratio [b] ME: 0.60 g C_8G_1, 0.89 mL toluene, 0.77 mL H_2O at $\gamma = 0.26$ and $\alpha = 0.54$. [c] ME: 0.60 g C_8G_1, 0.81 mL toluene, 0.70 mL H_2O at $\gamma = 0.28$ and $\alpha = 0.54$.

3.2.5. Kinetic Studies of Rh-catalyzed Asymmetric 1,2-Additions

It was noticed while performing the Rh-catalyzed asymmetric 1,2-additions in the microemulsion regardless of the ligand, that the microemulsion became turbid within few minutes after the reaction started. This indicates a change in the composition of the microemulsion. However, this quick change was not expected, since in the literature a reaction time between 6 – 24 h were reported [121,123]. Therefore, the kinetics of Rh-catalyzed asymmetric 1,2-additions using the ligand **4a** and **5b** in different reaction media was investigated.

The kinetics of the Rh-catalyzed arylation of *N*-tosylimine **1** with boroxine **2** was monitored by ^{1}H-NMR. Figure 3.15 shows the yield obtained at T = 60 °C in the different reaction media, i.e. dioxane, toluene and the microemulsion as a function of time. While in the reaction profiles shown in Figure (3.15, a) the Rh/ligand **4a** was used, the Rh/ligand **5b** was applied in the profiles of Figure (3.15, b). Considering first the reaction profiles for the Rh/ligand **4a** system, an almost complete conversion was detected at t = 4 min in both dioxane (>99%) and the microemulsion (>96%). However, the reaction profile in toluene shows similar kinetics but a yield of 90 % was found after 4 minutes which remained constant for 24 hours. A first order kinetics with respect to *N*-tosylimine **1** was observed in all experiments. Accordingly, the kinetic data were described by a mono-exponential fit obtained via integration of the first order rate equation

$$d[product\ \mathbf{3}]/dt = k_{\mathrm{app}}[N\text{-tosylimine}\ \mathbf{1}]$$

yielding the reciprocal rate constant $\tau = k_{\mathrm{app}}^{-1}$, where is the apparent rate constant. Thereby, estimating the systematic error with respect to the time to be of the order of 20 s ($\Delta t_{\mathrm{start}} \approx 7$ s: time needed to obtain a homogeneous distribution after the addition of the reactant molecules; $\Delta t_{\mathrm{end}} \approx 13$ s: time needed to remove the Rh/ligand complex by filtration to stop the reaction). The values of τ (together with the standard deviation for $\tau > 1$ min) and the maximum yield obtained for reactions with the Rh/ligand **4a** and ligand **5b** complexes in the different reaction media are listed in Table 3.3.

Using the Rh/ligand **4a** system, the 1,2-addition proceeded fast in the three reaction media. Although a systematic trend in the initial rate might be deducible from the first data point, the value of the reciprocal rate constant τ only qualitatively was estimated due to the systematic time error of the order of 20 s and the fact that only one data point (yield after

two minutes) could be recorded between the start of the reaction and complete conversion. Therefore, the reciprocal rate constant was indicated to be smaller than 1 min for the three reaction media.

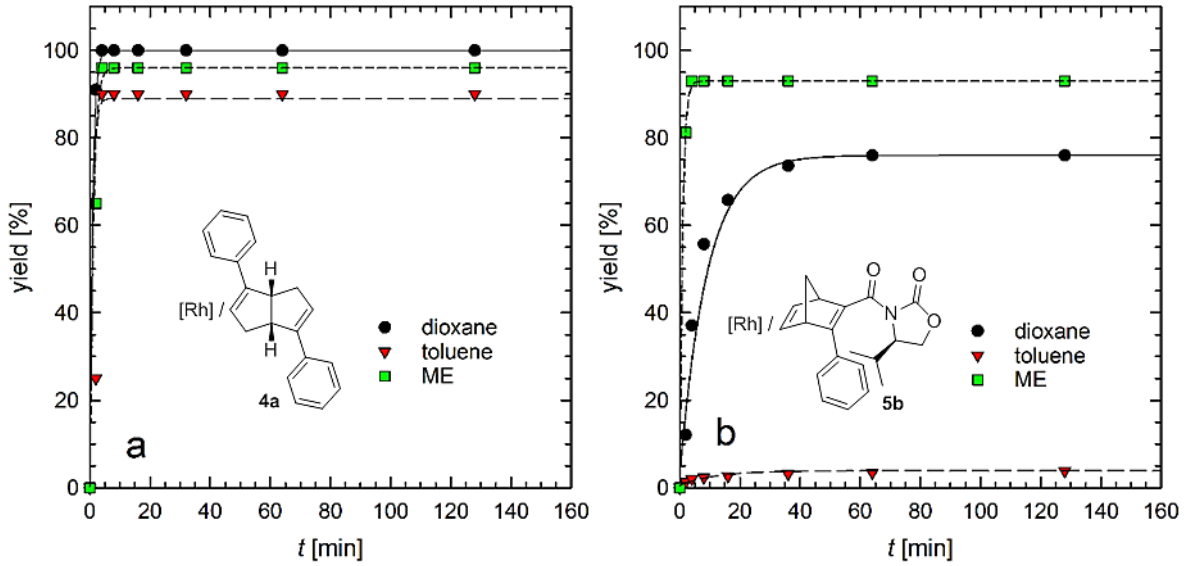

Figure 3.15: Yield of the Rh-catalyzed 1,2-addition of boroxine **2** to *N*-tosylimine **1** performed at T = 60 °C as a function of time using different reaction media. The kinetics obtained for the Rh/ligand **4a** (a) proceeded so fast in all reaction media, that only one data point could be recorded between the start of the reaction and complete conversion (τ < 1 min). In contrast, for the Rh/ligand **5b** (b) the microemulsion provides not only a higher conversion, but also almost one order of magnitude faster reaction rate than dioxane. The data were described by a mono-exponential fit which gives τ (together with the standard deviation) and the maximum yield (Table 3.3). Taken from [143].

Table 3.3: Reciprocal rate constant and maximum yield of the Rh-catalyzed 1,2-addition of boroxine **2** to *N*-tosylimine **1** at 60 °C in different reaction media and two different Rh/ligand systems (**4a** and **5b**). Taken from [143].

entry	medium	ligand	τ [min]	NMR yield [%]
1	dioxane	**4a**	< 1.0	>99
2	toluene	**4a**	< 1.0	90
3	ME	**4a**	< 1.0	96
4	dioxane	**5b**	9.1 ± 0.7	76
5	toluene	**5b**	11.9 ± 3.0	4
6	ME	**5b**	< 1.0	93

However, using the Rh/ligand **5b** in the microemulsion a yield of 93 % was reached after 8 minutes, whereas in dioxane a maximum yield of only 76 % was detected after 128 minutes which remained constant. In toluene, only a maximum yield of just 4 % was observed after 24 hours. The increase of the reciprocal rate constant (Table 3.3), unambiguously showed that the microemulsion reaction medium provided not only an almost complete conversion, but also an almost one order of magnitude faster reaction rate than dioxane.

In the next step, the influence of the temperature on the kinetics of the Rh/ligand **4a**-catalyzed 1,2-addition of **2** to *N*-tosylimine **1** was studied using dioxane and the microemulsion as reaction media.

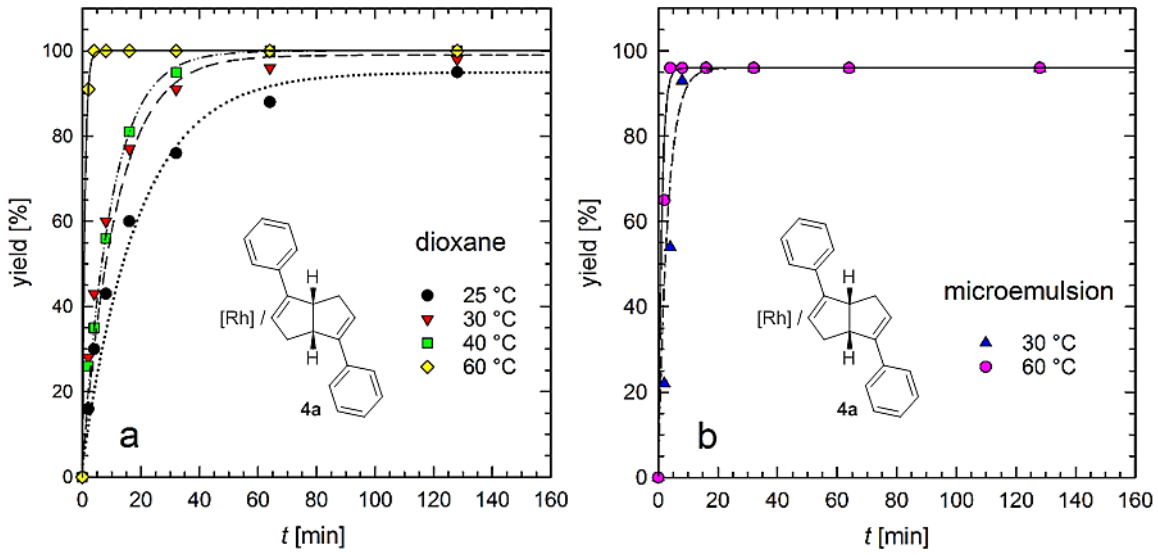

Figure 3.16: Yield of the 1,2-addition of **2** to *N*-tosylimine **1** in the presence of chiral ligand **4a** as a function of time at different temperatures. (a) In dioxane the reaction proceeded slow at low temperatures. (b) In the microemulsion fast kinetics were also observed at T = 30 °C, which were a factor 4 faster than in dioxane at the same temperature. The data were described by a mono-exponential fit providing the reciprocal rate constant τ and the maximum yield (Table 3.4). Taken from [143].

Figure (3.16, a) shows that the kinetics of the addition exhibits a strong temperature dependence if conducted in dioxane. The reciprocal rate constant τ was found to decrease from $\tau \approx 11.9$ min at 30 °C (the maximum yield of 98% was reached only after 128 min) to $\tau < 1$ min at 60 °C, which shows that the reaction proceeds slowly at low temperatures. On contrary, the reaction profiles for 1,2-addition in the microemulsion (Figure 7b) demonstrate that the Rh-catalyzed addition reaction proceeds fast even at T = 30°C, in the

microemulsion such that a complete conversion was detected at t = 16 min. The reciprocal rate constant τ and the maximum yield of the reaction profiles are compiled in Table 3.4.

Table 3.4: Reciprocal rate constants and maximum yield of the Rh/4a-catalyzed addition of boroxine **2** to *N*-tosylimine **1** at different temperatures in dioxane and the microemulsion. Taken from [143].

entry	medium	T [°C]	τ [min]	NMR yield [%]
1	dioxane	25	19.2 ± 1.3	95
2	dioxane	30	11.8 ± 1.4	>99
3	dioxane	40	9.8 ± 0.3	>99
4	dioxane	60	< 1.0	>99
5	ME	30	3.1 ± 0.6	96
6	ME	60	< 1.0	96

4 Conclusions and Outlook

Catalysis is not only about the chemistry of catalysts but also about the nanoenvironments in which catalysis takes place, which makes catalysis to an interdisciplinary field enveloping concepts and contributions from all areas of chemistry. In that light, to answer the challenges facing this field they might to be viewed from another perspective. For instance, there is a rising interest in heterogenizing the homogeneous organometallic catalysts, to reduce their economical and environmental impact. Moreover, to transfer the concept of biocatalysis to molecular heterogeneous catalysis new mesoporous supports are needed whose catalysts are anchored inside the pores via linker groups. Therefore, this thesis focused on the synthesis of open-cellular porous polystyrene and mesoporous PS/ZnO hybrid materials, on the one hand, and on probing the effect of bicontinuously nanostructured microemulsions on the homogeneous organometallic catalysis, on the other hand.

Porous Polymers. The main goal of this part was to synthesize porous polymers with a pore size $50 < d_{pore}/nm < 250$ and open-cellular morphology following the NF-CID method, which combined the template concept with $scCO_2$ foaming. A high number density of CO_2 nanodroplets (10^{16} cm^{-3}) in the polymer matrix is obtained starting from colloidal crystals of polymer nanoparticles with a particle diameter below 100 nm. Thus, the diameter and polydispersity of the nanoparticles synthesized via emulsion polymerization as well as the packing density of the colloidal crystals were expected to have a considerable influence on the pore size and morphology of the porous polymers. These investigations showed that foaming colloidal crystals of relatively polydisperse PS nanoparticle ($d_{particle} < 50$ nm) with a packing density of $Ø \geq 78$ % led to porous polymers with unimodal morphology and pore sizes smaller than 1 μm.

In next step, the influence of NF-CID parameters (temperature and exposure time) was studied based on the optimal colloidal crystals of PS nanoparticles with $d_{particle} = 48 \pm 6$ nm and a packing density of $Ø \geq 78$ %. Investigating the influence of the temperature, it was found that a temperature of 45 °C is needed to induce the inversion step leading to a porous polymer with pore size of $d_{pore} = 274 \pm 62$ nm, while the experiments performed at higher temperatures e,g, 55 °C, 65 °C, and 75 °C clearly indicated that the obtained porous polymers suffer from coarsening due to Ostwald ripening and coagulation and coalescence.

Varying the exposure time between 15 and 60 min, it could clearly be shown that coarsening of the CO_2 droplets occurs during the so-called continuity-inversion step of the NF-CID method and results in pores larger than 1 μm.

In order to decrease the pore size and to produce open-cellular porous polymers, the expansion step of the NF-CID method has been modified. By conducting the inversion and expansion step at different temperatures, a porous polymer with open-cellular morphology and pore size ≈ 50 nm could be obtained.

Porous Organic/Inorganic Hybrid Materials. With the overall goal to use the open-cellular porous polymers as supports for catalysis, a higher stability against harsh organic solvents and high temperatures is desirable. To overcome this weakness the chemical deposition bath (CBD) method was used to form a metal oxide layer on the pore wall. Mineralizing the closed-cellular porous polystyrene with a relatively large pore diameter of d_{pore} = 1.21 ± 0.28 μm with ZnO as a proof of principle led to the formation of a ZnO layer of 50 nm on the pore walls, while the morphology of the initial porous polystyrene is preserved.

However, the result of the mineralization of the open-cellular porous polystyrene with a pore size of 50 nm with ZnO demonstrated that only single ZnO particles or clusters of ZnO particles were formed on the inner surface and the most of the formed ZnO particles were rather deposited on the outer surface rather than on the inner surface. The findings might be related to the mineralization process and conditions, which might depend on the size of the confinement. Furthermore, the hindered diffusion of the mineralization solution into the open-cellular porous polymers might be an issue. Finally, the pore walls generated by the modified NF-CID process might not be fully covered with SDS molecules and thus not enabling the formation of ZnO film due to the lack of charges.

Therefore, investigating the influence of the confinement on the mineralization process, the influence of the diffusion in nanopore and the composition of the outer and inner surface could eliminate those issues and would lead to porous organic/inorganic hybrid materials with pore size below 50 nm.

Liquid Confinement and Rh-catalyzed Aysmmetric 1,2 Addition. The aim of this part of the thesis was to investigate the effect of the liquid confinement in bicontinuously structured microemulsions on the asymmetric Rh-catalyzed 1,2-additions of boroxine **2** to

N-tosylimine **1**. Since it was expected that this effect depends on the location of the catalyst within the microemulsion, i.e. the amphiphilic film, the organic or water domains. Catalysts with several ligands exhibiting different polarities were examined. Two series of novel chiral diene ligands were chosen; the relatively nonpolar, symmetric ligands **4a** and **4b,** as well as, the polar, less symmetric ligands **5a**-**d**, and **6a**–**d**.

Using the formulated microemulsion as a reaction medium provides not only liquid confinement but also mediated the miscibility between polar and nonpolar components. The aqueous domains of the microemulsion are a suitable environment for KOH which is needed to activate the Rh-complex. The hydrophobic reactants *N*-tosylimine **1** and boroxine **2** are rather solubilized in the toluene domains, while the Rh/ligand complex can reside in/at the amphiphilic film or in the toluene domains depends on the polarity of the corresponding ligand. Assuming that the bicontinuous structure of the microemulsion facilitates the access of the Rh/ligand system with respect to both KOH and the reactants, a balanced microemulsion containing equal amounts of water and toluene was formulated. Starting from the well-known microemulsion of the type H_2O – cyclohexane – C_6E_5, cyclohexane was replaced with the more polar toluene. This replacement led to a shift of the phase boundaries to lower temperature, in order to compensate it the surfactant C_6E_5 was partially replaced by the hydrophilic surfactant *n*-octyl β-D-glucopyranoside C_8G_1.

Having a microemulsion of H_2O – toluene – C_6E_5/C_8G_1, the influence of KOH, the catalyst and ligands as well as the reactants on the phase behavior was studied. While the presence of the Rh/diene ligand catalysts as well as KOH (low concentration) had almost no influence on the phase boundaries, *N*-tosylimine **1** and particularly boroxine **2** caused a strong shift of the phase boundaries to low temperatures. This effect was compensated by replacing the remaining surfactant C_6E_5 with the hydrophilic C_8G_1, which gave the reaction microemulsion H_2O/KOH – toluene/*N*-tosylimine **1**/boroxine **2** – C_8G_1. The characteristic length scale of the liquid confinement was determined via SAXS, revealing a domain size of the aqueous and toluene/*N*-tosylimine **1**/boroxine **2** compartments of 55 Å. Considering that the concentration of the catalyst with respect to reactant **1** is 2.5 mol%, on average every second toluene domain contains a catalyst.

Performing the Rh-catalyzed 1,2-addition of boroxine **2** to *N*-tosylimine **1** in toluene, dioxane and the microemulsion using different ligands of different polarity, it was found that the catalysis was strongly dependent on both the ligand type and the reaction medium.

For the relatively nonpolar ligands **4** good yields (up to 87 %) and good enantioselectivities (>95 % *ee*) of product **3** were obtained irrespective of the reaction medium (microemulsion vs dioxane or toluene). On contrary, applying more polar ligands **5**, **6,** the catalytic reactions were sluggish in dioxane and almost dead in toluene. Yields and *ee* values showed significate differences depending on the substitution on the ligands **5**, **6**. Performing the reactions in microemulsions, yields (up to 97 %) and enantioselectivities (up to 96 % *ee*) were enhanced in most cases compared to that in dioxane. The most pronounced effect of the microemulsions was found for diastereomeric pure ligands **5d**, **5d'**, which led to improved yields and different selectivities. While the results for **5d** were similar for microemulsions and dioxane (92 % *ee* (*R*) and 94 % *ee* (*R*) for **5d**), the **5d'** gave opposite configurations in microemulsions and dioxane (12 % *ee* (*R*) and 56 % *ee* (*S*) for **5d'**).

The observed yield improvement of the catalytic reaction in the microemulsion, in particular for ligand **5b** which is less active in dioxane solution as compared to ligands **4** was also confirmed by kinetic investigations, which showed that at T = 60 °C the reaction rate in the microemulsion is almost one order of magnitude faster than in dioxane and more than one order of magnitude faster than in toluene, where the latter yielded only 4%. Furthermore, performing the 1,2-addition with Rh/ligand **4a** catalyst at T = 30 °C, the reaction in the microemulsion was even 4 times faster than in dioxane.

The results showed that the liquid confinement provided by bicontinuous microemulsions can improve both reaction rate and enantioselectivity for the 1,2-addition of boroxine **2** to *N*-tosylimine **1** catalyzed by chiral Rh-diene complexes, mainly in case of slightly polar ligands.

5 Appendix

5.1. Nomenclature

Abbreviation

IUPAC	International Union of Pure and Applied Chemistry
SDS	sodium dodecyl sulfate
PS	polystyrene
ZnO	zinc oxide
CBD	chemical bath deposition
Rh	rhodium
SAXS	small angle X-ray scattering
SEM	scanning electron microscopy
DLS	dynamic light scattering
N-tosylimine **1**	*(E)*-*N*-(4-chloro-benzylidene)-4-methylbenzenesulfonamide
Boroxine **2**	triphenylboroxine
PMMA	poly(methyl methacrylate)
MMA	methyl methacrylate
BCs	block copolymers
KPS	potassium peroxodisulfate
CMC	critical micelle concentration
GPC	gel permeation chromatography
DSC	differential scanning calorimetry
TEAOH	tetraethylammonium hydroxide
PVP	polyvinylpyrrolidone
EO	ethylene oxide
KOH	potassium hydroxide
$C_{10}E_8$	octaethylene glycol monodecyl ether
C_6E_5	pentaethylene glycol monohexyl ether
C_8G_1	n-octyl β-D-glucopyranoside

Parameters

Λ	mean fee path
ΔG	free energy
r	radius of gas cell
r^*	critical radius
Δp	pressure difference
N_0	nucleation rate
η	viscosity
σ	interfacial tension
d_{pore}	pore size/diameter
d_{pred}	predicted pore size using equation (8)
d_{particel}	particle diameter
d_{H}	hydrodynamic diameter
PDI	polydispersity
f_{A}	volume fraction
T_{g}	glass transition temperature
T_{g}^*	glass transition temperature of polymer saturated with CO_2
T_{c}	critical temperature
p_{c}	critical pressure
ϕ	volume fraction
$\emptyset$	packing density
$\rho_{\text{scfluid,l}}$	density of the sc-fluid at high pressure
$\rho_{\text{scfluid,g}}$	density of the sc-fluid at low pressure
N_{particle}	number of particles
N_{scfluid}	number of spherical sc-fluid nanodroplets
sc	supercritical
t_{exp}	exposure time
k_{p}	propagation rate constant
N_{T}	number of mature particles
$[\text{M}_{\text{p}}]$	monomer concentration within the mature particle
a_{s}	interfacial area occupied by a surfactant

ee	Enantiomeric excess
dr	diastereomeric ratio
p_w	rate of radical generation
$\overline{M}_n$	number average molecular weight
BET	Brunauer-Emmett-Teller method
E	elastic modulus
τ	reciprocal rate constant
k_{app}^{-1}	apparent rate constant
cp_α	upper critical point
cp_β	lower critical point
$\overline{\mathbf{2}}$	index of a water-in-oil microemulsion with water excess phase
$\underline{\mathbf{2}}$	index of an oil-in-water microemulsion with oil excess phase
α	oil mass fraction
β	mass fraction of toluene in cyclohexane-toluene mixture
δ	mass fraction of C_8G_1 in the surfactant mixture
m_B	mass of oil
m_A	mass of water
m_C	mass of surfactant
γ	surfactant mass fraction
$\widetilde{X}$	efficiency point at a particular α
$\widetilde{T}$	temperature at $\widetilde{X}$-point
$\tilde{\gamma}$	surfactant mass fraction at $\widetilde{X}$-point
PIT	phase inversion temperature
c_1	principal curvature
R_1	principal curvature radius
H	mean curvature
w/o	water-in-oil
o/w	oil-in-water
d_{TS}	characteristic periodicity
ξ	characteristic length scale

5.2. Chemicals and Synthesis Methods

Synthesis of Polymer Nanoparticles. The polystyrene nanoparticle dispersions were synthesized via emulsion polymerization. Therefore, 170 ml degassed bidistilled water, (21.0 mL, 0.18 mol) styrene (99%, Sigma-Aldrich) and the respective amount of sodium dodecyl sulfate SDS (>99%, Sigma-Aldrich) were stirred in a three-necked round bottom glass flask, under nitrogen atmosphere, equipped with a stirrer, a heater and a reflux condenser and heated up to 80 °C. The polymerization was initiated by the addition of (0.3 g, 0.93 mmol) potassium peroxodisulfate (99%, Fluka) dissolved in 10 ml degassed bidistilled water, and reacted for 4.5 h. Moreover, (0.2 g, 0.92 mmol) of the chain transfer agent 2-ethyl hexyl thioglycolate (>95%, from Sigma-Aldrich) was added together with the monomer to the reaction mixture. The hydrodynamic diameter d_H was measured by dynamic light scattering (DLS). After 4.5 h the dispersion was cooled down to room temperature and filtrated using filter paper with 4-12 μm particle retention. To form the colloidal crystals, the dispersion was left aside uncovered at room temperature for somedays until the solvent was completely evaporated.

The synthesis of PS nanoparticles with $d_{particle}$ = 48 ± 6 nm were performed, as described above, using 13.1 mM SDS, while a 1 ml of the polymerization mixture was taken each 30 minutes.

Foaming Experiments via the NF-CID Method. The foaming experiments were carried out in a batch process using an in-house built high pressure sapphire cell [149] shown in Figure 5.1. The cell is equipped with a sapphire cylinder (h = 50 mm, $Ø_{internal}$ = 10 mm, $Ø_{external}$ = 40 mm) that allows to observe the entire sample volume of about 3 ml. Pressures up to p = 400 ±5 bar can be generated by turning a piston down into the sapphire cylinder. The pressure is measured by a miniature pressure transducer (Type 81530, Burster, Germany), placed in a casing at the bottom of the sample cell. In order to control the temperature with an accuracy of ΔT = ±0.02 K, the whole pressure cell is placed in a thermostated water bath.

For the foaming experiments, the colloidal crystals were put on a sample holder in the high-pressure cell. After the cell is closed with the piston, it is filled with liquid CO_2 (at room temperature and 72 bar) through a valve. Then the cell is transferred to the water bath to adjust the temperature. When thermal equilibrium is reached, the pressure is adjusted

moving the piston accordingly. After a targeted time at this pressure and temperature (exposure time), the pressure is released opening the valve rapidly.

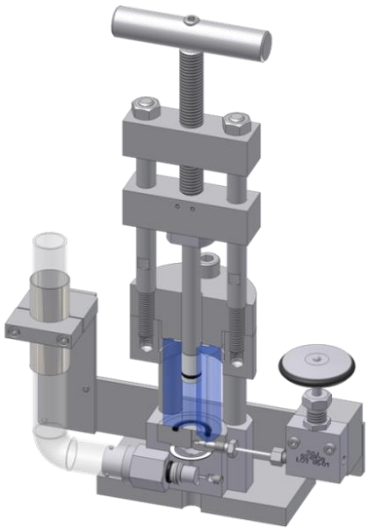

Figure 5.1: 3D- cross section of the home-built high-pressure view cell, which was used for the foaming experiments. The pressure was controlled by adjusting the position of the piston inside the sapphire cylinder (highlighted in blue). The valve is used for the gas inlet and expansion.

Synthesis of Porous Organic/Inorganic Hybrid Materials. A piece of porous polystyrene was placed in the vessel with deposition solution (described below) and let to infiltrate for 10 min. Then, the vessel was heated in an oil bath to 60 °C for 1.5 h (1 deposition cycle). Subsequently, the porous polymer was thoroughly rinsed with methanol and left in methanol for 1 h under stirring. Before starting the next cycle, the porous polymer piece was dried under inert gas and then placed in the fresh deposition solution. After the last washing step, the ZnO mineralized polymer was dried under vacuum for 3 h. A reference sample was prepared in parallel by heating a piece of porous polystyrene cube in methanol at 60 °C for 1.5 h.

Stock solutions preparation: Methanol stock solutions of $Zn(OOCCH_3)_2 \bullet 2\ H_2O$ (34 mM) from Sigma-Aldrich, tetraethylammonium hydroxide (TEAOH) (75 mM) purchased Aldrich Chemistry and polyvinylpyrrolidone (PVP) (21.7 mM) (M_w = 10000, Lot # BCBJ4889V) purchased from Sigma-Aldrich, were prepared. One volume unit of the zinc acetate was mixed with one volume unit of PVP stock solution. Then, one volume unit of TEAOH stock solution was added dropwise using a peristaltic pump at a flow rate of 1.04 mL min^{-1} under continuous stirring. Thus, a precursor solution with a ratio of [PVP]:[Zn^{2+}]:[TEAOH] = 1:1:1 and final concentrations of [PVP] = 7.23 mM, [Zn^{2+}] = 11.34 mM, and [TEAOH] = 25 mM were obtained. The precursor solution was always

prepared freshly prior to use. The deposition solution was obtained by adding 2 vol% nanopure water to the precursor solution resulting in a total volume of 3 ml.

Procedure for the Rh-catalyzed Asymmetric 1,2-Addition.

(dioxane and toluene) According to [123] under a nitrogen atmosphere $[Rh(C_2H_4)Cl]_2$ (1.94 mg, 4.99 μmol) and the respective chiral diene ligand (11.0 μmol) were dissolved in degassed dioxane/toluene (1.6 mL) and stirred for 15 min at room temperature. Degassed 3.1 M KOH solution (12.9 μL, 40.0 μmol) was added and the reaction mixture was stirred for another 5 min at room temperature. *N*-tosylimine **1** (58.8 mg, 0.20 mmol) and boroxine **2** (74.8 mg, 0.24 mmol) were added and the reaction mixture was stirred for 24 h at 60 °C. After cooling to room temperature, the solution was filtered through silica and rinsed with EtOAc (3 × 30 mL). The solvent was removed under reduced pressure and the crude product was purified by column chromatography on silica.

(microemulsion) Under a nitrogen atmosphere *n*-octyl-β-D-glucopyranoside (C_8G_1, 0.60 g, 2.05 mmol), $[Rh(C_2H_4)Cl]_2$ (1.94 mg, 4.99 μmol) and the respective chiral diene ligand (11.0 μmol) were dissolved in degassed toluene (0.80 mL) and degassed water (0.70 mL) and stirred for 15 min at room temperature. Degassed 3.1 M KOH solution (12.9 μL, 40.0 μmol) was added and the reaction mixture was stirred for another 5 min at room temperature. *N*-tosylimine **1** (58.8 mg, 0.20 mmol) and boroxine **2** (74.8 mg, 0.24 mmol) were added and the reaction mixture was stirred for 24 h at 60 °C. After cooling to room temperature, the solution was filtered through silica and rinsed with EtOAc (3 × 30 mL). The solvent was removed under reduced pressure and the crude product was purified by column chromatography on silica.

Kinetic Studies of the Rh-catalyzed Asymmetric 1,2-Addition. Under a nitrogen atmosphere *n*-octyl-β-D-glucopyranoside (C_8G_1, 0.80 g, 2.73 mmol), $[Rh(C_2H_4)Cl]_2$ (2.59 mg, 6.65 μmol) and the respective chiral diene ligand (14.63 μmol) were dissolved in degassed water (1.03 mL) and toluene (1.21 mL) and heated with stirring to the given temperature. After addition of degassed 3.1 M KOH solution (17.16 μL, 53.19 μmol), *N*-tosylimine **1** (78.14 mg, 265.99 μmol) and boroxine **2** (99.51 mg, 319.19 μmol), aliquots of 0.1 mL were taken in time intervals of 0, 4, 8, 16, 32, 64 and 128 min and filtered through a small pad of SiO_2 with EtOAc. The filtrate was concentrated, the residue taken up in $CDCl_3$ (0.4 mL) and 1,3,5-trimethylbenzene (1.67 μL or 1.64 μL for ME) and the reaction

mixture analyzed by NMR as described below. The same procedure was performed in the dioxane and toluene using (2.24 mL) of the respective solvent.

5.3. Experimental Methods

5.2.1. Phase Behavior Measurements

The optical determination of the phase boundaries of the phase diagram was conducted in a water bath thermostated with Thermo Electron Model Haake DC30 thermostat with a temperature control up to $\Delta T = \pm 0.1$ K. To record the phase boundaries at temperatures below room temperature an additional cooling loop was connected to a cooling thermostat from Lauda Model E 300. The required chemicals of each sample were weighed into a test tube with a precision of $\Delta m = \pm 0.0001$ g. Then a stirring bar is added, the test tube was sealed with a polyethylene stopper and placed in the water bath. Prior to the determination of the phase boundaries, the samples are stirred and homogenized at $T = 55$ °C. Afterwards the desired temperature of the water bath is adjusted while stirring the sample. When the temperature equilibrium is reached, the stirring process is turned off, and the type and number of coexisting phases are determined visually. All appearing phases and phase transition temperatures are determined with a precision of $\Delta T = \pm 0.05$ K. Afterwards the samples are diluted to the next composition.

The sample compositions are given using the nomenclature suggested by [150] i.e. the mass fraction α of oil (B) in the water (A)/oil (B) mixture

$$\alpha = \frac{m_B}{m_A + m_B}.$$

and the mass fraction of the surfactant (C) in the overall mixture:

$$\gamma = \frac{m_C}{m_A + m_B + m_C}.$$

In case a mixture of C_6E_5 and C_8G_1 surfactants is used, the mass fraction of C_8G_1 in the mixture of surfactants is defined by

$$\delta = \frac{m_{C8G1}}{m_{C6E5} + m_{C8G1}}.$$

In case KOH was added, the mass fraction of KOH in the mixture of water and KOH is given by

$$\varepsilon_{KOH} = \frac{m_{KOH}}{m_{H2O} + m_{KOH}}.$$

If cyclohexane is partially replaced by toluene, the mass fraction of toluene in the mixture of cyclohexane and toluene is defined by

$$\beta = \frac{m_{toluene}}{m_{toluene} + m_{cyclohexane}}.$$

To study the influence of *N*-tosylimine **1** on the phase behaviors a 7.1 wt% solution of **1** in toluene instead of pure toluene was used to prepare the microemulsion at γ = 0.32. However, in order to avoid the precipitation of **1**, which was observed in the stock solution of *N*-tosylimine **1** and toluene at temperatures T = 59.6±0.5 °C but not in the microemulsion, the phase diagram was recorded by adding H_2O/KOH and pure toluene to adjust lower γ-values. Thus, the concentration of **1** in toluene decreases slightly with decreasing surfactant mass fraction. In case of boroxine **2**, a 8.8 wt% solution of **2** in toluene was used to prepare the microemulsion at γ = 0.32. Again, in order to avoid the precipitation of **2**, which was observed in the **2**/toluene stock solution (T = 56.0 ± 0.5 °C) but not in the microemulsion, the phase diagram was recorded by adding H_2O/KOH and pure toluene to adjust lower γ-values.

Furthermore, the influence of the both *N*-tosylimine **1**/boroxine **2** on the phase behaviour was studied using a mixture of *N*-tosylimine **1**/boroxine **2** (7.1 wt%/8.8 wt% in toluene at γ = 0.32) by adding H_2O/KOH and pure toluene to adjust the lower γ-values.

5.2.2. Dynamic Light Scattering (DLS)

DLS is a well-known method for measuring the size of dispersed particles in the sub-micron region. Due to thermal density fluctuations the solvent molecules "hit" the dispersed particles leading to a random movement, which is known as Brownian motion. The larger the particle the slower the Brownian motion is. This motion can be described by the random-walk-motion. [151]. By means of DLS the diffusion of the dispersed particles can be characterized utilizing a coherent monochromatic light beam such as laser. In this method the speed at which the particles are diffusing is measured by detecting the rate at which the intensity of the scattered light fluctuates.

The dispersion of PS nanoparticle particles, synthesized via emulsion polymerization, were studied by DLS at 25 °C using a 3D LS spectrometer (LS Instruments, Switzerland). The

samples were irradiated with coherent, monochromatic light of a Helium/Neon-Laser (λ=633 nm). The scattering of diluted samples was measured at an angle of 90 °. To ensure the reproducibility of the results all measurements were repeated three times. The intensity of the scattered light was detected by a photomultiplier and converted by a correlator into an intensity-time-autocorrelation function, which were analyzed using *CONTIN* [152].

5.2.3. Gel-Permeation Chromatography (GPC)

The average molecular weight distribution was measured using GPC of Infinity 1260 instrument from Agilent. The instrument equipped with a column of modified Styrene-Divinylbenzene-Copolymer matrix (Linear M SDV, PSS) with a UV-detector (PSS SECcurity UV, PSS) and a refractive index detector (PSS SECcurity RI-detector, PSS). The synthesized polymer nanoparticles were dissolved in THF. The concentration was 0.5 g/L. The elugram was evaluated by means of a software of Agilent.

5.2.4. Differential Scanning Calorimetry (DSC)

The glass transition temperature T_g of the synthesized polystyrene was measured using DSC 800 calorimeter from Perkin Elmer. The samples were investigated between T = - 60 °C and T = - 140 °C with heating and cooling rate of 10 K/min. The thermograms was analyzed using the software form Perkin Elmer.

5.2.5. Scanning Electron Microscopy (SEM)

The scanning electron microscopy (SEM) examinations of the polystyrene nanoparticle crystals, the polystyrene porous polymers and porous PS/ZnO hybrid were conducted on Zeiss Merlin SEM at 3 kV (for polystyrene nanoparticles at 10 kV). For porous polystyrene all samples were fractured in liquid nitrogen to generate a breaking edge of the sample, so that the internal structure could be investigated: To avoid charging of the sample the fixation was performed using silver lacquer. Additionally, the polystyrene samples were sputtered with 5.0 nm Iridium, while the porous PS/ZnO hybrid materials were sputtered with 0.3 nm Iridium. Scanning electron microscopy (SEM) coupled with energy dispersive X-ray *(EDX)*, measurements were conducted on a Zeiss Ultra 55 microscope. Thereby, the EDX spectra were obtained with a nitrogen-cooled EDAX detector.

5.2.6. Uniaxial Compression Measurement

A BOSE ElectroForce 3200 Series III instrument, which is controlled via a WinTest7 control system and equipped with a load cell capable to bear 220 N, was used to perform uniaxial

compression measurements on rectangular samples of porous polystyrene and porous PS/ZnO hybrid material with a strain rate of $5.0 \cdot 10^{-3}$ mm/s and up to 70 % compression.

5.2.7. Small-Angle X-ray Scattering (SAXS)Measurement

The microstructure of the bicontinuous microemulsion used as reaction media was investigated using small-angle X-ray scattering (SAXS). The SAXS measurements were carried out with the SAXSess system (Anton Paar GmbH, detector: Mythen 2 1 K Dectris). The samples were filled with the aid of a tempered syringe in Mark tubes from Hilgenberg made of quartz glass (outer diameter: 0.7 mm, wall thickness 0.01 mm) then the tube was sealed. The samples were measured at a temperature of T = 60 °C. 180 single shots were taken with an exposure time of 60 s. The resulting data were processed and analyzed using the SAXSquant software of the SAXSess device.

For data analysis the Teubner-Strey model[147] was used to describe the scattering intensity recorded around the maximum.

$$I(q) = \frac{1}{a_0 + a_1 q^2 + a_2 q^4}$$

with a_0, a_1 and a_2 being the coefficients of the order parameter expansion defining the periodicity d_{TS} and the correlation length ξ_{TS} according to

$$d_{TS} = 2\pi \left[\frac{1}{2} \left(\frac{a_0}{a_2} \right)^{1/2} - \frac{1}{4} \frac{a_1}{a_2} \right]^{-1/2} \text{ and}$$

$$\xi_{TS} = \left[\frac{1}{2} \left(\frac{a_0}{a_2} \right)^{1/2} + \frac{1}{4} \frac{a_1}{a_2} \right]^{-1/2}$$

5.2.8. Profile Analysis Tensiometer

The influence of boroxine **2** on the interfacial tensions (IFT) between water and toluene were carried out at T = 25°C with the Profile Analysis Tensiometer PAT-1 from Sinterface Technologies. The interfacial tension σ between the two liquids is determined by creating a pendant drop of water at the tip of a capillary inside the lighter liquid (in this case the mixture of boroxine and toluene). Then taking an image of a drop and transfer it via a frame grabber to the PC, where the coordinates of the axisymmetric meniscus are extracted, and

the Gauss-Laplace equation is fitted. Using the macroscopic densities of the two liquids the interfacial tension is the only free parameter of this fitting procedure. The accuracy of the technique is ± 0.1 mNm^{-1}. The interfacial tension is measured as a function of time until the equilibrium value is reached (in these experiments 1500 s).

5.4. Additional Figures

Effect of boroxine 1 on the interfacial tension between water and toluene

The following figure shows the interfacial tension between water and toluene as a function of the boroxine **1** concentration in toluene at T = 25 °C using the pendant drop method.

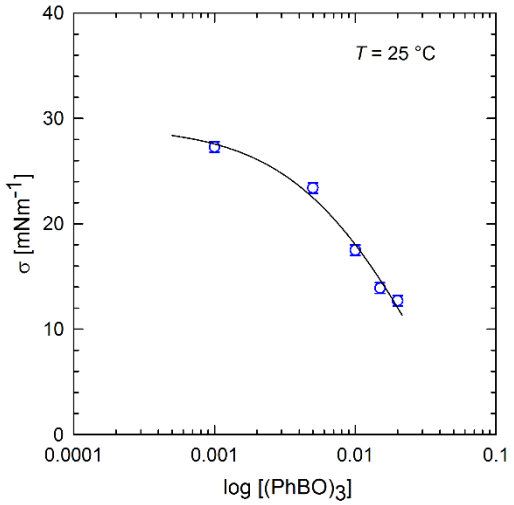

Figure 5.2: Semi-logarithmic plot of the water/toluene interfacial tension (determined with the pendant drop method) as a function of the concentration of **2** in toluene at T = 25 °C. The interfacial tension was found to decrease from 36 mNm^{-1} (value from [146]) to 12 mNm^{-1} increasing the concentration to 2.0 wt%. Note that decrease is most probably related to the formation of amphiphilic hydrolysis products as e.g. boronic acid. The solid line shows the fit of the data by Langmuir-Szyszkowski model [153]. Figure is taken from [143].

6 References

[1] M. Beller, "Preface for the themed issue of Chemical Society Reviews," *Chemical Society reviews*, vol. 40, no. 10, pp. 4891–4892, 2011.

[2] S. Caron, A. Ghosh, S. Gut Ruggeri et al., "Selected Metal-Mediated Cross-Coupling Reactions," in *Practical synthetic organic chemistry*: *Reactions, principles, and techniques,* S. Caron, Ed., pp. 279–340, Wiley, Hoboken, N.J, 2011.

[3] B. Cornils and W. A. Herrmann, *Applied homogeneous catalysis with organometallic compounds*, Wiley-VCH, Weinheim, 2002.

[4] K. N. Ferreira, T. M. Iverson, K. Maghlaoui et al., "Architecture of the photosynthetic oxygen-evolving center," *Science (New York, N.Y.)*, vol. 303, no. 5665, pp. 1831–1838, 2004.

[5] J. E. Karroumi, A. E. Haib, E. Manoury et al., "Selectivity controlled by ligand tuning in the palladium-catalysed cyclocarbonylation: Synthesis of new γ and δ lactones from a natural sesquiterpene," *Journal of Molecular Catalysis A: Chemical*, vol. 401, pp. 18–26, 2015.

[6] Z. J. Wang, K. N. Clary, R. G. Bergman et al., "A supramolecular approach to combining enzymatic and transition metal catalysis," *Nature chemistry*, vol. 5, no. 2, pp. 100–103, 2013.

[7] D. L. Pompliano, A. Peyman, and J. R. Knowles, "Stabilization of a reaction intermediate as a catalytic device: definition of the functional role of the flexible loop in triosephosphate isomerase," *Biochemistry*, vol. 29, no. 13, pp. 3186–3194, 1990.

[8] J. A. Kelly and M.N.G. James, *X-RAY CRYSTALLOGRAPHY OF THE BINDING OF THE BACTERIAL CELL WALL TRISACCHARIDE NAM-NAG-NAM TO LYSOZYME*, 1980.

[9] D. M. Vriezema, M. Comellas Aragonès, J. A. A. W. Elemans et al., "Self-assembled nanoreactors," *Chemical reviews*, vol. 105, no. 4, pp. 1445–1489, 2005.

[10] M. Raynal, P. Ballester, A. Vidal-Ferran et al., "Supramolecular catalysis. Part 2: artificial enzyme mimics," *Chemical Society reviews*, vol. 43, no. 5, pp. 1734–1787, 2014.

[11] G. Sastre and A. Corma, "The confinement effect in zeolites," *Journal of Molecular Catalysis A: Chemical*, vol. 305, no. 1, pp. 3–7, 2009.

[12] F. Vermoortele, M. Vandichel, B. van de Voorde et al., "Electronic effects of linker substitution on Lewis acid catalysis with metal-organic frameworks," *Angewandte Chemie (International ed. in English)*, vol. 51, no. 20, pp. 4887–4890, 2012.

[13] S. Royuela, R. Gil-San Millán, M. J. Mancheño et al., "Catalytically Active Imine-based Covalent Organic Frameworks for Detoxification of Nerve Agent Simulants in Aqueous Media," *Materials (Basel, Switzerland)*, vol. 12, no. 12, 2019.

[14] F. Hapiot, A. Ponchel, S. Tilloy et al., "Cyclodextrins and their applications in aqueous-phase metal-catalyzed reactions," *Comptes Rendus Chimie*, vol. 14, 2-3, pp. 149–166, 2011.

[15] J. Chen and J. Rebek, "Selectivity in an encapsulated cycloaddition reaction," *Organic letters*, vol. 4, no. 3, pp. 327–329, 2002.

[16] S. Otto and J. B. F. N. Engberts, "Diels_Alder reactions in water," *Pure and Applied Chemistry*, vol. 72, no. 7, pp. 1365–1372, 2000.

[17] M. Schmidt, C. Urban, S. Schmidt et al., "Palladium-Catalyzed Hydroxycarbonylation of 1-Dodecene in Microemulsion Systems: Does Reaction Performance Care about Phase Behavior?," *ACS omega*, vol. 3, no. 10, pp. 13355–13364, 2018.

[18] V. Mouarrawis, R. Plessius, J. I. van der Vlugt et al., "Confinement Effects in Catalysis Using Well-Defined Materials and Cages," *Frontiers in chemistry*, vol. 6, p. 623, 2018.

[19] A. Choplin and F. Quignard, "From supported homogeneous catalysts to heterogeneous molecular catalysts," *Coordination Chemistry Reviews*, 178-180, pp. 1679–1702, 1998.

[20] D. Wu, F. Xu, B. Sun et al., "Design and preparation of porous polymers," *Chemical reviews*, vol. 112, no. 7, pp. 3959–4015, 2012.

[21] J. Martín-de León, V. Bernardo, and M. Á. Rodríguez-Pérez, "Nanocellular Polymers: The Challenge of Creating Cells in the Nanoscale," *Materials (Basel, Switzerland)*, vol. 12, no. 5, 2019.

[22] R. Strey and A. Müller, *Generation of nanodisperse inclusions in a high-viscosity matrix*: *Patent*, 2010.

[23] H. Yi, F. Li, P. Ning et al., "Adsorption separation of CO2, CH4, and N2 on microwave activated carbon," *Chemical Engineering Journal*, 215-216, pp. 635–642, 2013.

[24] A. K. Sekizkardes, V. A. Kusuma, G. Dahe et al., "Separation of carbon dioxide from flue gas by mixed matrix membranes using dual phase microporous polymeric constituents," *Chemical communications (Cambridge, England)*, vol. 52, no. 79, pp. 11768–11771, 2016.

[25] H.-J. Wu, J.-T. Fan, and N. Du, "Porous Materials with Thin Interlayers for Optimal Thermal Insulation," *International Journal of Nonlinear Sciences and Numerical Simulation*, vol. 10, no. 3, 2009.

[26] A. Rizvi, R. K. M. Chu, and C. B. Park, "Scalable Fabrication of Thermally Insulating Mechanically Resilient Hierarchically Porous Polymer Foams," *ACS applied materials & interfaces*, vol. 10, no. 44, pp. 38410–38417, 2018.

[27] Q. Fang, J. Wang, S. Gu et al., "3D Porous Crystalline Polyimide Covalent Organic Frameworks for Drug Delivery," *Journal of the American Chemical Society*, vol. 137, no. 26, pp. 8352–8355, 2015.

[28] Y. Zhang and S. N. Riduan, "Functional porous organic polymers for heterogeneous catalysis," *Chemical Society reviews*, vol. 41, no. 6, pp. 2083–2094, 2012.

[29] T. Ennaert, J. van Aelst, J. Dijkmans et al., "Potential and challenges of zeolite chemistry in the catalytic conversion of biomass," *Chemical Society reviews*, vol. 45, no. 3, pp. 584–611, 2016.

[30] C. Gu, N. Huang, J. Gao et al., "Controlled synthesis of conjugated microporous polymer films: versatile platforms for highly sensitive and label-free chemo- and biosensing," *Angewandte Chemie (International ed. in English)*, vol. 53, no. 19, pp. 4850–4855, 2014.

[31] Y. Conde, J.-F. Despois, R. Goodall et al., "Replication Processing of Highly Porous Materials," *Advanced Engineering Materials*, vol. 8, no. 9, pp. 795–803, 2006.

[32] M. Ousalem, X.X. Zhu, and J. Hradil, "Evaluation of the porous structures of new polymer packing materials by inverse size-exclusion chromatography," *Journal of Chromatography A*, vol. 903, 1-2, pp. 13–19, 2000.

[33] J. Wu, F. Xu, S. Li et al., "Porous Polymers as Multifunctional Material Platforms toward Task-Specific Applications," *Advanced materials (Deerfield Beach, Fla.)*, vol. 31, no. 4, e1802922, 2019.

[34] P. Liu and G.-F. Chen, *Porous Materials*: *Processing and Applications*, Elsevier, Amsterdam, 2014.

[35] S. K. Goel and E. J. Beckman, "Generation of microcellular polymers using supercritical CO2," *cellular polymers*, vol. 12, p. 251, 1993.

[36] S. Jiang, S. Agarwal, and A. Greiner, "Low-Density Open Cellular Sponges as Functional Materials," *Angewandte Chemie (International ed. in English)*, vol. 56, no. 49, pp. 15520–15538, 2017.

[37] K. Sing, D. Everett, R. Haul et al., "Reporting physisorption data for gas/solid systems with special reference to the determination of surface area and porosity (IUPAC Recommendations 1984)," *Pure and Applied Chemistry*, vol. 57, no. 4, pp. 603–619, 1985.

[38] R. Dawson, A. I. Cooper, and D. J. Adams, "Nanoporous organic polymer networks," *Progress in Polymer Science*, vol. 37, no. 4, pp. 530–563, 2012.

[39] C. Okolieocha, D. Raps, K. Subramaniam et al., "Microcellular to nanocellular polymer foams: Progress (2004–2015) and future directions – A review," *European Polymer Journal*, vol. 73, pp. 500–519, 2015.

[40] J. Rouquerol, D. Avnir, C. W. Fairbridge et al., "Recommendations for the characterization of porous solids (Technical Report)," *Pure and Applied Chemistry*, vol. 66, no. 8, pp. 1739–1758, 1994.

[41] M. Knudsen, *The Kinetic Theory of Gases: Some Modern Aspects.*, London: Methuen & Co. Ltd, 1934.

[42] S. A. Hosseini and H. V. Tafreshi, "On the importance of fibers' cross-sectional shape for air filters operating in the slip flow regime," *Powder Technology*, vol. 212, no. 3, pp. 425–431, 2011.

[43] A. Thomas, F. Goettmann, and M. Antonietti, "Hard Templates for Soft Materials: Creating Nanostructured Organic Materials †," *Chemistry of Materials*, vol. 20, no. 3, pp. 738–755, 2008.

[44] D. A. Olson, L. Chen, and M. A. Hillmyer, "Templating Nanoporous Polymers with Ordered Block Copolymers †," *Chemistry of Materials*, vol. 20, no. 3, pp. 869–890, 2008.

[45] L. Grassberger, K. Koch, R. Oberhoffer et al., "Blowing agent free generation of nanoporous poly(methylmethacrylate) materials," *Colloid and Polymer Science*, vol. 295, no. 2, pp. 379–389, 2017.

[46] C. Forest, P. Chaumont, P. Cassagnau et al., "Polymer nano-foams for insulating applications prepared from CO2 foaming," *Progress in Polymer Science*, vol. 41, pp. 122–145, 2015.

[47] F. S. Bates and G. H. Fredrickson, "Block Copolymers—Designer Soft Materials," *Physics Today*, vol. 52, no. 2, pp. 32–38, 1999.

[48] R. Nisticò, "Block copolymers for designing nanostructured porous coatings," *Beilstein journal of nanotechnology*, vol. 9, pp. 2332–2344, 2018.

[49] J. M. Andino, "Chlorofluorocarbons (CFCs) are heavier than air, so how do scientists suppose that these chemicals reach the altitude of the ozone layer to adversely affect it?," *Scientific American*, vol. 264, p. 68, 1999.

[50] S. K. Goel and E. J. Beckman, "Generation of microcellular polymeric foams using supercritical carbon dioxide. I: Effect of pressure and temperature on nucleation," *Polymer Engineering and Science*, vol. 34, no. 14, pp. 1137–1147, 1994.

[51] S. K. Goel and E. J. Beckman, "Generation of microcellular polymeric foams using supercritical carbon dioxide. II: Cell growth and skin formation," *Polymer Engineering and Science*, vol. 34, no. 14, pp. 1148–1156, 1994.

[52] K. A. Arora, A. J. Lesser, and T. J. McCarthy, "Preparation and Characterization of Microcellular Polystyrene Foams Processed in Supercritical Carbon Dioxide," *Macromolecules*, vol. 31, no. 14, pp. 4614–4620, 1998.

[53] M.-T. Liang and C.-M. Wang, "Production of Engineering Plastics Foams by Supercritical CO2," *Industrial & Engineering Chemistry Research*, vol. 39, no. 12, pp. 4622–4626, 2000.

[54] M. Xanthos, U. Yilmazer, S. K. Dey et al., "Melt viscoelasticity of polyethylene terephthalate resins for low density extrusion foaming," *Polymer Engineering & Science*, vol. 40, no. 3, pp. 554–566, 2000.

[55] Y. Ema, M. Ikeya, and M. Okamoto, "Foam processing and cellular structure of polylactide-based nanocomposites," *Polymer*, vol. 47, no. 15, pp. 5350–5359, 2006.

[56] M. J. Jenkins, K. L. Harrison, M.M.C.G. Silva et al., "Characterisation of microcellular foams produced from semi-crystalline PCL using supercritical carbon dioxide," *European Polymer Journal*, vol. 42, no. 11, pp. 3145–3151, 2006.

[57] Z.-M. Xu, X.-L. Jiang, T. Liu et al., "Foaming of polypropylene with supercritical carbon dioxide," *The Journal of Supercritical Fluids*, vol. 41, no. 2, pp. 299–310, 2007.

[58] J. D. Gunton, "Homogeneous Nucleation," *Journal of statistical physics*, vol. 95, pp. 903–923, 1999.

[59] M. A. Shafi and R. W. Flumerfelt, "Initial bubble growth in polymer foam processes," *Chemical Engineering Science*, vol. 52, pp. 627–633, 1997.

[60] I. Tsivintzelis, G. Sanxaridou, E. Pavlidou et al., "Foaming of polymers with supercritical fluids: A thermodynamic investigation," *The Journal of Supercritical Fluids*, vol. 110, pp. 240–250, 2016.

[61] C. Panayiotou, M. Pantoula, E. Stefanis et al., "Nonrandom Hydrogen-Bonding Model of Fluids and Their Mixtures. 1. Pure Fluids," *Industrial & Engineering Chemistry Research*, vol. 43, pp. 6592–6606, 2004.

[62] S. Costeux, "CO 2 -blown nanocellular foams," *Journal of Applied Polymer Science*, vol. 131, no. 23, 41293-41309, 2014.

[63] S. Nakano and M. Shimbo, "Experiments on Solid-state Cell Nucleation in Polystyrene and Polycarbonate as a Function of Foaming Temperature and Foaming Time," *cellular polymers*, vol. 25, no. 3, pp. 127–142, 2006.

[64] R. P. Juntunen, V. Kumar, J. E. Weller et al., "Impact strength of high density microcellular poly(vinyl chloride) foams," *Journal of Vinyl and Additive Technology*, vol. 6, no. 2, pp. 93–99, 2000.

[65] A. Gandhi, N. Asija, K. Kumar Gaur et al., "Ultrasound assisted cyclic solid-state foaming for fabricating ultra-low density porous acrylonitrile–butadiene–styrene foams," *Materials Letters*, vol. 94, pp. 76–78, 2013.

[66] J. A. Reglero, P. Viot, and M. Dumon, "Foaming of amorphous polymers and blends in supercritical CO 2 : Solubility versus block copolymers addition," *Journal of Cellular Plastics*, vol. 47, no. 6, pp. 535–548, 2011.

[67] Y.-T. Shieh and K.-H. Liu, "Solubility of CO2 in Glassy PMMA and PS over a Wide Pressure Range: The Effect of Carbonyl Groups," *Journal of Polymer Research*, vol. 9, no. 2, pp. 107–113, 2002.

[68] Y. P. Handa and Z. Zhang, "A new technique for measuring retrograde vitrification in polymer-gas systems and for making ultramicrocellular foams from the retrograde phase," *Journal of Polymer Science Part B: Polymer Physics*, vol. 38, no. 5, pp. 716–725, 2000.

[69] J. A. Reglero Ruiz, M. Dumon, J. Pinto et al., "Low-Density Nanocellular Foams Produced by High-Pressure Carbon Dioxide," *Macromolecular Materials and Engineering*, vol. 296, no. 8, pp. 752–759, 2011.

[70] S. Costeux, I. Khan, S. P. Bunker et al., "Experimental study and modeling of nanofoams formation from single phase acrylic copolymers," *Journal of Cellular Plastics*, vol. 51, no. 2, pp. 197–221, 2015.

[71] B. Krause, H. J. P. Sijbesma, P. Münüklü et al., "Bicontinuous Nanoporous Polymers by Carbon Dioxide Foaming," *Macromolecules*, vol. 34, no. 25, pp. 8792–8801, 2001.

[72] D. Miller, P. Chatchaisucha, and V. Kumar, "Microcellular and nanocellular solid-state polyetherimide (PEI) foams using sub-critical carbon dioxide I. Processing and structure," *Polymer*, vol. 50, no. 23, pp. 5576–5584, 2009.

[73] B. Krause, G.-H. Koops, N.F.A. van der Vegt et al., "Ultralow-k Dielectrics Made by Supercritical Foaming of Thin Polymer Films," *Advanced Materials*, vol. 14, no. 15, p. 1041, 2002.

[74] T. Otsuka, K. Taki, and M. Ohshima, "Nanocellular Foams of PS/PMMA Polymer Blends," *Macromolecular Materials and Engineering*, vol. 293, no. 1, pp. 78–82, 2008.

[75] S. Costeux, S. P. Bunker, and H. K. Jeon, "Homogeneous nanocellular foams from styrenic-acrylic polymer blends," *Journal of Materials Research*, vol. 28, no. 17, pp. 2351–2365, 2013.

[76] J. S. Colton and N. P. Suh, "The nucleation of microcellular thermoplastic foam with additives: Part I: Theoretical considerations," *Polymer Engineering and Science*, vol. 27, pp. 485–492, 1987.

[77] S. Siripurapu, J. M. DeSimone, S. A. Khan et al., "Controlled Foaming of Polymer Films through Restricted Surface Diffusion and the Addition of Nanosilica Particles or CO2-philic Surfactants," *Macromolecules*, vol. 38, no. 6, pp. 2271–2280, 2005.

[78] V. Realinho, M. Antunes, A. B. Martínez et al., "Influence of Nanoclay Concentration on the CO2 Diffusion and Physical Properties of PMMA Montmorillonite Microcellular Foams," *Industrial & Engineering Chemistry Research*, vol. 50, no. 24, pp. 13819–13824, 2011.

[79] I. Piirma, ed., *Emulsion polymerization*, Acad. Press, New York, 1982.

[80] K. Landfester, "Miniemulsion polymerization and the structure of polymer and hybrid nanoparticles," *Angewandte Chemie (International ed. in English)*, vol. 48, no. 25, pp. 4488–4507, 2009.

[81] M. Antonietti and H. ‐ P. Hentze, "Neuere Aspekte der Polymerisation in lyotropen Phasen und in Mikroemulsionen," *Chemie Ingenieur Technik*, vol. 69, no. 3, pp. 369–373, 1997.

[82] J. E. Puig and M. Rabelero, "Semicontinuous microemulsion polymerization," *Current Opinion in Colloid & Interface Science*, vol. 25, pp. 83–88, 2016.

[83] L. Grassberger, *Towards cost-efficient preparation of nanoporous materials: formation kinetics, process optimization and material characterization,* PhD Thesis, Verlag Dr. Hut; Universität zu Köln, 2016.

[84] P. D. Condo and K. P. Johnston, "In situ measurement of the glass transition temperature of polymers with compressed fluid diluents," *Journal of Polymer Science Part B: Polymer Physics*, vol. 32, no. 3, pp. 523–533, 1994.

[85] A. Müller, *Preparation of polymer nano-foams*: *Templates, challenges and kinetics,* PhD Thesis, 2013.

[86] W. Ostwald, "Über die vermeintliche Isomerie des roten und gelben Quecksilberoxyds und die Oberflächenspannung fester Körper," *Zeitschrift für Physikalische Chemie*, 34U, no. 1, 1900.

[87] S. Egelhaaf, U. Olsson, P. Schurtenberger et al., "Quantitative measurements of Ostwald ripening using time-resolved small-angle neutron scattering," *Physical review. E, Statistical physics, plasmas, fluids, and related interdisciplinary topics*, vol. 60, 5 Pt B, pp. 5681–5684, 1999.

[88] M. Smoluchowski, "Mathematical theory of the kinetics of the coagulation of colloidal solutions," *Zeitschrift für Physikalische Chemie*, vol. 19, pp. 129–135, 1917.

[89] P. Meakin, "Steady state droplet coalescence," *Physica A: Statistical Mechanics and its Applications*, vol. 171, no. 1, pp. 1–18, 1991.

[90] Y. Xia, B. Gates, Y. Yin et al., "Monodispersed Colloidal Spheres: Old Materials with New Applications," *Advanced Materials*, vol. 12, no. 10, pp. 693–713, 2000.

[91] M. Nomura, H. Tobita, and K. Suzuki, "Emulsion Polymerization: Kinetic and Mechanistic Aspects," in *Polymer Particles,* M. Okubo, Ed., vol. 175, pp. 1–128, Springer Berlin Heidelberg, Berlin, Heidelberg, 2005.

[92] S. C. Thickett and R. G. Gilbert, "Emulsion polymerization: State of the art in kinetics and mechanisms," *Polymer*, vol. 48, no. 24, pp. 6965–6991, 2007.

[93] W. D. Harkins, "A General Theory of the Reaction Loci in Emulsion Polymerization," *The Journal of Chemical Physics*, vol. 13, no. 9, pp. 381–382, 1945.

[94] "Kientics of Emulsion Polymerization," polymer database, 10/29/2018, https://polymerdatabase.com/polymer%20chemistry/Emulsion%20Polymerization2.html.

[95] W. V. Smith and R. H. Ewart, "Kinetics of Emulsion Polymerization," *The Journal of Chemical Physics*, vol. 16, no. 6, pp. 592–599, 1948.

[96] K. Abitaev, *Synthese von Polystyrol-Nanopartikeln: Einfluss der Partikelgröße und der Polydispersität auf das NF-CID Verfahren,* Master-Thesis, 2018.

[97] S. Paula, W. Sues, J. Tuchtenhagen et al., "Thermodynamics of Micelle Formation as a Function of Temperature: A High Sensitivity Titration Calorimetry Study," *The Journal of Physical Chemistry*, vol. 99, pp. 11742–11751, 1995.

[98] Y. Qawasmi, P. Atanasova, T. Jahnke et al., "Synthesis of nanoporous organic/inorganic hybrid materials with adjustable pore size," *Colloid and Polymer Science*, vol. 296, no. 11, pp. 1805–1816, 2018.

[99] H. Xu, X. Zheng, Y. Huang et al., "Interconnected Porous Polymers with Tunable Pore Throat Size Prepared via Pickering High Internal Phase Emulsions," *Langmuir : the ACS journal of surfaces and colloids*, vol. 32, no. 1, pp. 38–45, 2016.

[100] C. Sanchez, P. Belleville, M. Popall et al., "Applications of advanced hybrid organic-inorganic nanomaterials: from laboratory to market," *Chemical Society reviews*, vol. 40, no. 2, pp. 696–753, 2011.

[101] S. Weiner and Dove P., "An Overview of Biomineralization Processes and the Problem of the Vital Effect," *Reviews in Mineralogy and Geochemistry*, vol. 54, no. 1, pp. 1–29, 2003.

[102] C. J. Stephens, S. F. Ladden, F. C. Meldrum et al., "Amorphous Calcium Carbonate is Stabilized in Confinement," *Advanced Functional Materials*, vol. 20, no. 13, pp. 2108–2115, 2010.

[103] F. Barthelat, H. Tang, P. Zavattieri et al., "On the mechanics of mother-of-pearl: A key feature in the material hierarchical structure," *Journal of the Mechanics and Physics of Solids*, vol. 55, no. 2, pp. 306–337, 2007.

[104] S. Weiner and L. Addadi, "Crystallization Pathways in Biomineralization," *Annual Review of Materials Research*, vol. 41, no. 1, pp. 21–40, 2011.

[105] P. O'Brien and J. McAleese, "Developing an understanding of the processes controlling the chemical bath deposition of ZnS and CdS," *Journal of Materials Chemistry*, vol. 8, no. 11, pp. 2309–2314, 1998.

[106] T. Saeed and P. O'Brien, "Deposition and characterisation of ZnO thin films grown by chemical bath deposition," *Thin Solid Film*, vol. 271, pp. 35–38, 1995.

[107] S. Polarz, F. Neues, M. W. E. van den Berg et al., "Mesosynthesis of ZnO-silica composites for methanol nanocatalysis," *Journal of the American Chemical Society*, vol. 127, no. 34, pp. 12028–12034, 2005.

[108] F. Schröder, S. Hermes, H. Parala et al., "Non aqueous loading of the mesoporous siliceous MCM-48 matrix with ZnO: a comparison of solution, liquid and gas-phase infiltration using diethyl zinc as organometallic precursor," *J. Mater. Chem.*, vol. 16, no. 35, pp. 3565–3574, 2006.

[109] U. Suryavanshi, T. Iijima, A. Hayashi et al., "Fabrication of ZnO nanoparticles confined in the channels of mesoporous carbon," *Chemical Engineering Journal*, vol. 179, pp. 388–393, 2012.

[110] J. Shi, J. Chen, Z. Feng et al., "Time-resolved photoluminescence characteristics of subnanometer ZnO clusters confined in the micropores of zeolites," *The journal of physical chemistry. B*, vol. 110, no. 51, pp. 25612–25618, 2006.

[111] H. Ceylan, C. Ozgit-Akgun, T. S. Erkal et al., "Size-controlled conformal nanofabrication of biotemplated three-dimensional TiO_2 and ZnO nanonetworks," *Scientific reports*, vol. 3, p. 2306, 2013.

[112] S. Kovačič, A. Anžlovar, B. Erjavec et al., "Macroporous ZnO foams by high internal phase emulsion technique: synthesis and catalytic activity," *ACS applied materials & interfaces*, vol. 6, no. 21, pp. 19075–19081, 2014.

[113] P. Wang, J. Zhao, R. Xuan et al., "Flexible and monolithic zinc oxide bionanocomposite foams by a bacterial cellulose mediated approach for antibacterial applications," *Dalton transactions (Cambridge, England : 2003)*, vol. 43, no. 18, pp. 6762–6768, 2014.

[114] B. I. Seo, U.A. Shaislamov, M. H. Ha et al., "ZnO nanotubes by template wetting process," *Physica E: Low-dimensional Systems and Nanostructures*, vol. 37, 1-2, pp. 241–244, 2007.

[115] M. Ladanov, P. Algarin-Amaris, G. Matthews et al., "Microfluidic hydrothermal growth of ZnO nanowires over high aspect ratio microstructures," *Nanotechnology*, vol. 24, no. 37, p. 375301, 2013.

[116] P. Atanasova, N. Stitz, S. Sanctis et al., "Genetically improved monolayer-forming tobacco mosaic viruses to generate nanostructured semiconducting bio/inorganic hybrids," *Langmuir : the ACS journal of surfaces and colloids*, vol. 31, no. 13, pp. 3897–3903, 2015.

[117] P. Lipowsky, R. C. Hoffmann, U. Welzel et al., "Site-Selective Deposition of Nanostructured ZnO Thin Films from Solutions Containing Polyvinylpyrrolidone," *Advanced Functional Materials*, vol. 17, no. 13, pp. 2151–2159, 2007.

[118] L. J. Gibson, "Biomechanics of cellular solids," *Journal of biomechanics*, vol. 38, no. 3, pp. 377–399, 2005.

[119] K. A. Arora, A. J. Lesser, and T. J. McCarthy, "Compressive behavior of microcellular polystyrene foams processed in supercritical carbon dioxide," *Polymer Engineering & Science*, vol. 38, no. 12, pp. 2055–2062, 1998.

[120] B. H. Lipshutz, N. A. Isley, R. Moser et al., "Rhodium-Catalyzed Asymmetric 1,4-Additions, in Water at Room Temperature, with In-Flask Catalyst Recycling," *Advanced synthesis & catalysis*, vol. 354, no. 17, pp. 3175–3179, 2012.

[121] G. Berthon-Gelloz and T. Hayashi, "Expanding the C2-symmetric bicyclo2.2.1hepta-2,5-diene ligand family: concise synthesis and catalytic activity in rhodium-catalyzed asymmetric addition," *The Journal of organic chemistry*, vol. 71, no. 23, pp. 8957–8960, 2006.

[122] Y.-J. Chen, Y.-H. Chen, C.-G. Feng et al., "Enantioselective rhodium-catalyzed arylation of cyclic N-sulfamidate alkylketimines: a new access to chiral β-alkyl-β-aryl amino alcohols," *Organic letters*, vol. 16, no. 12, pp. 3400–3403, 2014.

[123] T. Mühlhäuser, A. Savin, W. Frey et al., "Role of Regioisomeric Bicyclo3.3.0octa-2,5-diene Ligands in Rh Catalysis: Synthesis, Structural Analysis, Theoretical Study, and Application in Asymmetric 1,2- and 1,4-Additions," *The Journal of organic chemistry*, vol. 82, no. 24, pp. 13468–13480, 2017.

[124] M. Kahlweit and R. Strey, "Phase Behavior of Ternary Systems of the Type H2O-Oil-Nonionic Amphiphile (Microemulsions)," *Angewandte Chemie (International ed. in English),* no. 24, pp. 654–668, 1985.

[125] R. Strey, "Microemulsion microstructure and interfacial curvature," *Colloid and Polymer Science*, vol. 272, no. 8, pp. 1005–1019, 1994.

[126] T. Sottmann and R. Strey, "Microemulsions," in *Fundamentals of Interface and Colloid Science*: *Soft Colloids,* J. Lyklema, Ed., vol. 5, 5.1-5.96, Elsevier professional, s.l., 2005.

[127] M. Kahlweit and R. Strey, "Phase Behavior of Ternary Systems of the Type H2O?Oil?Nonionic Amphiphile (Microemulsions)," *Angewandte Chemie International Edition in English*, vol. 24, no. 8, pp. 654–668, 1985.

[128] D. J. Mitchell, G. J. T. Tiddy, L. Waring et al., "Phase behaviour of polyoxyethylene surfactants with water. Mesophase structures and partial miscibility (cloud points)," *Journal of the Chemical Society, Faraday Transactions 1: Physical Chemistry in Condensed Phases*, vol. 79, no. 4, p. 975, 1983.

[129] S. Burauer, T. Sachert, T. Sottmann et al., "On microemulsion phase behavior and the monomeric solubility of surfactant," *Physical Chemistry Chemical Physics*, vol. 1, no. 18, pp. 4299–4306, 1999.

[130] T. Sottmann, *Mikroemulsionen: Eigenschaften von internen Grenzflächen,* PhD-Thesis, 1997.

[131] D. F. Evans and H. Wennerström, *The colloidal domain*: *Where physics, chemistry, biology, and technology meet*, Wiley-VCH, New York, NY, 1999.

[132] M. A. López-Quintela, C. Tojo, M. C. Blanco et al., "Microemulsion dynamics and reactions in microemulsions," *Current Opinion in Colloid & Interface Science*, vol. 9, no. 3, pp. 264–278, 2004.

[133] K. Holmberg, "Organic reactions in microemulsions," *Current Opinion in Colloid & Interface Science*, vol. 8, no. 2, pp. 187–196, 2003.

[134] T. Sottmann, R. Strey, and S.-H. Chen, "A small-angle neutron scattering study of nonionic surfactant molecules at the water–oil interface: Area per molecule, microemulsion domain size, and rigidity," *The Journal of Chemical Physics*, vol. 106, no. 15, pp. 6483–6491, 1997.

[135] B. H. Lipshutz, S. Ghorai, and M. Cortes-Clerget, "The Hydrophobic Effect Applied to Organic Synthesis: Recent Synthetic Chemistry "in Water"," *Chemistry (Weinheim an der Bergstrasse, Germany)*, vol. 24, no. 26, pp. 6672–6695, 2018.

[136] T. Hayashi, K. Ueyama, N. Tokunaga et al., "A chiral chelating diene as a new type of chiral ligand for transition metal catalysts: its preparation and use for the rhodium-catalyzed asymmetric 1,4-addition," *Journal of the American Chemical Society*, vol. 125, no. 38, pp. 11508–11509, 2003.

[137] M. Nagamoto and T. Nishimura, "Asymmetric Transformations under Iridium/Chiral Diene Catalysis," *ACS Catalysis*, vol. 7, no. 1, pp. 833–847, 2017.

[138] B. M. Trost, A. C. Burns, and T. Tautz, "Readily accessible chiral diene ligands for Rh-catalyzed enantioselective conjugate additions of boronic acids," *Organic letters*, vol. 13, no. 17, pp. 4566–4569, 2011.

[139] A. Kina, K. Ueyama, and T. Hayashi, "Enantiomerically pure rhodium complexes bearing 1,5-diphenyl-1,5-cyclooctadiene as a chiral diene ligand. Their use as catalysts for asymmetric 1,4-addition of phenylzinc chloride," *Organic letters*, vol. 7, no. 26, pp. 5889–5892, 2005.

[140] P. Tian, H.-Q. Dong, and G.-Q. Lin, "Rhodium-Catalyzed Asymmetric Arylation," *ACS Catalysis*, vol. 2, no. 1, pp. 95–119, 2012.

[141] N. Sieffert, J. Boisson, and S. Py, "Enantioselective Arylation of N-Tosylimines by Phenylboronic Acid Catalysed by a Rhodium/Diene Complex: Reaction Mechanism from Density Functional Theory," *Chemistry (Weinheim an der Bergstrasse, Germany)*, vol. 21, no. 27, pp. 9753–9768, 2015.

[142] S. Burauer, T. Sottmann, and R. Strey, "Nonionic microemulsions with cyclic oils: Oil penetration, efficiency and monomeric solubility," *Tenside Surfactants Detergents,* no. 37, pp. 8–16, 2000.

[143] M. Deimling, M. Kirchhof, B. Schwager et al., "Asymmetric Catalysis in Liquid Confinement: Probing the Performance of Novel Chiral Rhodium-Diene Complexes in Microemulsions and Conventional Solvents," *Chemistry (Weinheim an der Bergstrasse, Germany)*, vol. 25, no. 40, pp. 9464–9476, 2019.

[144] T. Sottmann and C. (E.) Stubenrauch, *Microemulsions Background, new concepts, applications, perspectives*: *Phase Behaviour, Interfacial Tension and Microstructure of Microemulsions*, Wiley, Chichester, West Sussex, U.K., Ames, Iowa, 2009.

[145] H. Egger, T. Sottmann, R. Strey et al., "Nonionic microemulsions with chlorinated hydrocarbons for caralysis," *Tenside Surfactants Detergents,* no. 39, pp. 2–7, 2002.

[146] J. Saien and S. Akbari, "Interfacial Tension of Toluene + Water + Sodium Dodecyl Sulfate from (20 to 50) °C and pH between 4 and 9," *Journal of Chemical & Engineering Data*, vol. 51, no. 5, pp. 1832–1835, 2006.

[147] M. Teubner and R. Strey, "Origin of the scattering peak in microemulsions," *The Journal of Chemical Physics*, vol. 87, no. 5, pp. 3195–3200, 1987.

[148] Z. Cui, Y.-J. Chen, W.-Y. Gao et al., "Enantioselective alkenylation of aldimines catalyzed by a rhodium-diene complex," *Organic letters*, vol. 16, no. 3, pp. 1016–1019, 2014.

[149] M. Schwan, L. G. A. Kramer, T. Sottmann et al., "Phase behaviour of propane- and scCO(2)-microemulsions and their prominent role for the recently proposed foaming procedure POSME (Principle of Supercritical Microemulsion Expansion)," *Physical chemistry chemical physics : PCCP*, vol. 12, no. 23, pp. 6247–6252, 2010.

[150] M. Kahlweit, R. Strey, and G. Busse, "Microemulsions: a qualitative thermodynamic approach," *The Journal of Physical Chemistry*, vol. 94, no. 10, pp. 3881–3894, 1990.

[151] P. Lindner and T. Zemb, eds., *Neutrons, X-rays and light*: *Scattering methods applied to soft condensed matter ; [completely revised 'Bombannes' lectures*, Norh-Holland Elsevier, Amsterdam, 2002.

[152] S. W. Provencher, "A constrained regularization method for inverting data represented by linear algebraic or integral equations," *Computer Physics Communications*, vol. 27, no. 3, pp. 213–227, 1982.

[153] B. v. Szyszkowski, "Experimental studies of the capillary properties of aqueous solutions of fatty acids," *Zeitschrift für Physikalische Chemie,* no. 64, pp. 385–414, 1908.